An Investigation of Cancer Effect on Viscoelastic Properties of Prostate Gland via Quasi-Linear Viscoelastic Model

by

Hamed Helisaz

B.Sc., Sharif University of Technology, 2014

M.Sc., Sharif University of Technology, 2016

A THESIS SUBMITTED IN PARTIAL FULFILLMENT
OF THE REQUIREMENTS FOR THE DEGREE OF

Doctor of Philosophy

in

THE FACULTY OF GRADUATE AND POSTDOCTORAL STUDIES
(Mechanical Engineering)

The University of British Columbia
(Vancouver)

September 2022

© Hamed Helisaz, 2022

The following individuals certify that they have read, and recommend to the Faculty of Graduate and Postdoctoral Studies for acceptance, the thesis entitled:

An Investigation of Cancer Effect on Viscoelastic Properties of Prostate Gland via Quasi-Linear Viscoelastic Model

submitted by **Hamed Helisaz** in partial fulfillment of the requirements for the degree of **Doctor of Philosophy** in **Mechanical Engineering**.

Examining Committee:

Mu Chiao, Professor, Mechanical Engineering, UBC
Supervisor

Mattia Bacca, Assistant Professor, Mechanical Engineering, UBC
Supervisory Committee Member

Abbas Samani, Professor, Electrical and Computer Engineering, Western University
External Examiner

Purang Abolmaesumi, Professor, Electrical and Computer Engineering, UBC
University Examiner

Mauricio Ponga de la Torre, Assistant Professor, Mechanical Engineering, UBC
University Examiner

Additional Supervisory Committee Members:

Boris Stoeber, Professor, Electrical and Computer Engineering and Mechanical Engineering, UBC
Supervisory Committee Member

Clarence de Silva, Professor, Mechanical Engineering, UBC
Supervisory Committee Member

Ryozo Nagamune, Professor, Mechanical Engineering, UBC
Supervisory Committee Member

Abstract

Mechanical properties of biological tissues have been shown to vary in the presence of pathological disorders. This dissertation aims to investigate the effect of cancer on the viscoelastic properties of prostate gland. We use the quasi-linear viscoelastic model to characterize the elastic and viscous characteristics of thirty-five fresh prostate glands, removed within two hours of radical prostatectomy surgery. The viscoelastic properties of normal and cancerous prostates are compared to reveal the influence of cancer grade and tumor volume on the elasticity and viscosity of prostate tissue.

We first present a novel method for describing the time-dependent behavior of soft materials using one-dimensional quasi-linear viscoelastic model. Our model derives the elastic (Young's modulus) and viscous (shear relaxation modulus) properties by analyzing the stress response after a sudden uniaxial compression. The model is validated using experimental data on the phantoms that mimic the elasticity of normal and cancerous prostate tissues.

The applicability of the model for material characterization is demonstrated by introducing a procedure for obtaining the mechanical properties via indentation test. Using three-dimensional equations and pre-calculated finite element analysis, the procedure introduces a fast and straightforward approach that is superior to inverse finite element methods. We evaluate our procedure by comparing the derived properties with those obtained from uniaxial compression test, where the results show high precision (standard deviation less than 10%) and good accuracy (error less than 20%).

Finally, the procedure introduced for material characterization is used to characterize the viscoelastic properties of prostate gland. We test four different locations on fresh, unfixed prostate samples and compare the properties of locations where cancer spreads with those where cancer is not present. Our data-driven results demonstrate that tumor volume increases elastic and viscous properties of prostate with high statistical significance (p-value $< 2\%$), which reflects the potential of using the mechanical properties of prostate as a cancer biomarker. However, the author admits the challenges for realizing an *in vivo* apparatus to measure the viscoelastic properties of prostate. In fact, *in vivo* application of the findings requires other considerations that are not discussed here.

Lay Summary

Prostate cancer is the second most common type of cancer in the World and one of the leading causes of cancer deaths among men. When diagnosed at early stages, prostate cancer can be cured with minimal side effects. One of the primary methods for detecting prostate cancer is monitoring the viscoelastic properties of the prostate, as cancer affects the elastic and viscous properties of the tissue. This dissertation introduces a model for finding the viscoelastic properties of the prostate and investigates the influence of cancer on prostate properties.

First, we introduce a model to describe prostate tissue in one dimension and then present a method to extend the model to three-dimension. Finally, we use our model to study the behavior of normal and cancerous prostate tissue and compare the findings to understand the effect of cancer. Our results show that cancer increases the stiffness and viscosity of prostate tissue.

Preface

This dissertation entitled ”An Investigation of Cancer Effect on Viscoelastic Properties of Prostate Gland via Quasi-Linear Viscoelastic Model” describes the research projects that I carried out during my PhD. The research projects that introduced in this dissertation were mainly designed and supervised by Mu Chiao (Supervisor). In this preface, the contributions and collaborations to the projects and published papers are briefly explained.

A version of Chapter 2 has been published as: ”H. Helisaz, M. Bacca, and M. Chiao, “Quasi-Linear Viscoelastic Characterization of Soft Tissue-Mimicking Materials,” ASME J. Biomech. Eng., vol. 143, no. 6, Jun. 2021, doi: 10.1115/1.4050036.” This research project was designed by Hamed Helisaz, Mattia Bacca, and Mu Chiao. Hamed Helisaz (author) derived the model formulation, and conducted numerical simulations and data collection. Mu Chiao and Mattia Bacca supervised the content and formula and contributed to the editing of the paper.

A version of Chapter 3 has been published as: ”H. Helisaz, M. Bacca, and M. Chiao, “A New Characterization Procedure for Quasi-Linear Viscoelastic Materials Using Indentation Test: Validation with Finite Element and Experimental Results,” Exp. Mech., no. 0123456789, 2022, doi: 10.1007/s11340-022-00837-7.” This research project was designed by Hamed Helisaz, Mattia Bacca, and Mu Chiao. Hamed Helisaz (author) conducted the finite element analysis, designed experiments, and derived the results. Mattia Bacca supervised the formula and Mu Chiao and Mattia Bacca supervised content and contributed to the editing of the paper.

Hamed Helisaz, Mu Chiao, Peter Black, Eric Belanger designed the research project in chapter 4. Hamed Helisaz designed and coordinated the clinical study, and performed the data and statistical analysis on the results. Ethical and operational approval for the clinical study was obtained from the Research Ethics Board at the University of British Columbia (CREB Number: H19-03592) and the Vancouver Coastal Health Authority (VCH Number: V19-03592). Peter Black performed the surgeries for removing prostate glands, Eric Belanger conducted histology analysis on the prostate glands, and Mu Chiao supervised the process. The sensor design and fabrication in the last section was also performed with significant contribution from Anoush Sepehri, who also provided the data for this section.

Table of Contents

Abstract . . . . **iii**

Lay Summary . . . . **v**

Preface . . . . **vi**

Table of Contents . . . . **viii**

List of Tables . . . . **xi**

List of Figures . . . . **xiii**

Nomenclature . . . . **xxvii**

Acknowledgments . . . . **xxix**

1 Introduction **1**
- 1.1 Measurement of Tissue Viscoelasticity 2
  - 1.1.1 Tissue Actuation 2
  - 1.1.2 Response Detection 2
  - 1.1.3 Modeling 4
- 1.2 Material Characterization with the Quasi-linear Viscoelastic Model 9
- 1.3 Effect of Cancer on Mechanical Properties of Prostate Tissue . . . 11
- 1.4 Dissertation Organization 13

2 Quasi-linear Viscoelastic Calibration of Soft Materials via Uniaxial Test . . . 15
2.1 Methods and Materials . . . 16
2.1.1 QLV Model in One Dimension . . . 16
2.1.2 Data-Fitting Algorithm . . . 19
2.1.3 Tissue-Mimicking Phantoms . . . 21
2.1.4 Method Validation and Confidence Interval . . . 22
2.2 Results and Discussion . . . 25
2.3 Summary . . . 28

3 Quasi-linear Viscoelastic Characterization of Soft Materials via Indentation Test and Finite Element Analysis . . . 31
3.1 Methods and Materials . . . 32
3.1.1 Three-dimensional QLV Constitutive Equation . . . 32
3.1.2 Finite Element Implementation . . . 35
3.1.3 Model Validation . . . 36
3.2 Results and Discussion . . . 39
3.2.1 The Elastic Part of Indentation Behavior . . . 39
3.2.2 The Viscous Part of Indentation Behavior . . . 41
3.3 The New Material Characterization Procedure . . . 46
3.4 Summary . . . 52

4 Effect of Cancer on the Viscoelastic Properties of Prostate Tissue . . . 56
4.1 Experimental Design for Ex Vivo Testing . . . 57
4.1.1 Model Validation with Prostate-mimicking Phantoms . . . 57
4.1.2 Experiment with Fresh Prostate Tissue . . . 60
4.2 Results and Discussion . . . 62
4.2.1 Application of the QLV model to Prostate Tissue . . . 62
4.2.2 Effect of Cancer on Mechanical Properties of Prostate . . . 64
4.2.3 Effect of Cancer Grade on the Prostate Gland . . . 70
4.3 Application in Prostate Cancer Diagnosis . . . 74
4.4 Summary . . . 76

5 Conclusions and Future Work . . . 78

5.1 Conclusion 78
    5.1.1 Calibrating the QLV Model via the Uniaxial Test 78
    5.1.2 QLV Characterization via the Indentation Test 79
    5.1.3 Effect of Cancer on Prostate Viscoelasticity 80
5.2 Future Work 81

Bibliography 83

A A Possible Approach for *In Vivo* Diagnosis of Prostate Cancer 96
A.1 Sensor Design and Fabrication 96
A.2 Validation on Prostate-mimicking Phantoms 98

B Prostate Glands for Clinical Study 103

List of Tables

Table 2.1 The composition of tissue-mimicking phantoms 22

Table 2.2 The QLV parameters for tissue-mimicking phantoms; 95% confidence intervals are reported 23

Table 2.3 95% confidence intervals for relaxation parameters of Elastomer III under different strain levels (see Fig. 2.3) 25

Table 3.1 The QLV parameters of the fabricated silicon-based polymer; the parameters were obtained from uniaxial compression tests (see Chapter 2) and were used as the input for the ABAQUS® simulation. 37

Table 3.2 Comparing the relaxation parameters obtained from uniaxial compression and indentation: the parameters are first obtained from the compression test using the method described in Section 2.1 and compared with those calculated from an indentation test using our proposed methods (Eqs. (3.12) and (3.13)). Compression and indentation tests were repeated three times for each material and the mean values are reported along with the standard deviations. The table demonstrates that Eq. (3.13) introduces parameters with a high precision (standard deviation within 10%) and in a good agreement with uniaxial parameters (maximum error within 20%). 52

Table 4.1 95% confidence intervals for the ratio between the properties of the cancerous and normal sides of the posterior prostate. As seen in Fig. 4.10, the properties for the cancerous side are greater than those for the normal side. 69

Table 4.2 Descriptive and inferential statistics for the cancer effect on the viscoelastic properties of the prostate gland when cancer presents in the posterior prostate. The table also includes p-values for the alternative hypothesis with $g_i^{\text{cancer}}/g_i^{\text{normal}} > 1$ and $\sigma_E^{\text{cancer}}/\sigma_E^{\text{normal}} > 1$. From the table, cancer appears to have a greater statistically significant effect on g_1 and σ_E (lower p-values). 75

Table 4.3 95% confidence interval for non-cancerous prostate samples. Since cancer is absent from the prostate sections, the properties for the left and right sides are expected to be similar. The table shows that g1 and g3 are relatively biased towards higher ratios and g2 and E are balanced around a ratio of one. 76

Table B.1 Characteristics of fresh prostate samples used in the clinical study: Thirty-five fresh prostate samples, identified as P1-P35 were collected within two hours after removal by prostatectomy surgery. The table includes the location(s) of the cancer in mid and apical sections, cancer grade, Gleason score, prostate volume, prostate mass, and the patient's age. The results for samples P1-P3 are used in Section 3.1 to check the suitability of the QLV model for the prostate gland, and the results for samples P4 - P35 are used in Sections 3.1 and 3.2 for studying the effect of cancer on the properties of the prostate gland. Some of the prostate characteristics were not available and appear empty in the table. 104

List of Figures

Figure 1.1 Comparison of the actual mechanical response of the rabbit mesentery (solid line) with the corresponding incremental lines (dashed lines). Reproduced with permission from [1]. 5

Figure 1.2 Time-dependent characteristic of tissue behavior: a) change in loading/unloading behavior of an anterior cruciate ligament through time; b) pre-conditioning of a dog's carotid artery. Reproduced with permission from [1]. 7

Figure 1.3 Different forms of spring-dashpot models; (a) Maxwell model, (b) Kelvin-Voight model, (c) Standard Linear Solid model. Reproduced with permission from [2] 8

Figure 2.1 Experimental procedure: (a) a series of low-range compressions: each is a 2.5% strain and kept long enough until the stress reaches the steady-state; (b) stress response versus time under the prescribed displacement at (a): elastic properties are obtained by plotting the steady-state stress (orange dots) against the compression; (c) ramp-and-hold compression with 50% final strain: strain is kept long enough until the stress reaches the steady-state; (d) stress response versus time under the prescribed displacement at (c): the stress amplification factors g_1 and g_2, and g_3 measure the stress relaxation in the time intervals (τ_0, τ_1), (τ_1, τ_2), and (τ_2, τ_3) 21

Figure 2.2 Tissue-mimicking phantoms: (a) Elastomer I (67% Ecoflex™ 00-10 and 33% NOVOCS™); (b) Elastomer II (80% Ecoflex™ 00-30 and 20% NOVOCS™); c) Elastomer III (100% Ecoflex™ 00-10): Elastomer I mimics normal tissue in terms of Young's modulus while elastomers II and III mimic cancerous tissues. . 23

Figure 2.3 Model validation: a) ramp-and-hold compression with different final strains; b) stress response of Elastomer III versus time under the prescribed displacement at (a): lines are experimental results while symbols denote predictions of the QLV model (Eq. (2.9)). The experiments are repeated three times for each sample, and the mean values for the results are presented with the error bars. 24

Figure 2.4 Testing machine used to obtain stress response of materials: a custom compression has slightly larger diameter than samples to guarantee a uniaxial compression force. 26

Figure 2.5 Material characterization: lines are experimental results while symbols denote predictions of the QLV model (Eq. (2.9)). QLV parameters, including α, E, and g_i, can well distinguish the phantoms. The experiments are repeated three times for each sample, and the mean values for the results are presented with the error bars. 29

Figure 3.1 ABAQUS® simulation: a) axisymmetric model with a deformable part, for the soft material (shown in green), a rigid analytical part, for the indenter (shown in blue), and a rigid analytical part for the bottom support (shown in red); b) the indentation stress is expressed as von Mises stress; the indenter size φ and indentation depth δ are also shown in the figure. The results are depicted for φ = 7.60 mm, H = 18.88 mm, and D = 25 mm 37

Figure 3.2 Model validation: The ABAQUS® simulation results are compared with those obtained from experiments on a silicon-based polymer. Lines denote the QLV model prediction, and the symbols are the experimental results. The experiment includes compressing an indenter into the specimen at a rate of 10 mm/s and recording the force response ($\mathscr{F}$). The force data is then converted to stress (σ) by dividing force by the indenter surface area ($\frac{\pi}{4}\varphi^2$). Each experiment is repeated three times, and the mean values for the results are depicted along with the error bars. The results are depicted for specimen height $H = 18.88$ mm, specimen diameter $D = 25$ mm, and indenter diameter $\varphi = 7.60$ mm 38

Figure 3.3 Comparing the stress feedback with and without using WD-40 silicone lubricant (WD-40 Company Inc., California, USA). The figure demonstrates no difference between the results, which confirms the frictionless contacts in the experiment. The symbols indicate the experimental results for a silicon-based polymer with height H=18.88 mm and diameter $D = 25$ mm. . . . 40

Figure 3.4 Model validation for indenter diameter $\varphi = 4.95$ mm: the ABAQUS® simulation results are compared with those obtained from experiments on a silicon-based polymer. Lines denote the QLV model prediction, and the symbols are the experimental results. The results are depicted for specimen height $H = 18.88$ mm and specimen diameter $D = 25$mm. 41

Figure 3.5 Model validation for indenter diameter $\varphi = 6.33$ mm: the ABAQUS® simulation results are compared with those obtained from experiments on a silicon-based polymer. Lines denote the QLV model prediction, and the symbols are the experimental results. The results are depicted for specimen height $H = 18.88$ mm and specimen diameter $D = 25$mm. 42

Figure 3.6 Model validation for indenter diameter $\varphi = 8.88$ mm: the ABAQUS® simulation results are compared with those obtained from experiments on a silicon-based polymer. Lines denote the QLV model prediction, and the symbols are the experimental results. The results are depicted for specimen height $H = 18.88$ mm and specimen diameter $D = 25$mm. 43

Figure 3.7 Effect of elastic parameters (μ and α) on indentation behavior: effect of a) shear modulus μ and b) strain-stiffen parameter α on the stress response of the material. The behavior shows a peak stress followed by stress relaxation until the results reach a steady-state. The steady-state stress occurs when the viscous properties of a material vanish, and only the elastic properties remain. The results demonstrate that the indentation stress is sensitive to both μ and α: it has a linear relationship with μ and a non-linear relationship with α. 44

Figure 3.8 Effect of indenter size and indentation depth on the elastic stress of the material. The results are nondimensionalized to clarify the impact of each parameter; elastic stress is nondimensionalized with shear modulus μ and indentation depth δ with indenter diameter φ. Unlike the prediction of linear elasticity, the curves for different indenter diameters do not intersect, and the data suggests a non-linear relationship between stress and indentation depth. The results are depicted for specimen height $H = 18.88$ mm and specimen diameter $D = 25$ mm. 45

Figure 3.9 Nondimensionalized stress behavior for different indenter diameters and indentation depths: nondimensionalized stress response at indentation diameters of a) $\varphi = 4.95$ mm, b) $\varphi = 6.33$ mm, c) $\varphi = 7.60$ mm, and d) $\varphi = 8.88$ mm. The results demonstrate that relaxation behavior does not depend on the indentation size and depth. 46

Figure 3.10 Effect of material properties on the viscous behavior: evolution of nondimensionalized stress relaxation over time for different values of a) g_1, b) g_2, and c) g_3: the results indicate that the stress relaxation is proportional to the value of g_is. The relaxation caused by $g_i = 2$ is two-times that of $g_i = 1$; d) the nondimensionalized stress relaxation associated with multiple g_is; the figure shows that the stress relaxation caused by several g_is is obtained by adding the stress relaxations made by each. 47

Figure 3.11 Stress relaxation in different time intervals: four time intervals are determined by τ_0, τ_1, τ_2, and τ_3, where τ_0 measures the indentation time and τ_1, τ_2, and τ_3 denote the relaxation times. The stress relaxation in the time interval (τ_{i-1}, τ_i) is obtained by subtracting the stress at $t = \tau_i(\sigma_{\tau_i})$ from the stress at $t = \tau_{i-1}(\sigma_{\tau_{i-1}})$. The data is nondimensionalized by the elastic stress σ_E. 48

Figure 3.12 Effect of indentation rate on the viscous behavior: evolution of nondimensionalized stress relaxation over time when a) $g_1 = 1$, b) $g_2 = 1$, and c) $g_3 = 1$. The indentation rate is measured by indentation time τ_0, which is measured against τ_i. Stress relaxation increases as τ_i/τ_0 increases; in particular, when $\tau_i/\tau_0 \geq 10$, the indentation rate is sufficiently fast to fully capture the stress relaxation $(\sigma - \sigma_E/\sigma_E \approx 1)$. In addition, the stress relaxation is shown to depend on τ_i/τ_0 and not on the individual values of τ_i and τ_0. While τ_i differs in different plots, the same stress relaxation is observed when τ_i/τ_0 is the same. 49

Figure 3.13 The stress relaxation of Fig. 3.12 in different time intervals; the data is nondimensionalized by elastic stress, and expressed as a percentage. The coefficient g_i affects the stress relaxation mainly between (τ_{i-1}, τ_{i+1}); in particular, the stress relaxation over the last time interval is only influenced by g_3 since $\Delta\sigma_{\tau_3-\infty}$ is zero when $g_1 = 1$ or $g_2 = 1$. Likewise, stress relaxation in (τ_2, τ_3) depends on g_2 and g_3 ($\Delta\sigma_{\tau_2-\tau_3}$) is zero when $g_1 = 1$ and the stress relaxation between (τ_1, τ_2) depends on all three relaxation coefficients. 50

Figure 3.14 The suggested characterization procedure; a) stress relaxation from a ramp-and-hold indentation experiment. The figure shows stress relaxation created by b) $g_1 = 1$, c) $g_2 = 1$, and d) $g_3 = 1$. Note that the values for $\Delta\hat{\sigma}^{g_1=1}_{\tau_2-\tau_3}, \Delta\hat{\sigma}^{g_1=1}_{\tau_3-\infty}$, and $\Delta\hat{\sigma}^{g_2=1}_{\tau_3-\infty}$ are all zero. Eq. (3.12) compares the stress relaxation at three points ($t = \tau_1$, $t = \tau_2$, and $t = \tau_3$ in figure a) with those of pre-calculated simulation results (figures b-d) and derives the material's parameters. The results are depicted for indentation time $\tau_0 = 0.5$ s. 51

Figure 3.15 Effect of indentation rate (measured by τ_0) on the stress relaxations created by $g_1 = 1, g_2 = 1$, and $g_3 = 1$. The results demonstrate the stress relaxation between a) $(\tau_1 - \tau_2)$, b) $(\tau_2 - \tau_3)$, and c) $(\tau_3 - \infty)$. The stress relaxation decreases as the indentation time (τ_0) increases (slower indentation). No stress relaxation is created by g_1 after $t = \tau_2$ ($\Delta\hat{\sigma}^{g_1=1}_{\tau_2-\tau_3}$ and $\Delta\hat{\sigma}^{g_1=1}_{\tau_3-\infty}$) are zero in figures b and c) and no stress relaxation is made by g_2 after $t = \tau_3$ ($\Delta\hat{\sigma}^{g_2=1}_{\tau_3-\infty}$ is zero in figure c)). Since the values of $\Delta\hat{\sigma}^{g_1=1}, \Delta\hat{\sigma}^{g_2=1}$, and $\Delta\hat{\sigma}^{g_3=1}$ are dependent on the indentation rate, the values substituted in Eq. (3.12) and (3.13) should correspond to τ_0 used in the experiment. 53

Figure 3.16 Normalized stress for indentation tests with different indentation tilt angles, defined as the angle between the indenter and contact surface normal (θ). The results demonstrate that tilt angle (misalignment) up to 20° does not affect the stress relaxation. Note that the figure represents the experimental data since the indentation test with 0 cannot be modelled with an axisymmetric simulation. 54

Figure 3.17 Algorithm for writing the UMAT software in Fortran; the UMAT receives the deformation gradient tensor (from ABAQUS calculations) and material properties (from user inputs) and provides the Cauchy stress and elasticity tensor. 55

Figure 4.1 Procedure for mechanical testing: a) the sample is compressed at 10 mm/s and kept at an indentation depth (here, $\delta = 5$mm for 45 seconds), b) stress response after the compression shown in (a). Stress peaks occurred at $t = \tau_0$ and then they relaxed over time until reaching the steady-state stress σ_E. Relaxation shear moduli g_is were determined by the stress relaxation that occurred in different time periods, as specified by relaxation times τ_ks. Three relaxation times τ_1, τ_2, and τ_3 were chosen that were 0.1, 1, and 10 seconds, respectively, after $t = \tau_0$. . . 58

Figure 4.2 Tissue-mimicking phantoms with embedded nodules to resemble cancerous prostate tissue: a) phantoms were fabricated by Ecoflex™ 00-10 with elasticity close to the Young's modulus of normal prostate gland. The anatomical model was used to ensure that the phantom's shape was similar to that of the posterior prostate, b) a hard nodule was embedded on the left side of the phantom to mimic the presence of cancer. Nodules were made by Ecoflex™ 00-50 with a Young's modulus close to that of prostate cancer. Three phantoms were fabricated with different-sized nodules; i.e., 5 mm, 7 mm, and 10 mm, representing the presence of cancer in early, intermediate, and advanced stages, respectively, c) mechanical tester (Mach-1 V500CS) equipped with a multiple-axis load cell to record the stress response of tissue at a sampling rate of 100 Hz. . . . 59

Figure 4.3 Model validation with tissue-mimicking phantoms: comparison of relaxation shear moduli between the side with the hard nodule (i.e., the "cancerous" side) and the side without a nodule (i.e., the "normal" side), for nodule sizes of a) 10 mm, b) 7 mm, and c) 5 mm. The figure shows that larger nodules led to higher viscous properties. 61

Figure 4.4 Model validation with tissue-mimicking phantoms: comparison of elastic properties (steady-state stress) between the side with the hard nodule (i.e., the "cancerous" side), and the side without a hard nodule (i.e., the "normal" side), for nodule sizes of 10 mm, 7 mm, and 5 mm. The figure shows that larger nodules led to higher elastic properties. 61

Figure 4.5 Fresh prostate gland: tissues were collected within two hours after being removed by radical prostatectomy surgery. Tests were performed on mid and apex sections of the posterior prostate and the mechanical properties were compared to those at the left and right sides of the posterior prostate. 62

Figure 4.6 The prostate was placed into a container filled with phosphate buffered saline (PBS) to avoid dehydration. Samples were supported from beneath by a plastic holder and oriented so that the anterior prostate was at the bottom (touching the holder) and the posterior prostate was at the top (touching the indenter). . 63

Figure 4.7 Applicability of the QLV model for prostate tissue: the QLV model's applicability for predicting the viscoelastic behavior of prostate tissue was checked by testing the separation between the viscous and elastic parts of the stress response. Testing was performed with different indentation depths; i.e., 4 mm, 5 mm, and 6 mm, and the stress was normalized by the elastic stress to obtain the viscous part of the stress. The results show that the elastic and viscous parts of the prostate stress response are separable since while the indentation depth varies, and hence the elastic part of stress, the viscous part remained the same. 65

Figure 4.8 Applicability of the QLV model for the prostate gland: mechanical testing was performed with different indentation depths; i.e., $\delta = 4$ mm, 5 mm, and 6 mm, and the relaxation shear moduli g_is were obtained for each test. Each test was repeated eight times and the average and standard deviation of g_is for the last six tests were reported in the figure (blue, orange, and green boxes). The properties are normalized by g_i^{avg}s; i.e., the average of the properties for the three indentation depths. The figure shows that a) g_1, b) g_2, and c) g_3 from tests at different indentation depths are close. The greater variation of g_1 is mainly due to overshoot; i.e., when the tester cannot precisely control the final deformation at a high indentation rate. The figure also shows that the variation within g_is for the different tests is within 10%, which indicates the precision of the measurements. 66

Figure 4.9 Precision of the QLV model: each mechanical test was repeated eight times and the results of last six tests were used for the figure. σ_E from each test was compared to the average elastic stress σ_E^{avg} to determine the precision of the measurements. From this figure (and Fig. 4.8) the QLV model has a high precision for reporting the viscoelastic properties of the prostate. 67

Figure 4.10 Effect of cancer on the mechanical properties when cancer is in posterior prostate (a-d); and when cancer is in anterior prostate (a-h). Samples that had cancer on both sides were excluded. The properties were normalized by dividing the properties of the cancerous side by the properties of the normal side for each section. Tests were repeated eight times for each quadrant and the average of the last six tests were used to calculate the properties. The figures show higher values for the properties on the cancerous side, especially for a) g_1, and d) σ_E as the ratio for the properties on the cancerous and normal sides are mostly above one. The effect of cancer on the properties is less significant when cancer occurred in the anterior prostate e-h), mainly because the tests were performed on the posterior prostate, which limits the accuracy in capturing the anterior prostate properties. 68

Figure 4.11 Mechanical properties of non-cancerous prostate gland. The properties are normalized by dividing the properties for the right side by the properties for the left side in each section. Since no cancerous nodules are in the prostate, the properties for the left and right sides are expected to be similar. The shaded area shows the 10% variation in the properties, which can be considered as insignificant (see Fig. 4.8 and Fig. 4.9). The figures also show more similarity between the properties for the left and right sides for a) g_1 and d) σ_E. The higher difference in g_2, c) g_3 may be explained by the presence of a nodule in a nearby section. 69

Figure 4.12 Correlation between different properties of the prostate gland: a) correlation between cancer grade, prostate mass, and prostate volume, and b) correlation between cancer grade, prostate volume, and patient's age. a) shows a strong correlation between the prostate volume and mass, but the cancer grade does not appear to be correlated to the mass or volume. For example, cancer grade 5 could be assigned to either a small or a large prostate gland. b) shows a positive correlation between patient's age and prostate volume. While a clear relationship between cancer grade and age is not seen, high-grade cancer (i.e., grades 4 and 5) are more likely to occur in older patients. . . . 71

Figure 4.13 Gleason scores for prostate cancer cells: a) patterns for Gleason score 3 have well-formed glands without fusion, b) patterns for Gleason score 4 have back-to-back fused glands and a sieve-like structure formed by the cells, and c) patterns for Gleason score 5 show cell invasion in the glands. 72

Figure 4.14 Correlation between tumor volume and properties when cancer presents in the posterior prostate. The properties were normalized by dividing the properties for the cancerous side to the properties for the normal side. Viscous properties are affected by tumor volume (see a, b, and c) while the elastic properties do not seem to vary with tumor volume (see d). g_1 and g_3 have the highest statistical significance (lowest p-value). The cancer grade does not appear to be correlated with tumor volume or the viscoelastic properties. International Society of Urological Pathology (ISUP) Cancer Grade was reported, and calculated based on the Gleason score. Cancer grades 2, 3, 4, and 5 are associated with Gleason Score 3+4, 4+3, 4+4, and 4+5 (or 5+4), respectively. 73

Figure 4.15 Correlation between tumor volume and mechanical properties when cancer presents in the anterior prostate. The properties are normalized by dividing the properties on the cancerous side by the properties on the normal side. Unlike Fig. 4.14, no clear correlation can be seen between tumor volume and the viscoelastic properties. This may be due to our testing that was performed on the posterior prostate, which fails to accurately capture the properties in the anterior prostate. International Society of Urological Pathology (ISUP) Cancer Grade was reported, and calculated based on the Gleason score. Cancer grades 2, 3, 4, and 5 are associated with Gleason Score 3+4, 4+3, 4+4, and 4+5 (or 5+4), respectively. 74

Figure 4.16 Correlation between cancer grade and relative tumor volume (tumor volume divided by prostate volume). No clear correlation is seen between cancer grade, patient's age, and the relative tumor volume. International Society of Urological Pathology (ISUP) Cancer Grade was reported, and calculated based on the Gleason score. Cancer grades 2, 3, 4, and 5 are associated with Gleason Score 3+4, 4+3, 4+4, and 4+5 (or 5+4), respectively. 75

Figure A.1 Design of the proposed FBG sensor: The sensor is composed of an FBG sensor bonded to a elastomer (polyurethane) rod and it is supported by a 3D printed enclosure. The rod is designed to contact the material through a sensor head with a diameter of 6 mm. The sensor is compressed into a material by using an actuator and the force reaction of the material is recorded over time. The size of the sensor is designed to allow for *in vivo* applications. 98

Figure A.2 Sensor calibration: the mechanical tester described in Section 2.1 was used to calibrate the sensor. The FGB sensor was placed beneath the tester's indenter and a range of strains from 0 to 2.25% were applied in intervals of 0.225%. The sensor information was read through the interrogator and calibrated by the forces recorded for the load cell. The calibration showed a linear relationship between the sensor's measurements (wavelength shift in the FBG sensor) and Force, with a maximum non-linearity error of 22 mN. 99

Figure A.3 Testing the FBG sensor on the prostate-mimicking phantoms: phantoms were fabricated as described in Section 4.1.1 and the nodule was located in L1; c) the FBG sensor was used to measure the force response of the prostate phantoms after each test. The sensor was connected to the actuator with an adaptor and a custom-built rig. Experiments were repeated three times for each quadrant (L1-L4) and the average QLV parameters were recorded for each quadrant. 100

Figure A.4 Validation of the FBG sensor applicability by testing on prostate-mimicking phantoms: viscous properties (g_i s) are reported for a) L1, b) L2, c) L3, and d) L4 for hard nodules with diameters of 5 mm, 7 mm, and 10 mm. The figure shows that the most variation occurs for the properties at L1, where the nodules are located. The properties at L4 also vary slightly for the different nodule sizes, which is likely due to the effect of a hard nodule in a nearby quadrant. L2 and L3, however, have similar properties for the different nodule sizes. 101

Figure A.5 Validation of the FBG sensor applicability by testing the prostate-mimicking phantoms: elastic stress is shown for quadrants with different nodule sizes. The figure shows that the greatest variation in elastic stress occurs with the nodule sizes at L1. The elastic stress at L4 also varies slightly with the nodule size, which is likely due to the effect of a nearby quadrant. L2 and L3, however, have similar amounts of elastic stress for the different nodule sizes. 102

Nomenclature

C	Right Cauchy-Green Deformation Tensor
D	Specimen Diameter
E	Young's Modulus
$G(t)$	Reduced Function
H	Specimen Height
I_1	First Invariant (Trace)
J	Volumetric Stretch
N_i	Eigenvector
P	Hydrostatic Pressure
α	Ogden's Model Constant
$\boldsymbol{F}$	Deformation Gradient Tensor
$\boldsymbol{S}$	2nd Piola-Kirchhoff Tensor
$\boldsymbol{\ell}$	Elasticity Tensor
δ	Indentation Depth
ε	Strain
κ	Bulk Modulus

λ	Axial Compression
λ_i	Eigenvalue
μ	Ogden's Model Constant
ϕ	Material Constitutive Parameter
ψ	Strain Energy Density Function
σ	Cauchy Stress
σ_E	Steady-state (Elastic) Cauchy Stress
τ	Relaxation Time
φ	Indenter Size
g_i	Shear Relaxation Modulus

Acknowledgments

I would first like to thank my advisor, Prof. Mu Chiao. He has been very supportive in the course of my Ph.D. program and provided me with the resources, without which the work could not be imagined. His generosity, guidance, sharpness, and approach to science have all contributed to shape who I am in my research career. I also want to thank my lab mates, Minghua Wu, Hiroshan Gunawardane, Shayan Jannati, Anoush Sepehri, Ali Shademani, and Ali Moalemi for creating an intellectually stimulating environment where I could better develop my research ideas. Furthermore, I very much appreciate the supports I received from John Jackson, who helped me to shape my ideas at the beginning of my study.

I want to thank Dr. Mattia Bacca, Dr. Peter Black, and Dr. Eric Belanger, who have worked closely with me through the years and given me invaluable advice. Dr. Bacca supported me in the mathematical side of the project and Dr. Black and Dr. Belanger made the clinical study possible and facilitated the collaboration with Vancouver General Hospital. I would also like to thank my supervisory committee, Prof. Boris Stoeber, Prof. Clarence de Silva, and Prof. Ryozo Nagamune, for their input and guidance in turning this into a stronger dissertation. I would also like to show my appreciation to Dr. Danmei Liu and Vivian Chung who provided me with excellent support in The Robert HN Ho Research Centre. In addition, I want to thank Ali Hussein and Mathieu Roumiguie for facilitating the clinical study.

To my friends: thank you so much, Vahid Karamzadeh, Mohammadhossein Akhavanfar, Abdollah Safari, Amin Arefi, Amirhossein Afshinfard, and Hamidreza Eslami, for all your assistance and for giving me strong encouragement when, at times, I had to grapple with deep frustration and self-doubt. My warm gratitude also goes to Alireza Zakeri, Kasra Ghorbaninejad, and Ali Karimi for all their help

and emotional support.

Last but not least, I would like to thank my lovely wife, parents, parents-in-law, sister, brother, and brothers-in-law, for their moral support and encouragement in the pursuit of education. Without foundation they gave me, I would never have reached this stage.

Chapter 1

Introduction

Prostate cancer (PCa) is the second most common type of cancer in the world and the fifth leading cause of cancer death among men in 2020 [3]. Being diagnosed in early stages, PCa can be cured with manageable side effects. The initial screening method for PCa includes digital rectal examination (DRE) [4], where a physician examines the stiffness of the posterior prostate gland by finger. Higher stiffness in the prostate gland marks the presence of cancer [5]. The results of DRE though are not accurate as they are subjective and dependent on the sensitivity of the human finger. Naji et al. [6], Soeterik et al. [7], and Jones et al. [8], in different studies, showed that more than 50% of the people with abnormal DRE results do not have prostate cancer. Alternative methods have been introduced for measuring the mechanical properties of the prostate gland in an objective manner, among which ultrasonic elastography (USE) [9], magnetic resonance elastography (MRE) [10], and direct elasticity measurement [5] are more common. Despite their differences, all of these methods have the same basis: measuring the response of tissue upon applying a specific actuation [11]. This common basis requires all viscoelasticity measurement techniques to follow three main steps: actuating tissue, detecting the response, and extracting the properties based on a model.

1.1 Measurement of Tissue Viscoelasticity

1.1.1 Tissue Actuation

Tissue can be excited by applying either a displacement or a force. In the former, tissue is actuated by static or dynamic deformation. Takács et al. [12] measured the viscoelastic properties of liver by conducting a relaxation test, where the liver tissues were compressed at a rate of 750 mm/min, and then kept compressed at 4 mm for 60 seconds. The stress relaxation of tissues during this procedure was recorded to measure the viscous characteristics. In another work, dynamic deformation was utilized for measuring the stiffness of synthetic and natural sponges [13]. In this article, the sponges were excited by a sinusoidal deflection with an amplitude between 0.5-1.0 mm and frequency between 5-40 Hz. Alternatively, static and dynamic forces can be used in the actuation mode. Magnetic, piezoelectric, and pneumatic drivers are among the conventional methods for generating actuation force [14]. Mechanical drivers, however, are only appropriate when the properties of superficial organs are of interest. For deep organs, another technique called acoustic radiation force impulse (ARFI) should be considered [15, 16]. In ARFI, force is generated by focalizing an ultrasound beam to a small spot (a few square centimeters) [11, 17]. Since the actuation is produced by ultrasonic waves, this method can work without physical contact and so it is suitable for deep tissues. ARFI technique actuates tissue with high frequency (i.e., few MHz) [18]. High-frequency actuation, however, does not allow tissues to exhibit their entire viscoelastic characteristics. For example, it has been shown that stress relaxation in biological tissues can last for several minutes [19–21]. That is to say, using mechanical drivers with low actuation frequency is preferable to better capture the viscoelastic properties of materials, but the application is limited to superficial organs.

1.1.2 Response Detection

The second step is detecting tissue response upon the applied actuation. When tissue is excited by displacement, its force response is recorded, and vice versa [12]. In the literature, it is more common to use force as actuation and then measure the deformation. One of the methods for measuring tissue deformation is medical imaging, in which the images before and after actuation are compared to estimate displacement. Various imaging techniques, including ultrasound (US) and magnetic resonance (MR) can be used for this purpose. Knowing the tissue displacement over an applied force, the viscoelasticity of tissue can then be calculated. Despite providing a straightforward method for measuring biomechanical properties, this method suffers from that fact that the exact value of applied stress is not always known, especially when it comes to deep organs. To address this problem, researchers have developed another approach, called wave imaging, whereby tissue properties are determined without the stress field. In this approach, the waves created inside tissue as the result of actuation are considered for calculating stiffness. The waves induced after an actuation can move either in the same direction as the actuation (longitudinal waves) or normal to that (shear waves). It can be shown that the propagation speed of longitudinal and shear waves are dependent on the bulk modulus and shear modulus of the material, respectively [9]. Bulk modulus is less commonly used for characterizing biological tissues as they are almost incompressible and so highly resistant to change of volume. On the contrary, shear waves can well characterize tissues, and so the shear wave imaging is more common in the literate [9, 11]. Capturing shear wave velocity though is challenging. Shear waves propagate in opposite directions away from the actuation source, and so they are difficult to be monitored. Moreover, because of their high attenuation rate, shear waves can be detected only in a small region.

Alternatively, tissue can be actuated by a deformation and the stress response is measured by using electronic [22, 23] or optical pressure sensors [24, 25]. The electronic sensors, like piezoresistive and capacitive sensors, have a simple working mechanism and inexpensive fabrication cost [23]. Meanwhile, they have some drawbacks that compromise their applicability, especially when it comes to biomedicine. For example, they need to be in direct contact with the tissue while keeping the sensor fixed on tissue is challenging [26]. Also, miniaturizing the electronic sensors decreases their mechanical strength; that is why brittleness is accounted for one of the main problems of small (i.e., few millimeters) electronic sensors [22]. This is especially important in biomedical applications where unreliability of sensors can risk the patient's health. Optical sensing is an alternative sensing scheme for biomedical tactile sensors. In these sensors, the force-induced deflection is correlated by the optical properties of light in a fiber. The non-contact nature of optical sensors facilitates their application in biomedical systems. Also, optical sensors show good mechanical strength in small sizes [27]. These advantages have been encouraging an increasing number of researchers to select optical sensors for the biomedical applications. In particular, the Fibre-Bragg grating sensors (FBG) are more popular due to the simplicity in packaging process and low fabrication cost [25]. FBG sensors are made by inscribing diffraction grating on an optical fiber. The grating reflects a specific wavelength of light dependent on the grating period [28]. Reading the reflected wavelength, therefore, one can measure the strain in the fiber and hence the corresponding stress. FBG sensors, however, are subject to chirp failure; that is when the stress is not distributed uniformly in the grating zone, and multiple wavelengths are reflected [25]. To avoid the ambiguity caused by chirp failure, the sensor's design should guarantee uniform distribution of stress through fiber. Also, FBG sensors are susceptible to temperature so that temperature cross-sensitivity can exceed force sensitivity [24]. This problem can also be addressed by considering another optical fiber for temperature compensation.

Hitherto, techniques for actuating tissue and measuring the tissue feedback behavior are discussed. For discovering the tissue properties, a viscoelastic model is needed to translate the tissue behavior into quantifiable parameters reflecting its characteristics. This point brings us to the third and last step of viscoelasticity measurement which is discussed in the next subsection .

1.1.3 Modeling

The last step in determining materials' viscoelastic properties is extracting the intrinsic characteristics from the experimental data. No matter how accurate the first two steps (actuation and response measurement) are carried out, using an inappropriate model prevents obtaining accurate results. Modeling biological tissues, however, is difficult since their stress-strain behavior is non-linear and it can be different in loading and unloading cycles ([1]). To relive this difficulty, some techniques have been proposed in the literature to approximate the viscoelastic behavior

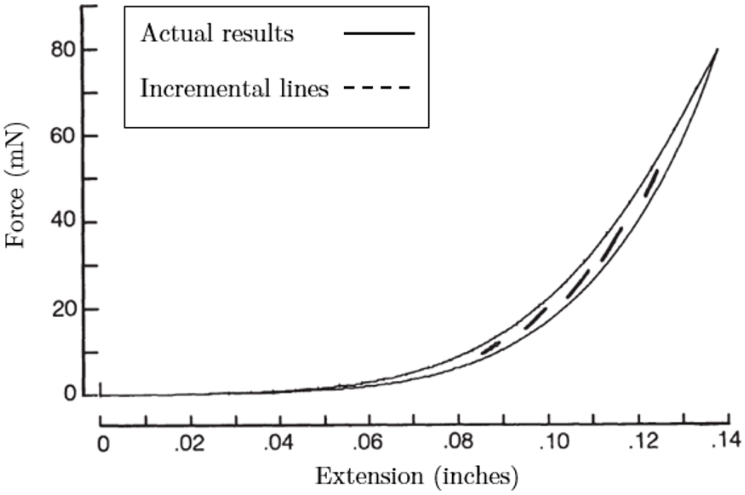

Figure 1.1: Comparison of the actual mechanical response of the rabbit mesentery (solid line) with the corresponding incremental lines (dashed lines). Reproduced with permission from [1].

of tissue with that of elastic materials, which is easier to be simulated.

Incremental Law

Viscoelastic substances demonstrate non-linear behavior when an actuation is applied. This non-linear behavior decays to linear form when perturbation is infinitesimal [1]. Therefore, dividing the actual actuation of tissue into a set of small disturbances, the stress-strain curve of tissue can be approximated by a set of lines, called incremental lines, each reflects a small disturbance (Fig. 1.1) compares the actual behavior of the rabbit mesentery with the corresponding incremental lines [1]. As it is seen in the figure, the actual behavior of tissue is estimated with several lines (dashed lines), each can be described by an elastic model. It should be noted that the incremental lines are not necessarily tangent to the actual curve of materials. In fact, these lines are not mathematically related to the actual behavior and should be obtained experimentally.

Pseudo-Elasticity and Hyperelasticity

The hysteresis loop shown in (Fig. 1.1) implies the fact that biological tissues have different behavior in loading and unloading cycles. Therefore, one can suggest two separate elastic models for describing the loading and unloading curves. Doing this, however, requires tissue to show consistent behavior over time, which is not necessarily true for soft tissues [1]: for example, Fig. 1.2a demonstrates the change in behavior of a ligament through time. Fortunately though, the time dependency of tissue's reaction can be removed by a process called pre-conditioning (Fig. 1.2b). In this process, the tissue completes several cycles before conducting the actual test. Accordingly, the discrepancy between the behavior of tissue in different cycles decreases, which results in a same loading/unloading curves through time. After pre-conditioning, tissue can be treated as a pseudo-elastic material exhibiting two different elastic behavior in loading and unloading cycles, each can be modeled with a separate model.

The techniques above enable us to consider elastic models for representing viscoelastic materials. Hyperelastic models are a classification of elastic models used to represent soft tissues. In Hyperelastic models, an analytical function, called strain energy density (SED), is proposed to relate the stress tensor of materials to their strain rate. Examples of SED functions can be found in the comprehensive review paper of Chagnon et al. [29]. Hyperelastic models are widely used for modeling soft tissues [30–32]; however, they can only provide an approximated description for the behavior of biological materials as they ignore the viscous characteristics. In fact, these models, like other elastic models, cannot accurately predict some behavior of viscoelastic materials, such as creep and stress relaxation. Therefore, when the accurate characterization of tissue is of interest, elastic models are not appropriate, and instead viscoelastic models should be considered. In this document, we review two viscoelastic models that are widely-used for describing biological tissues.

Spring-dashpot models

Spring-dashpot models introduce a set of springs and dashpots for describing a material; the spring part is supposed to explain the elastic behavior and the dashpots

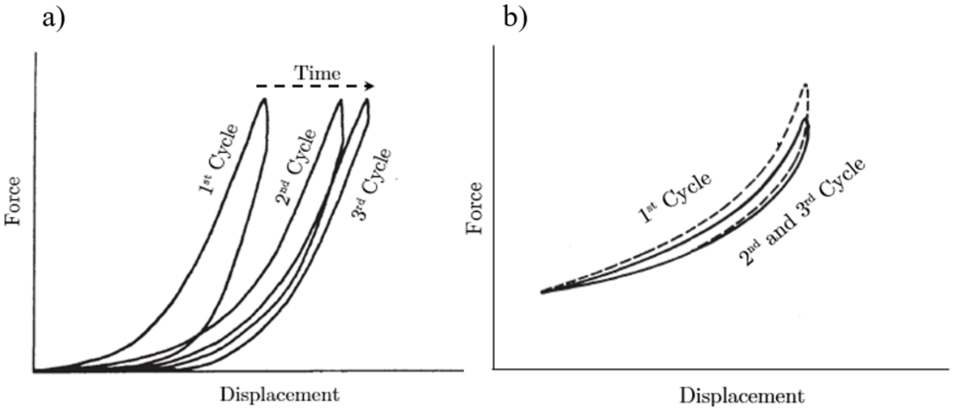

Figure 1.2: Time-dependent characteristic of tissue behavior: a) change in loading/unloading behavior of an anterior cruciate ligament through time; b) pre-conditioning of a dog's carotid artery. Reproduced with permission from [1].

represent viscous characteristics. The relation between force and strain in springs and dashpots can be either linear [2] or non-linear [12]. In their simplest forms, spring-dashpot models are comprised of a spring and dashpot which are placed either in series (Maxwell model) or parallel (Kelvin-Voight model). Figs. 1.3a and b display Maxwell and Kelvin-Voight models, each suggests two parameters, E and η , for describing the stress-strain relation. Complete agreement with experiments, however, is not usually achievable by tuning only two parameters. Therefore, multi-parameter models are often employed. In particular, the three-parameter model of Standard Linear Solid (SLS) is commonly used in the literature (Fig. 1.3c) [2]. Despite providing an appropriates relation for capturing the viscoelastic properties, spring-dashpot models are empirical and therefore lacking a physical basis [2]. This fact indicates that the parameters introduced for spring and dashpot coefficients are not necessarily meaningful. That is why the same tissue can be represented well by using two different spring-dashpot models [12, 33], each introduces different values for E and η. This problem has been discussed by Parker et al. [34] with the goal of reaching a consensus on the appropriate model for soft tissues. They concluded that, among linear viscoelastic models, fractional standard linear model and Kelvin–Voigt fractional derivative (KVFD) model pro-

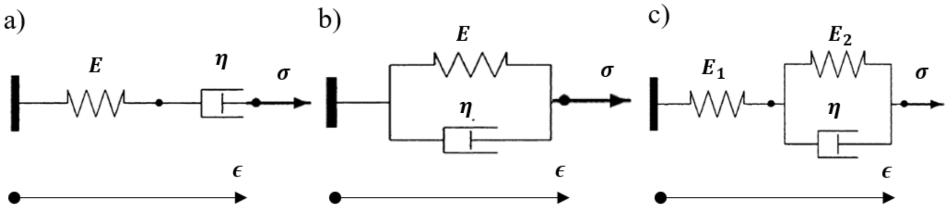

Figure 1.3: Different forms of spring-dashpot models; (a) Maxwell model, (b) Kelvin-Voight model, (c) Standard Linear Solid model. Reproduced with permission from [2]

vide the most meaningful description for viscoelastic behavior. Meanwhile, the properties obtained by these models are still dependent on the frequency by which the tissue is actuated; for example, the loss modulus given by Kelvin-Voigt model increases with frequency, which compromises the model's generality. It should be noted that having a physically interpretable model is essential when investigating actual properties of tissue. Therefore, it is necessary to introduce another viscoelastic model which has better biophysical background.

Quasi-linear Viscoelastic Model

To better describe the viscoelastic properties of materials, Fung introduced Quasi-linear Viscoelastic (QLV) in 1981 [1]. Unlike spring-dashpot models, the QLV model *characterizes tissues, as opposed to describing them.* In other words, spring-dashpot models describe the observed behavior of tissue by an arrangement of springs and dashpots while there is no guarantee that this description keeps its validity for other behavior of tissue. However, the QLV explores the relaxation characteristics, which are inherent properties of tissue, and so it provides a more valid model. This feature enables the QLV model to predict the non-linear behavior of viscoelastic materials, and to provide better estimations than spring-dashpot models. The QLV model calculates the stress by the convolution of two functions: one describes the elastic response, defined by Fung as the stress generated instantaneously after the deformation, and another accounts for the stress relaxation [1].

Fung's QLV model is shown to predict the non-linear characteristics of inelastic materials and provide an accurate representation for tissue. In this dissertation, we aim to use the QLV model for characterizing the prostate tissues. Nevertheless, correct implementation of the QLV model requires delicate considerations; disregarding those considerations caused some authors to mistakenly doubt the accuracy of the model [35]. For example, in order to preserve objectivity, the stress in the QLV model should be expressed by the second Piola–Kirchhoff stress form. Also, the determination of the functions for describing elastic stress and stress relaxation requires experimental elicitation so that the functions are derived independently from each other. The characterization of viscoelastic materials via the QLV model is discussed in the next section.

1.2 Material Characterization with the Quasi-linear Viscoelastic Model

After being introduced in 1981, the QLV model has been reappraised in later research works [35–37]. For example, the relaxation function that is originally suggested by Fung in 1981 is shown to results in viscoelastic parameters with large confidence intervals, which complicate material identification [37]. To avoid this problem, it was suggested to use a discrete spectrum approximation [38], which identifies a limited number of relaxation timescales over which a discrete spectrum represents the relaxation behavior. The QLV model with a discrete spectrum relaxation function has been widely used for modeling soft tissues ([37–40]). Using a discrete approach though cannot guarantee the reliability of the QLV parameters, especially when the model parameters increase and cause overfitting. This may explain why Calvo-Gallego et al. [40] concluded that the stress relaxation in adipose tissue is maximal after 0.01 seconds, which contradicts the experimental findings. There have been attempts in the literature to provide enhanced techniques for calibrating the QLV parameters. Yang et al. [39] normalized the data by using the differences between the peak and post-relaxation stresses and checked if the QLV parameters fit the normalized and denormalized stresses. A similar approach was followed in the works of Xu et al.[41] and Babaei et al. [37]. Alternatively, Troyer et al. [42] separated the elastic and relaxation terms of the QLV model by assuming a Heaviside strain form and derived the elastic and relaxation parameters independently. While they addressed the overfitting problem by reducing the parameters being fitted at a time, the deviation of the actual strain from the Heaviside form challenges their parameters' validity.

Material characterization by the QLV model requires experimental data that express the force feedback under specific deformation. Different deformation protocols, including unconfined compression, tension, torsion, and indentation can be considered for this purpose, but because of its simplicity, indentation is often the preferred method [43]. In an indentation test, the tissue is pressed by a small indenter (i.e., a flat punch) and the mechanical properties are derived from the force-displacement relationship. The test is simple and appropriate for in vivo assessments of tissues with various sizes and geometries [43]. In addition, its non-invasive nature preserves the tissue's physiological structure while showing the actual properties [44].

QLV Characterization by Indentation Test

Researchers have tried to incorporate analytical indentation models into the QLV analysis, and for example, Kermani et al. [45] substituted Sneddon's model for the elastic part of the QLV formulation. The authors predicted the behavior of porcine aorta using nanoindentation tests with a conical indenter. Other researchers have used spherical indenters in either nanoindentation [46] or traditional (macro) indentation tests [47]. Flat-ended tips, however, are more commonly used in indentation tests as they 1) can keep a constant contact area during the indentation, and 2) lead to higher forces compared to those obtained with spherical or conical tips at the same depth [48]. Ling et al. [43] used a flat-ended indentation test to characterize foot plantar tissue by substituting the QLV relaxation modulus in Hayes' solution. Similarly, Qiu et al. [49] derived the properties of breast cancer tissue with a flat punch indentation test. In this work, the QLV shear modulus was replaced with the shear modulus in Fischer-Cripps's indentation model. The same method was also adopted by Zheng Mak [50] and Huang et al. [51] to calculate the properties of biological tissues by applying the QLV model in indentation tests. In any case, the literature suggests that analytical indentation models cannot accurately model biological tissues as the reported properties differ from those obtained from uniaxial compression tests [52–54]

Finite element (FE) methods are more accurate for studying indentation tests as they can model the three-dimensional deformation that occurs during the indentation. Moreover, ABAQUS software has been widely used as an FE tool for this purpose. Seyf et al. [55] derived elastic and viscous properties of meniscus tissue using the inverse FE method and the QLV model in ABAQUS. In inverse FE methods, FE analyses are conducted iteratively with different parameters until the results match the experiment. Nevertheless, inverse FE methods are time-consuming, especially when it comes to 3D modeling. Consequently, attempts have been made to improve the speed of the inverse FE method when QLV is considered. For example, Kim and Srinivasan [56] separated the characterization of elastic and viscous parameters to enhance the model's speed, which could be completed in a few hours. In another study, Pierrat et al. [57] found elastic parameters from pre-computed FE simulation data, and then used a one-dimensional QLV model to derive the viscous parameters. By using pre-computed data, the authors introduced a method that was sufficiently rapid for real-time characterizations.

In this dissertation, we aim to use the QLV model to characterize the elastic and viscous characteristics of prostate tissue and study the effect of cancer on the mechanical properties. The effect of cancer on the viscoelasticity of prostate has been the subject of many research works, which some of them are reviewed in the next section.

1.3 Effect of Cancer on Mechanical Properties of Prostate Tissue

As mentioned earlier, imaging shear waves after an actuation is a common method for mapping the mechanical properties of soft tissues (i.e., shear wave elastography (SWE)). Using ultrasound SWE, Boehm et al. [58] recorded the elasticity of the prostate gland for 60 patients and concluded that cancerous tissues are two times stiffer than normal tissues. Their study included the samples with cancer grades[1] ranging from one (Gleason Score 3+3) to four (Gleason Score 4+4). In another work, Fu et al. [59] concluded that prostate tissue with a Gleason Score of 10 is four times stiffer than the tissue with a Gleason score of 6. A similar trend of works on elasticity of prostate tissue can be found in the recent review paper by Anbarasan et al. [60]. Like elastic properties, viscous properties affect the propagation of shear waves, and so neglecting them leads to inaccurate estimations [61]. While there are multiple studies on applying SWE to map viscoelastic properties of soft tissues [15, 62, 63], to our best knowledge, there is only one targeting prostate tissue, in which Mitri et al. [64] incorporated Kelvin-Voigt models with shear wave equations to obtain the shear elasticity and viscosity for non-cancerous prostates. Characterizing three freshly excised prostates from cadavers, they demonstrated that the elasticity and viscosity of the prostates for different people are not similar.

---

[1] International Society of Urological Pathology (ISUP) Cancer Grade

Alternatively, MRE can be used to capture the waves propagation speed after an actuation. Hu et al. [65], for instance, applied MRE to derive the stiffness of prostate using a 3 Tesla scanner and SWE techniques. Their results showed that PCa stiffness increases over 30% when cancer metastasis occurs. A similar approach has been followed by Asbach et al. [66] to differentiate PCa with cancer grade 1 and above (Gleason score $\geq$ 3+3) from benign prostate hyperplasia (BPH). Estimating shear wave speed as a measure of stiffness, they concluded that prostates show 10% more stiffness under PCa than BPH. Some other works on exploring elastic properties of the prostate with MRE have been reviewed by Pepin et al. [67]. The MRE research works that include viscoelastic properties are also frequent. As an example, Li et al. [68] derived viscoelasticity of prostate, and showed that cancerous prostate tissue is tree times stiffer and more viscous than prostatitis tissue. Another example is the work of Reiter et al. [69], who compared storage and loss moduli between normal and cancerous prostate. Their results showed that the complex shear modulus for the cancerous prostates with Gleason scores ≥ 3 is two times more than healthy tissues. Some other similar works include those of Reiss-zimmermann et al. [70] and Asbach et al. [66], who reported complex shear modulus to study prostate viscoelasticity. In line with other similar works, their results concluded that the stiffness and viscosity of prostate tissue increase in the presence of cancer.

The research works above describe the viscoelastic properties by using spring-dashpot models that, as discussed earlier, are not reliable since the reported properties are dependent on the arrangement of spring and dashpot elements and also the frequency that the tissue is actuated. That is to say, the tissue properties obtained from different actuation frequencies are not comparable. For example, the results of Reiter et al. [69] and Li et al. [68] cannot be compared as the former uses 500 Hz actuation while the latter used 100 Hz actuation. In this dissertation, for the first time, we propose a novel method for calibrating the QLV model and characterize the mechanical properties of soft materials. This method is different from previous methods that presented for QLV characterization in two aspects. First, we consider the elastic stress as the one that emerges after a sufficiently long time, when the time-dependent viscous part of stress vanishes, and the steady-state elastic part remains. This is different from Fung's traditional definition for elastic response: the stress generated instantaneously after the deformation [1]. Our definition for the elastic response can reduce the undesirable effect of overshooting on the parameter estimation as it removes the focus on the immediate stress response [71]. Second, the elastic and relaxation parameters are being derived separately using two different sets of experiments: one for representing the elastic response and another for the relaxation response. As a result, the number of fitting parameters decreases, and hence overfitting does not occur. The current method is shown to derive the QLV parameters with narrow confidence intervals. We validate our method using tissue-mimicking phantoms, with elastic properties that resemble normal and cancerous prostate tissues. The application of the method for material characterization via indentation test is also discussed by introducing a straightforward procedure for characterizing viscoelastic materials. We then apply our method for deriving the elastic and viscous properties of cancerous and normal prostate tissue and study the effect of cancer of the QLV parameters. Our results demonstrate that the cancer has statistically significant effect on the stiffness and shear relaxation modulus of the prostate.

1.4 Dissertation Organization

The rest of the dissertation is organized as follows: in Chapter 2, we provide a new method for calibrating the QLV model using uniaxial compression experiment. The method is shown to obtain the parameters with small confidence interval, independently from the loading conditions. We applied the method on tissue-mimicking phantoms to validate its applicability for biological tissues. Chapter 3 presents a procedure for characterizing the QLV parameters from indentation experiment. Using pre-calculated finite element results, we show the material parameters are obtained in a few seconds, with good accuracy (error withing 20%) and precision (standard error within 10%). The findings of Chapters 2 and 1 are then applied for finding the viscoelastic properties of normal and cancerous prostate tissue in Chapter 4. Having tested thirty-five fresh, unfixed prostate samples, we investigated the effect of cancer on the elastic and viscous properties of cancer and performed hypothesis testing to find the significance of findings. Finally, Chapter 5 concludes the findings and discuss future work.

Chapter 2

Quasi-linear Viscoelastic Calibration of Soft Materials via Uniaxial Test

This chapter [1] provides a new method for calibrating the QLV parameters from the uniaxial compression test (one-dimensional stress-strain state). The findings will be used as a base in the following chapter for calibrating the parameters from indentation test (three-dimensional stress-strain state).

This chapter is organized as follows: first, we provide the constitutive equations for one-dimensional QLV model and provides an approximated analytical solution. The QLV equations are then solved numerically to provide a better description for the viscoelastic characteristics of materials. Finally, based on the numerical solution provided, we present a characterization method for deriving the Young's modulus and shear relaxation modulus from uniaxial compression test, and validate our method by testing on phantoms with similar Young's modulus as normal and cancerous prostate tissue.

---

[1] The results of this chapter were published in: ”H. Helisaz, M. Bacca, and M. Chiao, “Quasi-Linear Viscoelastic Characterization of Soft Tissue-Mimicking Materials,” ASME J. Biomech. Eng., vol. 143, no. 6, Jun. 2021, doi: 10.1115/1.4050036.”

2.1 Methods and Materials

2.1.1 QLV Model in One Dimension

The parameters of the QLV model can be obtained via calibration from uniaxial stress relaxation experiments, where the sample is compressed at high rate and then wait for stress to be fully relaxed. We apply a compression strain ε and measure the evolution of the stress σ over time t. The stress state is uniaxial and σ can be described as:

$$\sigma(t) = \int_0^t \phi(t-\tau)\frac{\partial \varepsilon(\tau)}{\partial \tau}d\tau \tag{2.1}$$

where ϕ identifies the constitutive behavior of materials. The QLV model proposes [1]:

$$\phi(t) = G(t)\frac{\partial \sigma_E(\varepsilon)}{\partial \varepsilon} \tag{2.2}$$

with G, the relaxation function, is a function related to the viscous (rate-dependent) response of the material and σ_E is a function related to its elastic behavior. The latter corresponds to the true (Cauchy) stress of the material under quasi-static deformation, and it can be obtained from hyperelastic constitutive models. We use a one-term Ogden model to determine σ_E, which has been shown to predict the elastic response of human tissue accurately [72]. Note that the one-term Ogden model can describe the behavior of materials under fully compressive or fully tensile experiments while characterizing the whole compression-tension behavior requires at least two terms [72]. Assuming incompressibility, the axial compression $\lambda = 1 - |\varepsilon|$ generates an elastic Cauchy stress σ_E of [40]:

$$\sigma_E(\lambda) = -\mu\left(\lambda^{\alpha} - \frac{1}{\lambda^{\alpha/2}}\right) \tag{2.3}$$

where μ and α are the materials' constants related to the elastic modulus E as follows:

$$E = \frac{3}{2}\mu\alpha \tag{2.4}$$

In compression tests, the applied deformation follows a ramp-and-hold function (see Fig. 2.1c). Hence, the deformation increases from $t = 0$ to $t = \tau_0$, and remains constant for t $\geq t = \tau_0$, where $t = \tau_0$ is determined by the compression rate.

This implies that for $t \geq t = \tau_0$ the applied strain rate is zero, reducing the integral bounds on the right-hand side of Eq.(2.1). Also, the rate of change of ε per unit time in Eq. (2.1) is equivalent to that of the axial compression λ; hence, the substitution of Eq. (2.2) into Eq. (2.1) gives:

$$\sigma(t) = -\int_0^{\tau_0} G(t-\tau) \frac{\partial \sigma_E(\lambda)}{\partial \lambda} \frac{\partial \lambda(\tau)}{\partial \tau} d\tau \tag{2.5}$$

G describes the time-dependent behavior of the material as a stiffness decay. Fung proposed the following relaxation function to describe the relaxation behavior of biological soft tissues [1]:

$$G(t) = \frac{1+\kappa\left[\mathrm{Z}_1\left(t/v_2\right) - \mathrm{Z}_1\left(t/v_1\right)\right]}{1+\kappa \ln\left(v_2/v_1\right)} \tag{2.6}$$

where v_1, v_2, and κ are viscoelastic material coefficients and Z_1 is defined as follows:

$$\mathrm{Z}_1(t) = \int_t^{\infty} \frac{e^{-t}}{t} dt \tag{2.7}$$

Eq. (2.6), however, prohibits the numerical integration of Eq. (2.5) [38] and will lead to viscoelastic parameters with large confidence intervals [37]. To avoid these problems, we consider the Prony's series below as a discrete spectrum approximation for the relaxation function [38]

$$G(t) = 1 + \sum_i g_i e^{-t/\tau_i} \tag{2.8}$$

where g_is are shear relaxation moduli created by the viscous response of the material decaying to zero at the rate defined by the relaxation time τ_i. Eq. (2.8) has been shown to well represent Fung's relaxation function when relaxation times spread one decade apart [38]. Substituting Eqs. (2.8), (2.4), and (2.8) into Eq. (2.5), we finally have:

$$\sigma(t) = -\frac{2E}{3} \int_0^{\tau_0} \left[1 + \sum_i g_i e^{-(t-\tau)/\tau_i}\right] \left(\lambda^{\alpha-1} + \frac{1}{2\lambda^{\alpha/2+1}}\right) \frac{\partial \lambda(\tau)}{\partial \tau} d\tau \tag{2.9}$$

This integro-differential equation is solved numerically, as explained in the next section.

We now try to find the analytical solution of Eq. (2.9) for a specific condition of super-fast compression. By use of the mean value theorem for integrals, a time τ_m exists with $0 \leq \tau_m \leq \tau_0$, for which Eq. (2.5) can be rewritten as:

$$\sigma(t) = -\tau_0 G(t - \tau_m) \frac{\partial \sigma_E(\lambda(\tau_m))}{\partial \lambda} \frac{\partial \lambda(\tau_m)}{\partial t} \tag{2.10}$$

For fast compression, we have $\tau_0 \ll \tau_i \; \forall i$; that is, the "compression time" τ_0 is much smaller than the relaxation timescales. This also implies $\tau_m \ll \tau_i \; \forall i$ and so $G(t - \tau_m)$ from Eq. (2.8) can be approximated by $G(t)$. Rewriting Eq. (2.10), we have:

$$\sigma(t) \approx -\tau_0 \left(1 + \sum_i g_i e^{-t/\tau_i}\right) \frac{\partial \sigma_E(\lambda(\tau_m))}{\partial \lambda} \frac{\partial \lambda(\tau_m)}{\partial t} \tag{2.11}$$

The stress in Eq. (2.11) is maximal at the beginning of the stress relaxation process, at $t = \tau_0$, giving:

$$\sigma_{\max} = \sigma(\tau_0) \approx -\tau_0 \left(1 + \sum_i g_i\right) \frac{\partial \sigma_E(\lambda(\tau_m))}{\partial \lambda} \frac{\partial \lambda(\tau_m)}{\partial t} \tag{2.12}$$

and it reaches the steady-state when stress relaxation is completed at $t \to \infty$, giving:

$$\sigma_{\text{steady}} = \sigma(\infty) = -\tau_0 \frac{\partial \sigma_E(\lambda(\tau_m))}{\partial \lambda} \frac{\partial \lambda(\tau_m)}{\partial t} \tag{2.13}$$

Equating Eqs. (2.12) and (2.13), we obtain the nominal amount of stress relaxation as:

$$\left| \frac{\sigma_{\max} - \sigma_{\text{steady}}}{\sigma_{\text{steady}}} \right| = \sum_i g_i \tag{2.14}$$

while at any j^{th} relaxation time τ_j we have:

$$\left| \frac{\sigma(\tau_j) - \sigma_{\text{steady}}}{\sigma_{\text{steady}}} \right| = \sum_i g_i e^{-\tau_j/\tau_i} \tag{2.15}$$

Eqs. (2.14) and (2.15) correlate the shear relaxation moduli to the amount of stress relaxation occurring in different time intervals; specifically, g_is measure the decrease in stress response between τ_{i-1} and τ_{i+1}. In our approach, the choice of relaxation times τ_i is arbitrary. As mentioned earlier, Eq. (2.9) has shown to be accurate for a choice of relaxation times as decades [40, 42, 73], that is when τ_{i+1} is ten times more than τ_i. We adopt the same testing protocol and try to find the material parameters (E, α and g_is) by fitting the experimental results with Eq. (2.9).

2.1.2 Data-Fitting Algorithm

This section presents our novel method for deriving the elastic and viscous parameters of materials by invoking the QLV model. We characterize the elastic behavior by prescribing displacements following the protocol shown in Fig. 2.1a. The compression at each step is then matched with the steady-state stress developed after relaxation (evidenced by the solid orange circles in Fig. 2.1b). The material is compressed by a displacement of 0.5 mm (∼ % 2.5 engineering strain) in each step and then maintained until the stress reaches a steady-state. The steady-state stress represents the *elastostatic* response as it excludes the time-dependent (viscous) part. In the following of this manuscript, we use elastic stress instead of elastostatic stress for the sake of simplicity. The figure has an inset showing the steady-state stresses that are fit to $\sigma_E(\lambda)$ from Eq. (2.3) to obtain μ and α and hence E (see Eq. (2.4)). Notably, the literature suggests deriving elastic properties, E and α, by fitting Eq. (2.9) with stress relaxation tests (Fig. 2.1d) [40, 73, 74]. Nevertheless, a stress relaxation test cannot characterize the elastic properties of the materials. In fact, including E and α in the curve fitting causes overfitting, which leads to incorrect parameters. Babaei et al. [37] reported that the QLV model can fit relaxation data by parameters that fail to predict the behavior of the material under other dynamic loadings.

We then substitute E and α in Eq. (2.9) and solve by deriving $\sigma(t)$ in terms of g_i, given τ_i as a priori. The experiments reveal that relaxation does not start before 0.01 seconds from the peak stress, at $t = \tau_0$, and terminates after 10 seconds. Hence, three relaxation times, τ_1, τ_2, and τ_3 are chosen so that $\tau_1 - \tau_0 = 0.1s$, $\tau_2 - \tau_0 = 1s$, and $\tau_3 - \tau_0 = 10s$ (see Fig. 2.1d). $G(t)$ is derived as:

$$G(t) = 1 + g_1 e^{-t/\tau_1} + g_2 e^{-t/\tau_2} + g_3 e^{-t/\tau_3} \tag{2.16}$$

The integral in Eq. (2.9) is solved numerically by invoking the Right Riemann sum formula with time intervals of 0.01 seconds. The solution expresses the stress in terms of shear relaxation moduli $g_i s$. We then derive g_1,g_2, and g_3 by fitting the solution with the experimental results (Fig. 2.1d). $g_i s$ characterize the viscous properties by determining the stress relaxation in specific time scales (see Eqs. (2.14, 2.15)). High-rate compression (30 mm⁄s) is considered in the experiment to enhance the accuracy of the QLV estimation [75]. The obtained g_i along with E and α define the QLV parameters required for material characteristics.

We fit the experimental results by minimizing the weighted least square error function as follows:

$$e = \sum_i W_i \left(\sigma_i^{\text{QLV}}(t) - \sigma_i^{\text{Exp}}(t) \right)^2 \tag{2.17}$$

where $\sigma_i^{\text{QLV}}(t)$ is the stress predicted by the QLV model (obtained by Eq. (2.9)) and $\sigma_i^{\text{Exp}}(t)$ is obtained by experiments; experiments provide stress in the time intervals of 0.01 seconds. We repeat the experiments three times for each sample and substitute the mean values as $\sigma_i^{\text{Exp}}(t)$. W_i is also the assigned weight for each data point. Larger weights are considered for the data points neighboring the stress peak due to smaller points in that region. In the first five points nearing the stress peak, $W_i = 50$ for the three middle points and $W_i = 20$ for the remaining two; $W_i = 1$ for other points. We use the interior-point algorithm performed by MATLAB function fmincon to minimize the error. However, the interior-point algorithm cannot guarantee a global minimum because of the non-convexity in the objective function [76]. The outcome of the interior-point algorithm is the local minimum around the initial guess, and so, it is highly sensitive to the first guess [40]. To address this issue, we adopt a two-step minimization. In the first step, we use a genetic algorithm (GA) by MATLAB function *ga* to estimate the global minimum in the space of the variables $g_i s$. GA starts from a set of random points distributed in the entire domain of $g_i s$ and finds a set of values for $g_i s$ where the error function is minimal. Nevertheless, the solution of the genetic algorithm is not optimal as it uses a heuristic method. Therefore, in the second step, we input the solution of the genetic algorithm as the initial guess for the interior-point algorithm to find the optimal values for $g_i s$. To confirm that the minimization algorithm is consistent for a given choice of relaxation times, we repeat the algorithm ten times with the same τ_i and compare the derived values for $g_i s$. While the estimation of GA is different

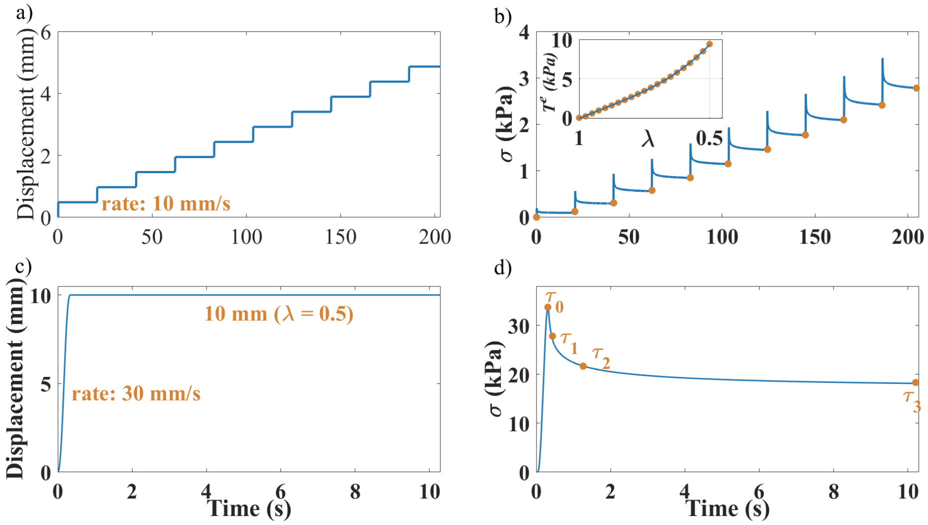

Figure 2.1: Experimental procedure: (a) a series of low-range compressions: each is a 2.5% strain and kept long enough until the stress reaches the steady-state; (b) stress response versus time under the prescribed displacement at (a): elastic properties are obtained by plotting the steady-state stress (orange dots) against the compression; (c) ramp-and-hold compression with 50% final strain: strain is kept long enough until the stress reaches the steady-state; (d) stress response versus time under the prescribed displacement at (c): the stress amplification factors g_1 and g_2, and g_3 measure the stress relaxation in the time intervals (τ_0, τ_1), (τ_1, τ_2), and (τ_2, τ_3)

each time, the final solution provided by the interior-point algorithm is same and insensitive to the initial guess. A similar procedure is followed for finding E and α by fitting Eq. (2.3) to the elastic response from the experiments (see Fig. 2.1b).

2.1.3 Tissue-Mimicking Phantoms

We evaluated the ability of the QLV model to characterize the phantoms shown in (Fig. 2.2). The phantoms were fabricated by mixing a silicon-based polymer and cross-linker in the presence of platinum as a catalyst. We used the commercially available elastomer kits Ecoflex™ 00-10 and Ecoflex™ 00-30 (Smooth-On Inc., Pennsylvania, U.S.). The mechanical properties of the elastomers are tailored by changing the concentrations of cross-linker and polymer. Having less cross-linker than polymer results in a smaller number of polymer chains and a softer elastomer [77]. A non-reactive silicone fluid NOVOCS™ (Smooth-On Inc., Pennsylvania, U.S.) was also added to further adjust the properties. The silicone fluid decreases the friction between the polymer chains and leads to a lower viscosity. It also reduces the relative concentration of cross-linker with respect to polymer and hence the ultimate stiffness. The elastomers were fabricated so that Young's modulus of Elastomer I matches with that suggested by the literature for normal prostate tissue (15-20 kPa) [78], and Elastomers II and III mimic that of cancerous prostate tissue (24-40 kPa) [78]; the composition and the properties of the elastomers are listed in Table 2.1 and Table 2.2. Unlike the elastic properties, the viscous properties of normal and cancerous prostate tissues have not been well established [79, 80]. The findings of the few available studies on the viscosity of prostate tissues are also not comparable as they reported different parameters for representing viscosity [79, 81]. Therefore, we cannot confirm whether the viscous properties of our phantoms resemble those of normal and cancerous prostate tissues. To fabricate the phantoms, we mixed the polymer, cross-linker, and silicone fluid for one minute, degassed the mixture for 10 minutes in a 30 kPa vacuum, and waited overnight for the solution to cure at room temperature. All samples had a cylindrical shape with a diameter of 25.2±0.24 mm and a height of 19.9±0.30 mm (Fig. 2.2). The color pigment (Silc Pig™, Smooth-On Inc., Pennsylvania, U.S.) was added to distinguish the elastomers.

Table 2.1: The composition of tissue-mimicking phantoms

	Ecoflex™ 00-10	**Ecoflex™ 00-30**	**NOVOCS™**
Elastomer I	0%	67%	33%
Elastomer II	0%	80%	20%
Elastomer III	100%	0%	0%

2.1.4 Method Validation and Confidence Interval

We compare the relaxation behavior for one of the tissue-mimicking phantoms (Elastomer III) with that predicted by the QLV model. The phantom is subject to

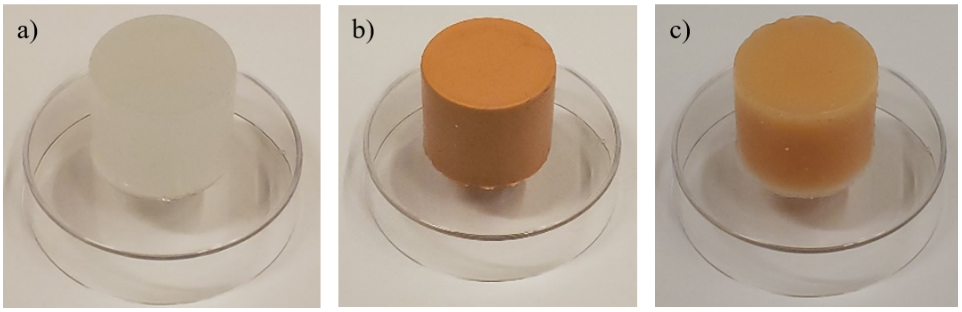

Figure 2.2: Tissue-mimicking phantoms: (a) Elastomer I (67% Ecoflex™ 00-10 and 33% NOVOCS™); (b) Elastomer II (80% Ecoflex™ 00-30 and 20% NOVOCS™); c) Elastomer III (100% Ecoflex™ 00-10): Elastomer I mimics normal tissue in terms of Young's modulus while elastomers II and III mimic cancerous tissues.

Table 2.2: The QLV parameters for tissue-mimicking phantoms; 95% confidence intervals are reported

	α	**Young's Modulus**	g_1	g_2	g_3
Elastomer I	2.63 ± 0.03	16.0 ± 0.1kPa	0.31 ± 0.03	0.08 ± 0.01	0.01 ± 0.00
Elastomer II	2.53 ± 0.03	33.0 ± 0.1 kPa	0.15 ± 0.02	0.18 ± 0.00	0.00 ± 0.00
Elastomer III	3.70 ± 0.01	28.5 ± 0.0 kPa	0.87 ± 0.03	0.46 ± 0.01	0.00 ± 0.00

four different compression strains, i.e. $\varepsilon = 30\%, 40\%, 50\%$ and 60% (Fig. 2.3a). The QLV parameters are obtained by fitting the theory to the experimental results for 50% compression strain. We then use the same parameters for describing the behavior of the same material under 30%, 40%, and 60% strain levels and compare our prediction with the experimental results (Fig. 2.3b). The experiments were performed by the mechanical tester Mach-1 V500CS (Biomomentum Inc., Laval, QC, Canada). The tester has the multiple-axis load cell MA234 (Biomomentum Inc.) with a range of 35 N, a resolution of 1.75 mN, and a recording rate of 100 Hz. The load cell is connected to the phantom by a compression plate with a diameter of 25 mm (Fig. 2.4). The compression plate has slightly larger size than the samples to guarantee a uniaxial stress state. Also, the lateral force of the loadcell is monitored to confirm a friction-less boundary condition between tissue and the fixture plates. As shown in Fig. 2.3, QLV can well predict the phantom's relaxation behavior under different loading conditions. The observed discrepancy between the theoretical

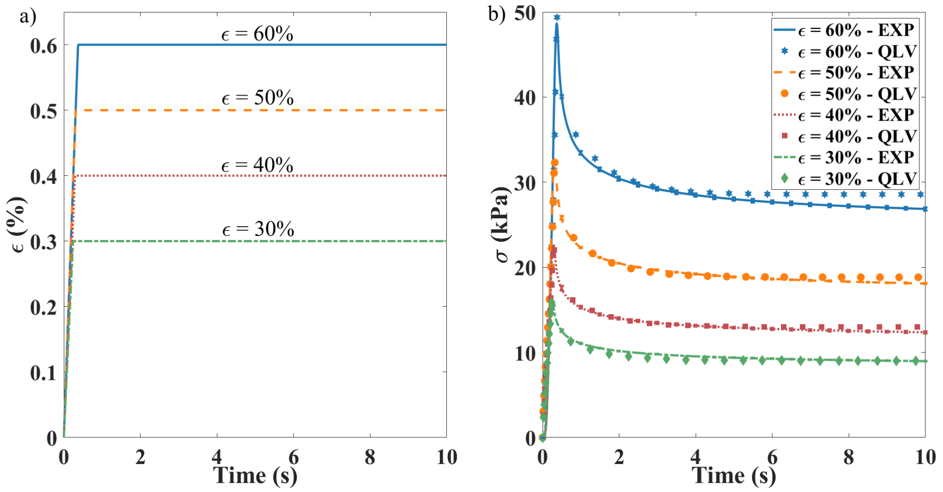

Figure 2.3: Model validation: a) ramp-and-hold compression with different final strains; b) stress response of Elastomer III versus time under the prescribed displacement at (a): lines are experimental results while symbols denote predictions of the QLV model (Eq. (2.9)). The experiments are repeated three times for each sample, and the mean values for the results are presented with the error bars.

and experimental results is partly because of considering a limited number of relaxation times (see Eq. (2.16)). One can enhance the model's accuracy by considering more relaxation times but at the expense of increasing the number of calibration parameters. It should be noted that, however, considering more relaxation times does not guarantee a perfect fit to the experiments, because, like any other model, the QLV model has its own limitations. In particular, the model assumes that the effects of strain and time on the viscoelasticity are separable (see Eq. (2.2)), which does not perfectly represent the materials' characteristics.

To measure the reliability of the QLV model, the confidence intervals of the parameters in Fig. 2.3 are determined by using the method described by Yin et al. [82]. Using this method, we first create sixty-four new data sets (like that of Fig. 2.1d) that could be observed in the experiments. Then, we calculate $g_i s$ for each of the new data to obtain a population for $g_i s$ values, from which confidence intervals are measured. For finding the new set of data, we calculate the differences between the experimental stress response with that predicted by the QLV model to draw a residual plot. It is assumed that the residual stress is the sum of a smooth error representing systematic error and a rough error rendering experimental noise. Assuming that the systematic errors can be derived by fitting a polynomial function to residual plot [82] , we obtain the noise as the difference between the residual stress and systematic error. We use eight polynomial functions to represent the systematic error, and for each, we obtain a random noise distribution. Then, the systematic error functions and noise distributions are paired and added to the stress predicted by the QLV model. This creates sixty-four new data whose systematic error and noise distributions could be observed in the experiments. Finally, we implement our data fitting algorithm to calculate the relaxation parameters for the new data set and find the confidence intervals. The 95% confidence intervals for the relaxation parameters are obtained for Elastomer III under different strain levels (Table 2.3). The table shows the relaxation parameters for different strain levels have a good agreement proving our method's ability to predict the behavior of materials under different loading conditions. As expected, more difference is observed between the parameters of the lowest and highest strain levels. This can also be seen in Fig. 2.3 where the parameters for $\varepsilon = 50\%$ predict the behavior of $\varepsilon = 40\%$ better than $\varepsilon = 30\%$ and $\varepsilon = 60\%$. (Table 2.3) confirms a narrow confidence interval for all reported parameters.

Table 2.3: 95% confidence intervals for relaxation parameters of Elastomer III under different strain levels (see Fig. 2.3)

	g_1	g_2	g_3
$\varepsilon = 30\%$	0.74 ± 0.06	0.51 ± 0.01	0.05 ± 0.00
$\varepsilon = 40\%$	0.84 ± 0.05	0.46 ± 0.01	0.00 ± 0.00
$\varepsilon = 50\%$	0.87 ± 0.03	0.46 ± 0.01	0.00 ± 0.00

2.2 Results and Discussion

We used the process described in the previous section to characterize the tissue-mimicking phantoms. The identification of viscoelastic materials requires detecting both elastic and viscous properties. In particular, distinguishing between normal and cancerous prostate tissue involves extracting both properties as cancer can

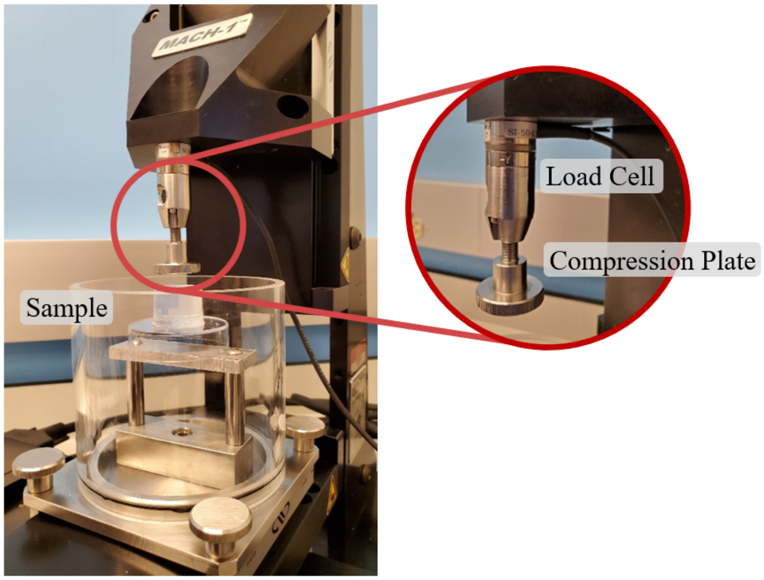

Figure 2.4: Testing machine used to obtain stress response of materials: a custom compression has slightly larger diameter than samples to guarantee a uniaxial compression force.

change either. The uncontrolled proliferation of cancer cells generates compressive stress in the tissue, which causes an increase in the stiffness [83]. On the other hand, the depletion of collagen in the presence of cancer changes the time-dependent behavior of tissue and hence its viscous properties [84]. Cancer effect on the mechanical properties of prostate tissue will be discussed more in Chapter 4.

Mixing a non-stoichiometric ratio of cross-linker and polymer leaves some molecules unattached to the network (unreacted monomers) or attached only at one end (dangling chains). The movement of monomers and dangling chains under deformation causes a time-dependent behavior [77]. The ramp-and-hold compression (shown in Fig. 2.1c) compels the monomer molecules to move between the polymer chains. Nevertheless, the movement is resisted by viscosity, which is high at the beginning and diminishes over time until the stress reaches a steady state. That is why we observe a peak stress in Fig. 2.1d, which is followed by a gradual stress relaxation over time. The amount and duration of stress relaxation depend on the concentration of the unreacted monomers and the structure of the dangling chains [77]. We used the QLV model to calculate the amount and rate of stress relaxation, based on which a material can be identified.

Fig. 2.5 illustrates the relaxation behavior of the elastomers. We identified the phantoms based on the shear relaxation modulus g_i, which reflect the stress relaxation in (τ_{i-1}, τ_{i+1}) intervals (see Eqs. (2.14) and (2.15)). The 95% confidence intervals for QLV parameters are listed in Table 2.2. The table demonstrates that our method derives the QLV parameters with narrow confidence intervals. In particular, our confidence interval for Young's modulus is a third of that reported by Abramowitch and Woo [75], who used Fung's original continuous spectrum for QLV analysis. The parameters are also more reliable as we derive E and α based on the steady-state stress (see Fig. 2.1b), as opposed to instantaneous stress that is associated with overshooting errors [71]. Gimbel et al. [71] have shown that a 10% overshoot in the strain input results in a more than 30% error in the QLV parameters.

The QLV parameters for the elastomers are listed in Table 2.2 and Fig. 2.5. Table 2.2 demonstrates that the shear relaxation moduli ($g_i s$) can well characterize Elastomers II and III that have similar Young's moduli but different viscous properties. The higher stress relaxation in Elastomer III is reflected in a larger g_1, g_2. The table also compares the rate of stress relaxation in the elastomers: while Elastomer II relaxes the same amount of stress in intervals (τ_0, τ_1) and (τ_1, τ_2), Elastomer III does twice as much in the first interval. Both elastomers have negligible stress relaxation in the third interval (τ_2, τ_3). These results reflect the potential of our method for distinguishing materials with similar elasticity (Young's modulus) but different viscous properties.

The stress relaxation behavior of Elastomer I is also demonstrated in Fig. 2.5. Elastomers I and II are fabricated with the same polymer and cross-linker; however, the larger amount of silicon fluid in Elastomer I decreases the viscosity and leads to a higher stress relaxation rate in the early time interval. Also, Elastomer I shows a smaller Young's modulus than Elastomer II, reflecting the lower concentration of polymer and cross-linker (see Table 2.2). We compare Young's modulus derived from the QLV model with that represented by the linear regression of the steady-state stress-strain data (orange dots in the inset of Fig. 2.1b). Linear regression is implemented by invoking the MATLAB function *fitlm*. Young's modulus is calculated from the experimental data of up to 40% strain, where the stress-strain behavior of phantoms is still in the linear region [85]. The measured Young's moduli from linear regression match with those predicted by the QLV model.

As explained in the previous section, the relaxation times $\tau_i s$ are selected knowing (from experiments) that no stress relaxation occurs in the first 0.01 seconds and after 10 seconds. To culminate this section, we examine the outputs of the QLV model without considering this *a priori* information. For this purpose, we should add two more relaxation times to consider stress relaxation before 0.01 seconds and after 10 seconds. Thus, τ' and τ'' are added where $\tau' - \tau_0 = 0.01s$ and $\tau'' - \tau_0 = 100s$. Having these two relaxation times in Eqs. (2.8) and (2.9), we re-fit the experimental data to Eq. (2.9) and re-obtain the stress amplification factors. The results show that the amplification factors corresponding to the time intervals (τ', τ_0) and (τ_3, τ'') are negligible and other $g_i s$ match the previous results. That is to say, the QLV model works well even with no *a priori* information about the relaxation behavior of materials.

While the proposed method demonstrates the potential for characterizing soft materials, some limitations exist. First, the derived parameters and the accuracy of the data fit depend on the choice of relaxation times. One can improve the accuracy of data fit by considering more relaxation times but at the expense of increasing calibration parameters. Also, the QLV model assumes that the effects of time and strain on the material's viscoelasticity are separable, which is not necessarily true for all the materials. That is to say, when the proposed model does not demonstrate an acceptable agreement with the actual behavior of a material, one should consider using another model.

2.3 Summary

This chapter presents a method for characterizing the QLV properties of soft materials using uniaxial compression test. Unlike the previous approaches for calibrating the QLV model, we use two different experimental data for deriving elastic and viscous parameters separately. Our method can reduce the negative effect of overshooting on the estimation of the QLV parameter. The proposed model is shown

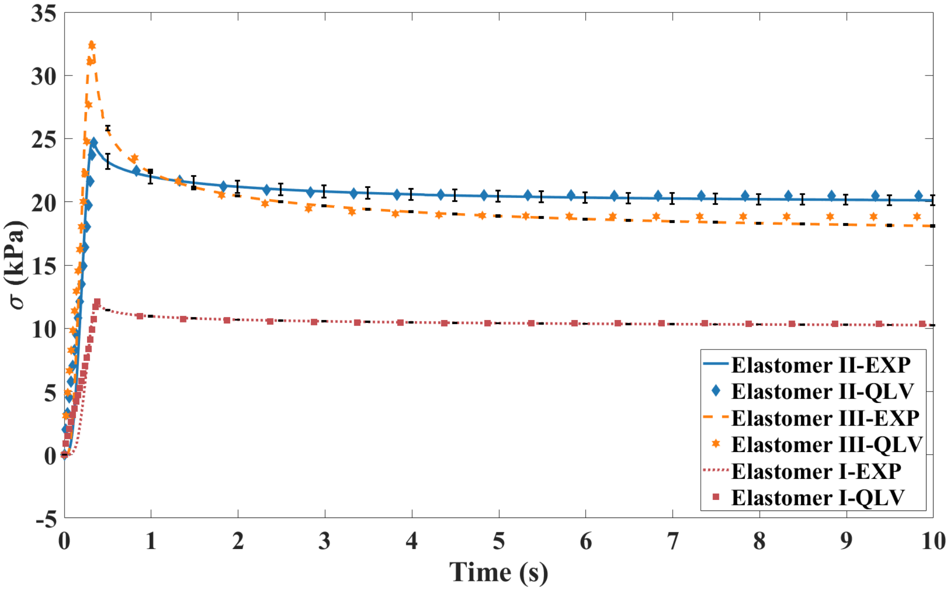

Figure 2.5: Material characterization: lines are experimental results while symbols denote predictions of the QLV model (Eq. (2.9)). QLV parameters, including α, E, and g_i, can well distinguish the phantoms. The experiments are repeated three times for each sample, and the mean values for the results are presented with the error bars.

to characterizes the material by parameters with narrow confidence intervals (high accuracy), independently from the loading conditions. Hence, it represents an improvement with respect to other viscoelastic models (e.g., spring-dashpot models) that introduce different parameters for each loading condition [12, 33]. To test our method, we developed low-cost tissue-mimicking materials that match Young's modulus of healthy and cancerous prostate tissues. Characterization of these samples with our method allows for a precise distinction between materials having similar elastic (viscous) properties but different viscous (elastic) properties. However, the uniaxial compression test is not always applicable for *in-vivo* applications. Also, compressing the whole tissue may cause some irreversible damages. For clinical applications, indentation test is recommended as 1) it can be applied on tissues with various size and geometries [43], and 2) it is non-invasive and so preserves the tissue's structure [44]. Unlike uniaxial compression test, the indentation test causes three-dimensional stress-strain fields and so Eq. (2.1) is not valid. Therefore, a procedure is required to extend the proposed method to a three-dimensional field, which is discussed in the next chapter.

Chapter 3

Quasi-linear Viscoelastic Characterization of Soft Materials via Indentation Test and Finite Element Analysis

In this chapter[1] we present a new method for characterizing the QLV parameters of viscoelastic materials via indentation test. Using pre-calculated finite element analysis on three-dimensional stress-strain field, our method is able to obtain the parameters in a few seconds that suggest its application in real-time.

This chapter is organized as follows: first, we provide the equation for three-dimensional QLV model and a finite element approach for solving the equation. The finite element method is implemented in ABAQUS® by invoking a user material subroutine (UMAT). We validate our finite element simulation with experimental results and then use it for studying the indentation stress response of a material under different QLV parameters, indentation depths, indenter sizes, and indentation rates. Our results, for the first time, demonstrate that

---

[1] A form of this chapter were published in: ”H. Helisaz, M. Bacca, and M. Chiao, “A New Characterization Procedure for Quasi - Linear Viscoelastic Materials Using Indentation Test: Validation with Finite Element and Experimental Results,” Exp. Mech., no. 0123456789, 2022, doi: 10.1007/s11340-022-00837-7.”

- Indentation depth and indenter size do not have effect on the stress relaxation behavior of materials in indentation test
- Each QLV parameters has a specific (and quantifiable) effect on the stress relaxations over different time intervals
- Stress relaxation is linearly correlated with the shear relaxation moduli

Based on these findings, we propose a procedure for material characterization using an indentation test with a flat-ended tip. The procedure provides a straightforward approach for material characterization that is significantly faster than inverse finite element methods. Finally, we evaluate the accuracy of the procedure by characterizing the same material once with the procedure and once again with the method described in Section 2 and compare the parameters. Our procedure is shown to have high precision (standard deviation less than 10%) and good accuracy (error less than 20%).

3.1 Methods and Materials

3.1.1 Three-dimensional QLV Constitutive Equation

The equation presented in Eq. (2.1) is only valid for one-dimensional stress-strain field and it cannot be used for indentation test. In three dimensions, QLV-based constitutive models describe the stress tensor $\boldsymbol{S}(t)$ in terms of 2$^{\text{nd}}$ Piola-Kirchhoff: [35, 86]

$$\boldsymbol{S}(t) = \boldsymbol{S}_E(t) : \boldsymbol{G}\left(0^+\right) + \int_0^t \boldsymbol{S}_E(\tau) : \frac{\partial \boldsymbol{G}(t-\tau)}{\partial (t-\tau)} d\tau \tag{3.1}$$

where $\boldsymbol{S}_E$ is the elastic stress response, emerging at steady-state, which is expressed in the form of 2$^{\text{nd}}$ Piola-Kirchhoff [35]. The colon operator ($:$) also represents the double dot product. In the general case, the Cauchy stress tensor is obtained from:

$$\boldsymbol{\sigma}(t) = J^{-1}\boldsymbol{F}(t)\boldsymbol{S}(t)\boldsymbol{F}(t)^T \tag{3.2}$$

where $\boldsymbol{F}$ is the deformation gradient tensor (bold letter indicates a tensor) and $J = det(\boldsymbol{F})$ is volumetric stretch and $\boldsymbol{S}$ is obtained from Eq. (3.1). Considering isotropic relaxation behavior, i.e., stress relaxation behavior is the same in all dimensions, the reduced relaxation tensor in Eq. (3.1) becomes the scalar function $G(t)$, and the equation is rewritten as:

$$\boldsymbol{S}(t)=\boldsymbol{S}_E G\left(0^{+}\right)+\int_0^t \boldsymbol{S}_E(\tau)\frac{\partial G(t-\tau)}{\partial(t-\tau)}d\tau \tag{3.3}$$

Assuming a hyperelastic constitutive model for predicting elastic stress, $\boldsymbol{S}^e$ is derived as follows:

$$\boldsymbol{S}_E=2\frac{\partial\psi}{\partial\boldsymbol{C}}-P\boldsymbol{C}^{-1} \tag{3.4}$$

where ψ is the strain energy density function, and P is the hydrostatic pressure. $\boldsymbol{C}$ is also the right Cauchy-Green deformation tensor, defined as $\boldsymbol{C}=\boldsymbol{F}^T\boldsymbol{F}=\sum_{i=1}^3\lambda_i^2\boldsymbol{C}_i\otimes\boldsymbol{N}_i$ with λ_i^2 and N_i the i$^{\text{th}}$ eigenvalue and eigenvector of $\boldsymbol{C}$, respectively, and $\otimes$ the outer product symbol. Note that λ_i represents the principal stretch applied in the i$^{\text{th}}$ direction. Linear elastic compressibility gives P as a function of bulk modulus κ:

$$p=\kappa(J-1) \tag{3.5}$$

Therefore, one can enforce incompressibility ($J=1$) by selecting a large value for bulk modulus since, as $\kappa\to\infty$, J should approach one to provide a finite value for P. Because large κ can cause instability in the simulation, the remedy is to select an appropriate finite element mesh. Here, we assume incompressibility by adopting $\kappa\geq 10^4\mu$. A one-term Ogden model expresses the strain energy density as:

$$\psi=\frac{2\mu}{\alpha^2}\left(I_1\left(\boldsymbol{C}^{\alpha/2}\right)-3\right) \tag{3.6}$$

where I_1 represents the first invariant (trace) of the tensor. Substituting Eq. (3.6) into Eq. (3.4) we have:

$$\boldsymbol{S}_E=\left(\frac{2\mu}{\alpha}\boldsymbol{C}^{\alpha/2}-p\right)\boldsymbol{C}^{-1} \tag{3.7}$$

Note that $\boldsymbol{C}$ is a symmetric matrix, and so $\frac{\partial}{\partial\boldsymbol{C}}I_1\left(\boldsymbol{C}^{\alpha/2}\right)=\boldsymbol{C}^{\alpha/2-1}$. The relaxation function in Eq. (3.3) can be represented by a Prony's series presented in Eq. (2.8). One can substitute Eqs. (3.7) and Eq. (2.8) into Eq. (3.3), and solve the integral with the trapezoid method as follows:

$$\begin{aligned}\boldsymbol{S}(t) =&\boldsymbol{S}_E\left(1+\sum_{k=1}^{n} g_k\right)-\frac{\Delta t}{2}\sum_{j=1}^{n-1}\sum_{k=1}^{N}\\ &\left[\boldsymbol{S}_E\left(t_j\right)\frac{g_k}{t_k}e^{-\frac{\left(t-t_j\right)}{t_k}}+\boldsymbol{S}_E\left(t_{j+1}\right)\frac{g_k}{t_k}e^{-\frac{\left(t-t_{j+1}\right)}{t_k}}\right]\end{aligned} \tag{3.8}$$

where the subscript j specifies the variable calculated at $t = t_j$. Substituting Eq. (3.8) in Eq. (3.2), one can derive the expression for three-dimensional Cauchy stress for an incompressible, isotropic material. The finite element implementation of Eq. (3.8) will be discussed in the following section. To incorporate Eq. (3.8) into the commercial software ABAQUS®, we also need to calculate the elasticity tensor $\boldsymbol{\ell} = \partial\boldsymbol{\sigma}/\partial\boldsymbol{\varepsilon}$ where ε is the strain tensor. This can be derived by transforming $\mathscr{L} = 2\partial\boldsymbol{S}/\partial\boldsymbol{C}$ using the gradient tensor. Assuming incompressibility, $\mathscr{L}$ has the following index form [87]:

$$\ell_{ijhk} = F_{ip}F_{jq}F_{hr}F_{ks}\mathscr{L}_{pqrs} \tag{3.9}$$

where ℓ_{ijhk} is the component i, j, h, k of l; F_{ij} is the component i, j of ; $\mathscr{L}_{ijhk}$ is the component i, j, h, k of $\mathscr{L}$; and repeated indices indicate a sum. Differentiating S in Eq. (3.8) with respect to $\boldsymbol{C}$ results in the following expression for tensor $\mathscr{L}$:

$$\mathscr{L} = 2\frac{\partial\boldsymbol{S}_E}{\partial\boldsymbol{C}}\left(1+\sum_{k=1}^{n} g_k-\frac{\Delta t}{2}\sum_{k=1}^{N}\frac{g_k}{\tau_k}\right) \tag{3.10}$$

Note that all of the terms in the sum over the time steps ($\sum_{j=1}^{n-1}\sum_{k=1}^{N}[\ldots]$ in the second term) are eliminated except the last term since the derivation is calculated at time $t = t_n$ [88]. The derivative of $\boldsymbol{S}_E$ in Eq. (2.7) with respect to C results in the following expression:

$$\frac{\partial\boldsymbol{S}_E}{\partial\boldsymbol{C}} = \mu\left(1-\frac{2}{\alpha}\right)\boldsymbol{C}^{\alpha/2-2}+P\boldsymbol{C}^{-2}-\frac{\partial P}{\partial\boldsymbol{C}}\boldsymbol{C}^{-1} \tag{3.11}$$

where, from Eq. (3.4), $\frac{\partial p}{\partial\boldsymbol{C}} = \kappa\frac{J}{2}\boldsymbol{C}^{-1}$. Further calculations for $\frac{\partial S^e}{\partial\boldsymbol{C}}$ are available in the works of Connolly et al. [89]. For the sake of brevity, we do not repeat the calculations here and refer the reader to these references. To incorporate Eq. (3.3) and Eq. (3.10) into ABAQUS®, the FE approach needs to be implemented for these equations, which is discussed in the next section.

3.1.2 Finite Element Implementation

ABAQUS® is able to model finite-strain viscoelasticity by splitting stress into volumetric and deviatoric parts (see Abaqus Theory Manual Version 6.11, section 4.8.2 and [90]). In particular, the QLV model can be implemented in ABAQUS® by combining built-in hyperelastic models (for elastic properties) and Prony's series (for viscous properties). Meanwhile, the expression for Prony's series in ABAQUS is different from Eq. (2.8) (see ABAQUS Analysis User's Guide Version 6.12, section 22.7.1). Using the ABAQUS's expression, the elastic part in the QLV formula is defined as the instantaneous stress, which appears immediately after the deformation (see ABAQUS Analysis User's Guide Version 6.12, section 22.7.1). This differs from the current formula that defines elastic stress as that which emerges at steady-state (see Eq. (3.1) and Section 2.1). The steady-state stress happens when viscous part of the stress vanishes, and the purely elastic part remains, and so we believe it is a better representative of the elastic stress. Also, unlike instantaneous stress, steady-state stress only depends on the strain and the parameters of the material, and not on the indentation speed. So, we translate Eqs. (3.2) and (3.9) into ABAQUS® using a UMAT subroutine in Fortran. The UMAT was written based on the program by Connolly et al. [87] for simulating hyperelastic materials. We modified their code so that it can model quasi-linear viscoelastic materials. Fig. 3.17 demonstrates the flow chart for the algorithm we used in the UMAT. The software receives material properties and deformation gradients as inputs and calculates Cauchy stress (Eqs. (3.2) and (3.8)) and the elasticity tensor (Eqs. (3.9) and (3.10)) as outputs. The material properties, including the coefficients for the hyperelastic model and Prony's series, are inputted by the user, and the deformation gradient is calculated at each timestep by ABAQUS. Then, the UMAT calculates the right Cauchy-Green tensor $\boldsymbol{C}$ and its eigenvalues α^2 and eigenvectors $\boldsymbol{N}$. The Ogden strain energy density ψ is also calculated and its first-order derivative is computed. Having the parameters for Prony's series (g and τ), the code estimates

2$^{\text{nd}}$ Piola-Kirchhoff stress from Eq. (3.8) and converts it to Cauchy stress using Eq. (3.2). Note that the summation term in Eq. (3.8) requires storing the information from previous steps. For this purpose, we define state variables (STATEV) to store the normal and shear components of stress in three dimensions. Finally, the software finds $\mathscr{L}$ by substituting $\frac{\partial S^e}{\partial C}$ from Eq. (3.11) and obtains the elasticity tensor ℓ from Eq. (3.9).

The UMAT described in Fig. 3.17 is translated into ABAQUS 2018 by Intel's Parallel Studio (XE 2018) compiler. The axisymmetric model shown in Fig. 3.1a is created in ABAQUS by including a deformable part, as the soft material, and a rigid analytical part, as the indenter. The deformable part is supported from the bottom by a rigid analytical layer with the encastre boundary condition. All contacts in the model are assumed to be frictionless and hard contacts. We use linear quadrilateral mesh elements (CAX4H) for the deformable part and perform a mesh independence analysis to ensure that the solution is independent of mesh size. The model includes two steps: first, the indenter compresses the material by imposing a displacement boundary condition. The indentation rate is controlled by tailoring the step's time period. In the second step, the indenter remains at the same displacement and waits 10 seconds for stress relaxation. A fixed time increment size of 10^{-4} s is chosen for both steps to guarantee simulation stability. Each run takes around 10 hours, after which we derive the indenter's normal stress in the y-direction by averaging the stress of elements beneath the indenter.

3.1.3 Model Validation

Fig. 3.2 validates the results of the FE analysis with those obtained from the indentation experiment on a silicon-based polymer. We fabricated the polymer using the commercially available elastomer kit Ecoflex™ 00-10 (Smooth-On Inc., Pennsylvania, USA), following the procedure mentioned in Section 2.1. The fabricated material had diameter $D = 25$ mm and height $H = 18.88$ mm. The material's QLV parameters were then obtained by following the process described in the previous section. Table 3.1 lists the QLV parameters for the material, which was used in ABAQUS®. For the relaxation function, we selected three relaxation times: $\tau_1 = 0.1$ s, $\tau_2 = 1$ s, and $\tau_3 = 10$ s, same as Section 2.1.

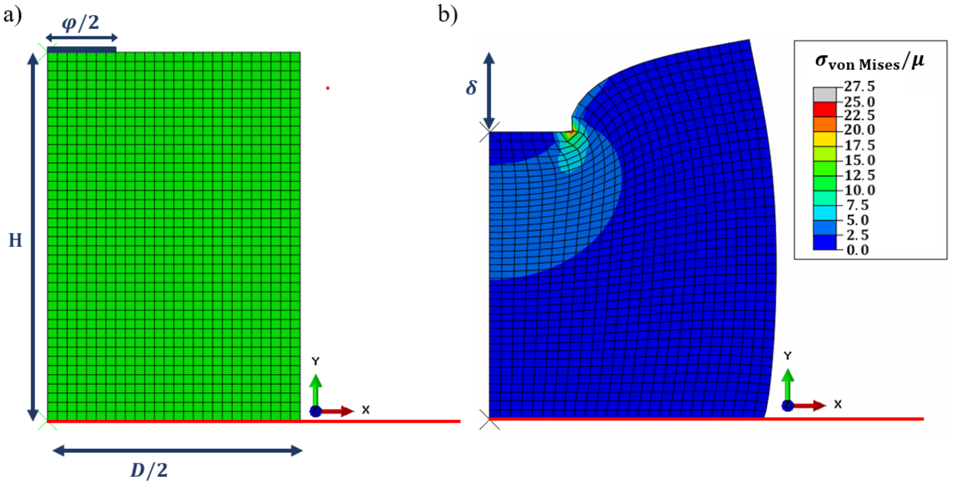

Figure 3.1: ABAQUS® simulation: a) axisymmetric model with a deformable part, for the soft material (shown in green), a rigid analytical part, for the indenter (shown in blue), and a rigid analytical part for the bottom support (shown in red); b) the indentation stress is expressed as von Mises stress; the indenter size φ and indentation depth δ are also shown in the figure. The results are depicted for φ = 7.60 mm, H = 18.88 mm, and D = 25 mm

Table 3.1: The QLV parameters of the fabricated silicon-based polymer; the parameters were obtained from uniaxial compression tests (see Chapter 2) and were used as the input for the ABAQUS® simulation.

α	μ	g_1	τ_1
5.39 ±0.07	3.98±0.02 kPa	0.33 ±0.10	0.1 s
g_2	τ_2	g_3	τ_3
0.48 ±0.02	1 s kPa	0.13±0.00	10 s

The mechanical tester Mach-1 V500CS (Biomomentum Inc., Laval, QC, Canada) was used to perform the indentation experiments. The tester was equipped with the multiple-axis load cell MA234 (Biomomentum Inc.) with a range of 35 N, a resolution of 1.75 mN, and a recording rate of 100 Hz. The load cell was connected to the material by an indenter. Multiple indenters were made with different diameters φ; i.e., φ = 4.95 mm, 6.33 mm, 7.60 mm, and 8.88 mm . The indenters were made of 316 stainless steel, which is considered rigid when contacting a soft material.

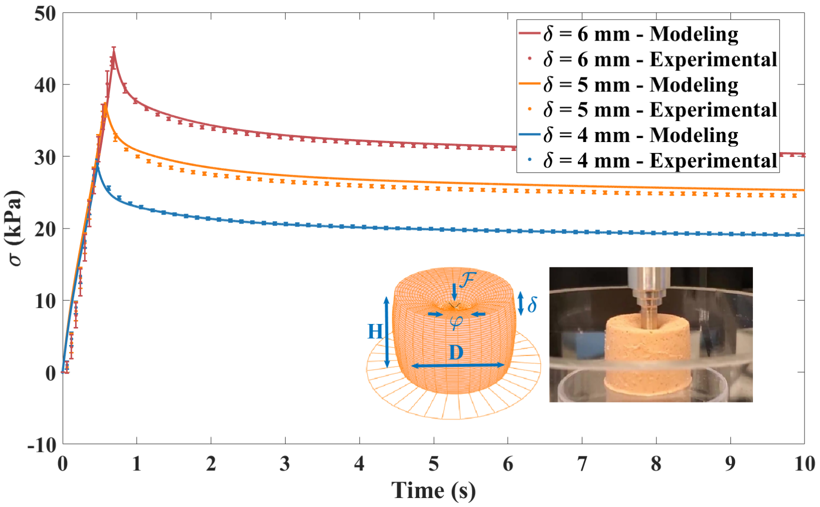

Figure 3.2: Model validation: The ABAQUS® simulation results are compared with those obtained from experiments on a silicon-based polymer. Lines denote the QLV model prediction, and the symbols are the experimental results. The experiment includes compressing an indenter into the specimen at a rate of 10 mm/s and recording the force response ($\mathscr{F}$). The force data is then converted to stress (σ) by dividing force by the indenter surface area ($\frac{\pi}{4}\varphi^2$). Each experiment is repeated three times, and the mean values for the results are depicted along with the error bars. The results are depicted for specimen height $H = 18.88$ mm, specimen diameter $D = 25$ mm, and indenter diameter $\varphi = 7.60$ mm

The specimen was supported by a petri dish from beneath. The indentation tests included fast compression of the sample at a rate of 10 mm/s for several indentation depths δ, and then waiting for 10 seconds for stress relaxation. The indentation force $\mathscr{F}$ was recorded by the load cell as the normal force component. Note that indentation force is not uniform and $\mathscr{F}$ represents the average stress beneath the punch. To ensure a frictionless contact, we compared $\mathscr{F}$ with and without lubricant, where no difference was observed (see Fig. 3.3). The ramp-and-hold indentation protocol compels the monomer molecules of the sample to move through the polymer chains. The movement, however, is resisted by the viscosity of monomers that causes a peak stress feedback at the beginning. As viscosity diminishes over time, the resistance against movement decreases, and stress relaxation starts until the stress reaches a steady-state. Fig. 3.2 compares the indentation stress obtained during the experiment with those predicted by ABAQUS® from simulation. The experimental stress was obtained by dividing the indentation force ($\mathscr{F}$) by the indenter surface area $\frac{\pi}{4}\varphi^2$. As shown in the figure, a good agreement is seen between the experimental and simulation results for different indentation depths δ. Fig. 3.2 is depicted for an indenter size of φ = 7.60 mm; the results for other indenter sizes also show a good agreement with the experiments (Figs. 3.4- 3.6). These results validate the applicability of the FE analysis that we developed in this section.

3.2 Results and Discussion

After the QLV finite element model was validated by experiments, we focused on simulating indentation experiments under different conditions. We changed the elastic (μ and α) and relaxation parameters (g_is) and investigated the indentation behavior over time. We also changed the indenter size, indentation depth, indentation tilt angle, and indentation rate to review the effects of loading condition on the indentation stress. We then used the findings to construct a general indentation procedure for characterizing viscoelastic materials without using inverse FE methods.

3.2.1 The Elastic Part of Indentation Behavior

Figs. 3.7a and b demonstrate the effects of μ and α on the indentation behavior, when $\varphi = 7.6$ mm and $\delta = 5$ mm. The relaxation coefficients are chosen to be $g_1 = 1$ and $g_2 = g_3 = 0$ for both figures. As expected for viscoelastic materials, we observe a peak stress followed by a stress relaxation over time until stress reaches a steady-state, which as mentioned earlier, represents elastic part of the stress. From this point forward in this manuscript, the steady-state stress is referred to as elastic stress and denoted by σ_E. The figure suggests a proportional effect for μ on the elastic stress, which is consistent with Eq. (3.6), where μ serves as a multiplier for the elastic stress. Unlike μ, the effect of α on elastic stress is nonlinear, which again, is expected from Eq. (3.6). Fig. 3.7 demonstrates that indentation stresses are sensitive to both μ and α. This result differs from those of Fellay et al. [91]

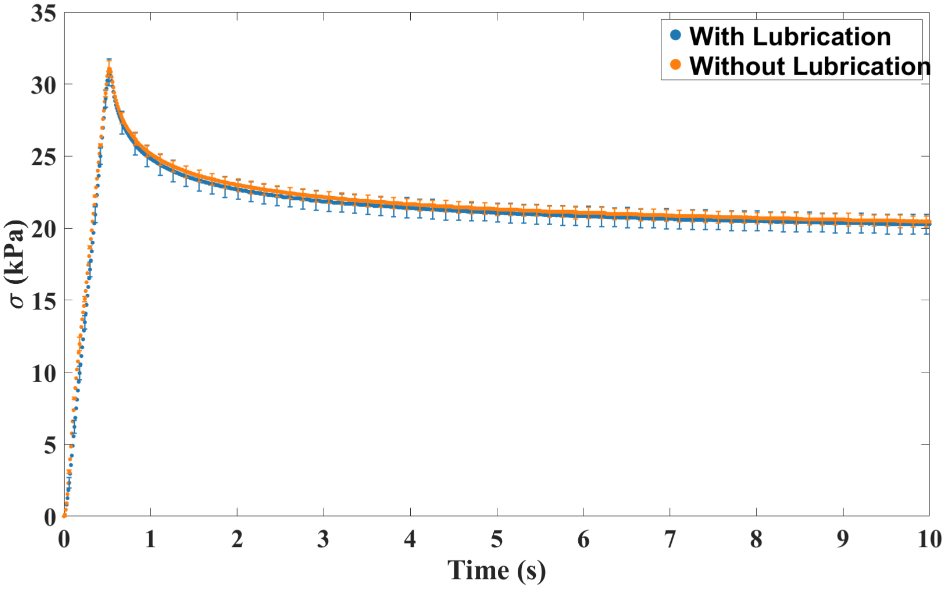

Figure 3.3: Comparing the stress feedback with and without using WD-40 silicone lubricant (WD-40 Company Inc., California, USA). The figure demonstrates no difference between the results, which confirms the frictionless contacts in the experiment. The symbols indicate the experimental results for a silicon-based polymer with height H=18.88 mm and diameter $D = 25$ mm.

who reported that the indentation stress remains unchanged for $\alpha \geq 2$. Considering the same stress for different values of α, the authors concluded that the indentation test is not able to characterize the materials with $\alpha \geq 2$. Our data in Fig. 3.7, however, show that the stress response is changing with α even when $\alpha \geq 2$, and so the indentation test can characterize the materials.

The results in Fig. 3.7 are depicted for a specific indentation diameter φ and indentation depth δ. In Fig. 3.8, we investigate the effects of φ and δ on the elastic stress. The figure displays the elastic stress for different sizes of indenter at different indentation depths. We nondimensionalize δ by φ and σ by μ. The results show that the relation between indentation depth and stress is non-linear. In addition, the curves for different indenter sizes do not collide after nondimensionalization, which deviates from the prediction of the analytical indentation models

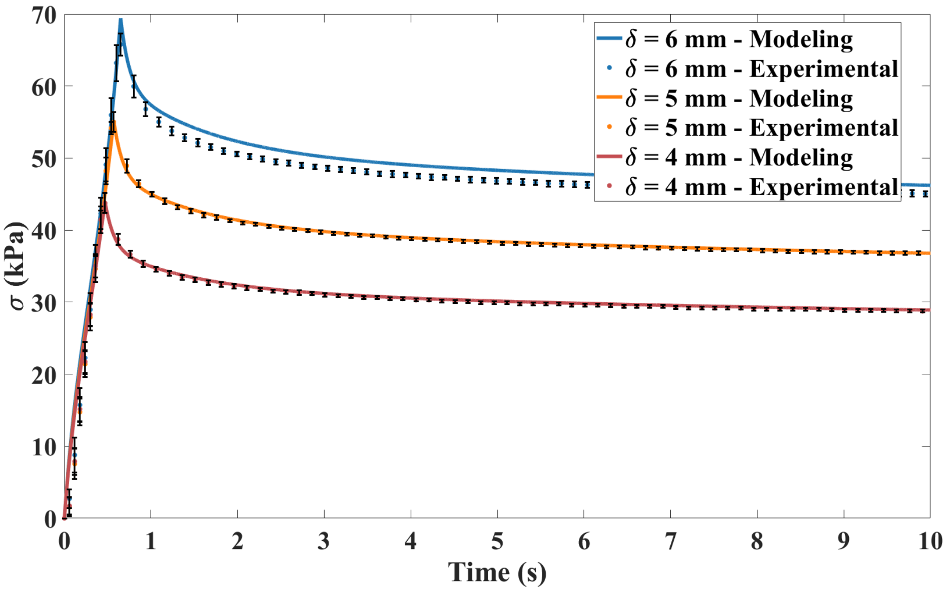

Figure 3.4: Model validation for indenter diameter $\varphi = 4.95$ mm: the ABAQUS® simulation results are compared with those obtained from experiments on a silicon-based polymer. Lines denote the QLV model prediction, and the symbols are the experimental results. The results are depicted for specimen height $H = 18.88$ mm and specimen diameter $D = 25$mm.

[54]. Attempts have been made to modify the analytical models for biological tissues, mainly by introducing a correction factor. For the sake of brevity, we do not repeat the same process here, and readers are referred to previous works [54, 92].

3.2.2 The Viscous Part of Indentation Behavior

In the QLV model, the effects of elastic and viscous parameters on the material's stress are assumed to be separable [35]. That is to say, $S_E(t)$ and $G(t)$ in Eq. (3.1) are independent. To reflect this separability, we nondimensionalize stress by σ_E in the figures to exclude the effect of elastic parameters, so the figures become independent of the values for μ and α. Fig. 3.9 demonstrates the evolution of nondimensionalized stress for different values of δ and φ, revealing that the relaxation behavior is the same for different values of indentation sizes and depths. Our

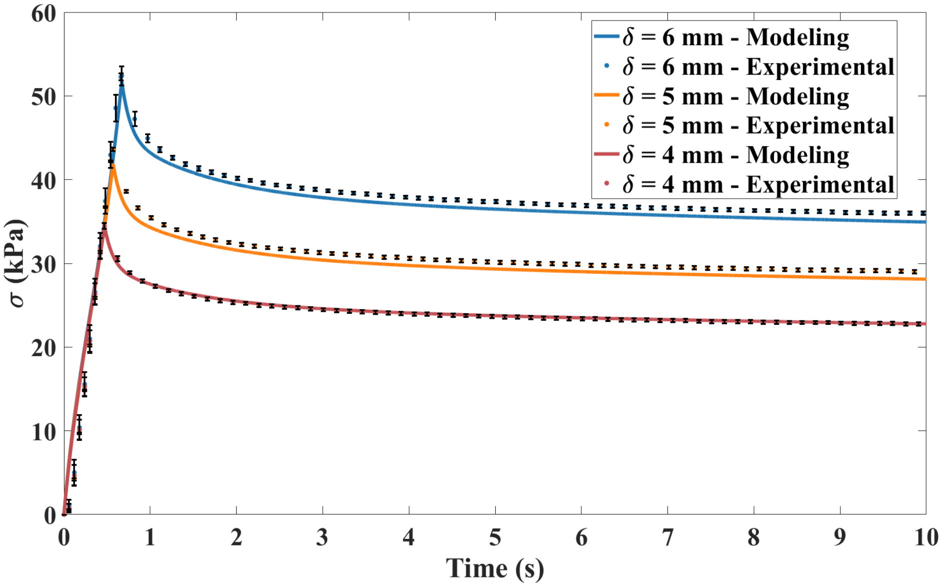

Figure 3.5: Model validation for indenter diameter $\varphi = 6.33$ mm: the ABAQUS® simulation results are compared with those obtained from experiments on a silicon-based polymer. Lines denote the QLV model prediction, and the symbols are the experimental results. The results are depicted for specimen height $H = 18.88$ mm and specimen diameter $D = 25$mm.

results demonstrate that the same is also true for tilted indentation, when the indenter is not aligned with contact surface normal (see Fig. 3.16). These observations are consistent with our reduced relaxation function (see Eq. (2.4)), where $G(t)$ is only dependent on time and scalar coefficients g_is and τ_is. The same relaxation behavior is hence expected in Figs. 3.9a-d since g_is and τ_is are the same.

Having the same relaxation behavior for different δ and φ is not necessarily true for materials that do not comply with the QLV model. In particular, different behaviors might be seen for materials whose elastic and viscous characteristics are not separable, such as collagenous soft tissues [93]. Comparing Fig. 3.8 and Fig. 3.9, one can conclude that relaxation behavior can serve as a better tool for material characterization than elastic behavior. That is because, unlike the former, the latter is dependent on the indentation size and depth, and so the effect of δ and

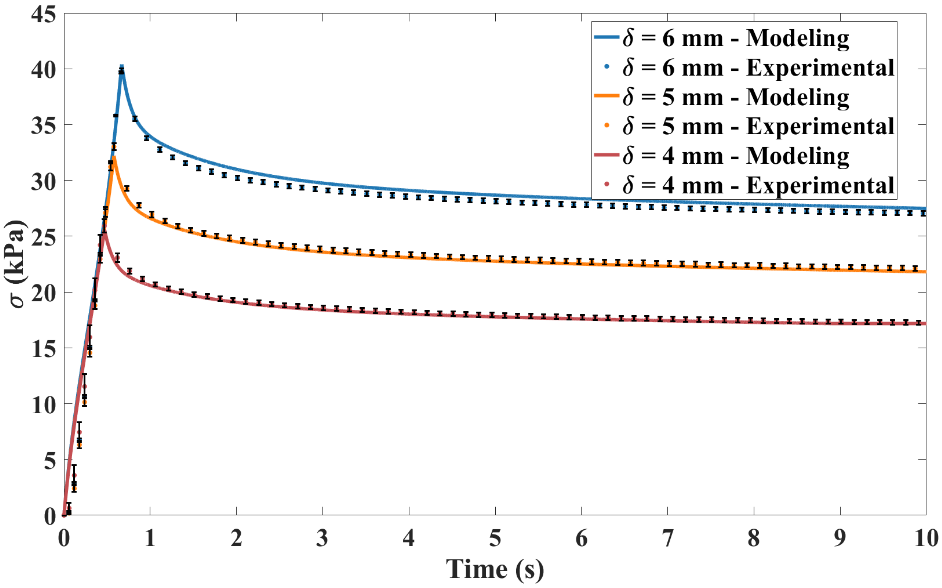

Figure 3.6: Model validation for indenter diameter $\varphi = 8.88$ mm: the ABAQUS® simulation results are compared with those obtained from experiments on a silicon-based polymer. Lines denote the QLV model prediction, and the symbols are the experimental results. The results are depicted for specimen height $H = 18.88$ mm and specimen diameter $D = 25$mm.

φ should be excluded before characterization.

Fig. 3.10 examines the effect of material properties on relaxation behavior. Fig. 3.10a, b, and c review the impact of g_1, g_2, and g_3, respectively. The results are expressed in the nondimensionalized form of $\hat{\sigma} = (\sigma - \sigma_E)/\sigma_E$. As seen in the figure, the stress relaxation is directly proportional to the value for g_i; the stress relaxation for $g_i = 2$ is twice that of $g_i = 1$. This observation is expected since g_is serve as scalar multipliers in the relaxation function (see Eq. (2.8)). Fig. 3.10d evaluates the relaxation behavior created by more than one relaxation coefficient. The results demonstrate that the stress relaxation associated with multiple g_is is derived by adding the stress relaxation made by each. For instance, the solid line in Fig. 3.10d is obtained by adding the red lines in Figs. 3.10a-c. Therefore, no cross-link effects occur between the stress relaxation coefficients g_is. A similar

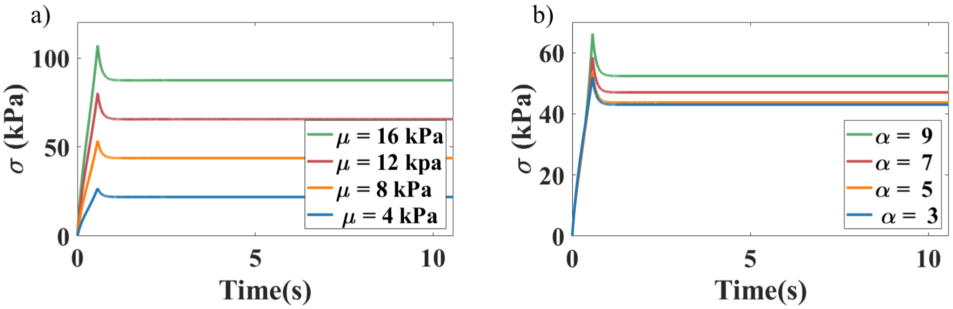

Figure 3.7: Effect of elastic parameters (μ and α) on indentation behavior: effect of a) shear modulus μ and b) strain-stiffen parameter α on the stress response of the material. The behavior shows a peak stress followed by stress relaxation until the results reach a steady-state. The steady-state stress occurs when the viscous properties of a material vanish, and only the elastic properties remain. The results demonstrate that the indentation stress is sensitive to both μ and α: it has a linear relationship with μ and a non-linear relationship with α.

conclusion was also reached by Amabili et al. [86], who introduced independent effects for relaxation coefficients under different directions.

The relaxation behavior of a material is influenced by the indentation time, which determines the time when stress relaxation begins (τ_0 in Fig. 3.11), and more stress relaxation is expected for lower indentation time. In particular, as it is shown in Section 2.1, when $\tau_0 \to 0$, stress relaxation reaches its maximum value $\sum_i g_i$. Fig. 3.12 plots the stress relaxation at different indentation rates. The results are obtained by keeping the indentation depth constant ($\delta = 5$mm) and changing the indentation time. τ_0 is nondimensionalized by τ_i to compare the indentation time against the relaxation times. As expected, we observe more stress relaxation for small values of τ_0, when the indentation rate is high. Interestingly, the figure shows that stress relaxation depends on the ratio of τ_i/τ_0 and not on individual values for τ_i and τ_0.

The relaxation behavior in Fig. 3.12 approaches one as the ratio of τ_i/τ_0 increases. This is consistent with our expectation for stress relaxation to reach $\sum_i g_i$ in super-fast indentation (when $\tau_i/\tau_0 \to \infty$). Our results reveal that when $\tau_i/\tau_0 \geq 10$, the indentation can be assumed to be super-fast, and the stress relaxation can be

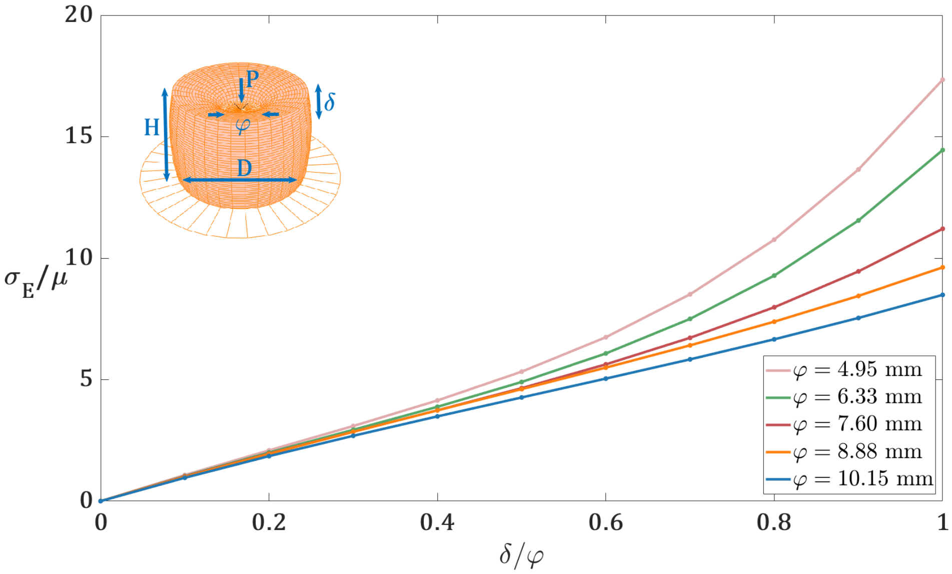

Figure 3.8: Effect of indenter size and indentation depth on the elastic stress of the material. The results are nondimensionalized to clarify the impact of each parameter; elastic stress is nondimensionalized with shear modulus μ and indentation depth δ with indenter diameter φ. Unlike the prediction of linear elasticity, the curves for different indenter diameters do not intersect, and the data suggests a non-linear relationship between stress and indentation depth. The results are depicted for specimen height $H = 18.88$ mm and specimen diameter $D = 25$ mm.

approximated as $\sum_i g_i$. That is to say, one can capture the full relaxation behavior when the indentation time is ten times smaller than the relaxation time. On the other hand, when the indentation rate is low ($\tau_i/\tau_0 \leq 10$), more than 80% of the stress relaxation is not perceived. Based on the data in Fig. 3.12, we recommend the indentation time to be $0.1\tau_m \leq \tau_0 \leq \tau_m$, where τ_m is the smallest relaxation time of the material, to ensure that at least 60% of the stress relaxation is captured.

Fig. 3.13 investigates the stress relaxation occurring in Fig. 3.12 during different time intervals. As described in Fig. 3.11, $\Delta\hat{\sigma}_{\tau_i - \tau_{i+1}}$), the normalized stress relaxation in the time interval $(\tau_i - \tau_{i+1})$, is obtained by subtracting the normalized stress at τ_i from that of τ_{i+1} $\left(\Delta\hat{\sigma}_{\tau_i - \tau_{i+1}} = \left(\sigma_{\tau_i} - \sigma_{\tau_{i+1}}\right)/\sigma_E\right)$. According to Fig. 3.13, the stress relaxation caused by g_i mostly occurs in (τ_{i-1}, τ_{i+1}), and for

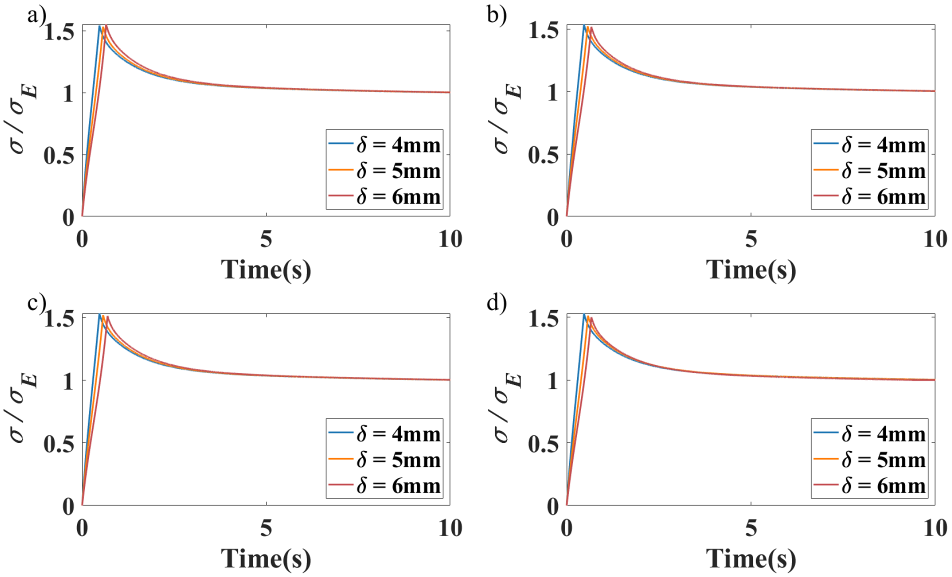

Figure 3.9: Nondimensionalized stress behavior for different indenter diameters and indentation depths: nondimensionalized stress response at indentation diameters of a) $\varphi = 4.95$ mm, b) $\varphi = 6.33$ mm, c) $\varphi = 7.60$ mm, and d) $\varphi = 8.88$ mm. The results demonstrate that relaxation behavior does not depend on the indentation size and depth.

example, the stress relaxation made by $g_1 = 1$ mainly occurs between τ_0 and τ_2. Furthermore, the stress relaxation in the last time interval ($\Delta\hat{\sigma}_{\tau_3-\infty}$) is affected only by the last coefficient g_3 because $\Delta\hat{\sigma}_{\tau_3-\infty}$ is zero when $g_1 = 1$ or $g_2 = 1$. Likewise, ($\Delta\hat{\sigma}_{\tau_2-\tau_3}$) is dependent on g_2 and g_3, and ($\Delta\hat{\sigma}_{\tau_1-\tau_2}$) is changing with all three g_is. As expected, the stress relaxation in different time intervals depends on the indentation rate, where a faster indentation rate (higher τ_i/τ_0) leads to more stress relaxation.

3.3 The New Material Characterization Procedure

Our results in Section 3.2 demonstrate that each g_i has specific effect on the stress relaxation which is proportionally related to the value for g_i (see Fig. 3.10). It has been also shown that the indentation depth and indenter size do not affect the stress relaxation (see Fig. 3.9). Based on these findings, we present a new method

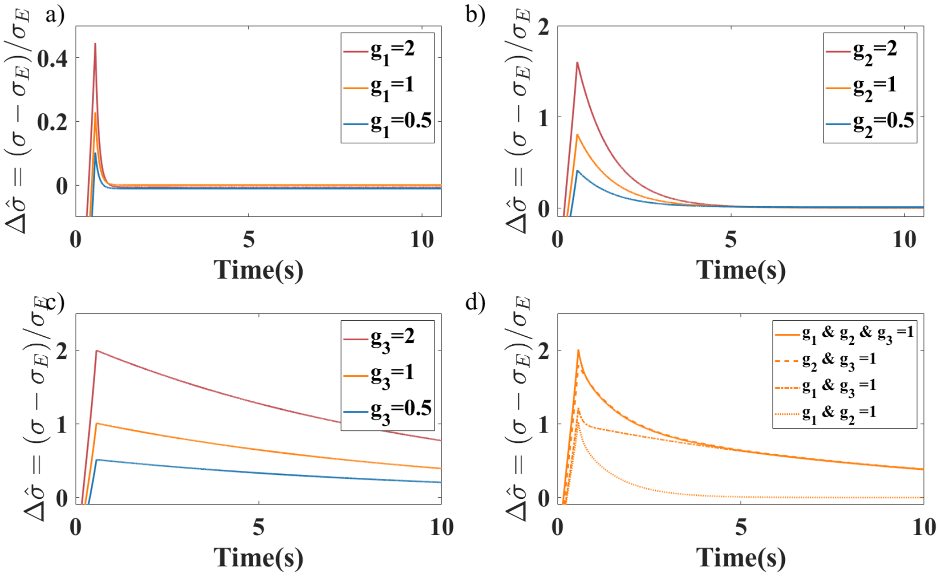

Figure 3.10: Effect of material properties on the viscous behavior: evolution of nondimensionalized stress relaxation over time for different values of a) g_1, b) g_2, and c) g_3: the results indicate that the stress relaxation is proportional to the value of g_is. The relaxation caused by $g_i = 2$ is two-times that of $g_i = 1$; d) the nondimensionalized stress relaxation associated with multiple g_is; the figure shows that the stress relaxation caused by several g_is is obtained by adding the stress relaxations made by each.

for deriving g_i from stress relaxation response of a material. Fig. 3.14 explains our suggested indentation procedure for material characterization. After recording the stress response of material from the indentation test (see Fig. 3.14a), we calculate the stress relaxation in different time intervals; i.e., $\Delta\hat{\sigma}_{\tau_1-\tau_2}$, $\Delta\hat{\sigma}_{\tau_2-\tau_3}$, and $\Delta\hat{\sigma}_{\tau_3-\infty}$. The results of Fig. 3.13 prove that stress relaxation in each time interval can be separated into three parts, each associated with one of the g_is; that is to say, $\Delta\hat{\sigma}_{\tau_i-\tau_{i+1}} = \sum_k \Delta\hat{\sigma}^{g_k}_{\tau_i-\tau_{i+1}}$ where the superscript g_k shows that the corresponding part is associated with g_k. Moreover, our findings in the previous section show that stress relaxation is proportionally related to the value for g_i, and so $\Delta\hat{\sigma}^{g_k}_{\tau_i-\tau_{i+1}} = g_k\Delta\hat{\sigma}^{g_k=1}_{\tau_i-\tau_{i+1}}$ where $\Delta\hat{\sigma}^{g_k=1}_{\tau_i-\tau_{i+1}}$ is stress relaxation created by $g_k = 1$ (see Figs. 3.14b-d). Therefore, we have:

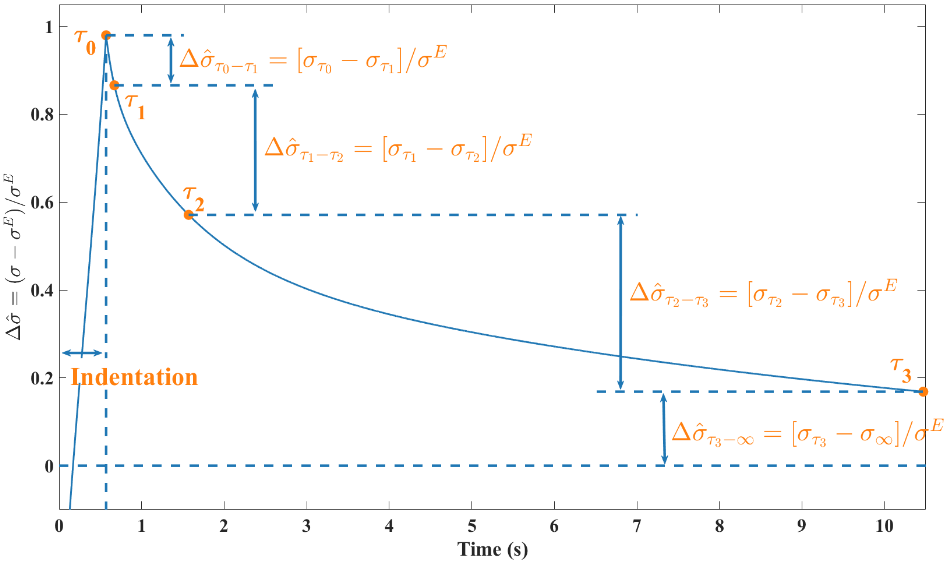

Figure 3.11: Stress relaxation in different time intervals: four time intervals are determined by τ_0, τ_1, τ_2, and τ_3, where τ_0 measures the indentation time and τ_1, τ_2, and τ_3 denote the relaxation times. The stress relaxation in the time interval (τ_{i-1}, τ_i) is obtained by subtracting the stress at $t = \tau_i(\sigma_{\tau_i})$ from the stress at $t = \tau_{i-1}(\sigma_{\tau_{i-1}})$. The data is nondimensionalized by the elastic stress σ_E.

$$\Delta\hat{\sigma}_{\tau_i-\tau_{i+1}} = \sum_{k=1}^{3} g_k \Delta\hat{\sigma}^{g_k=1}_{\tau_i-\tau_{i+1}} \tag{3.12}$$

where $\Delta\hat{\sigma}_{\tau_i-\tau_{i+1}}$ is obtained from the indentation experiment (Figs. 3.14a) and $\Delta\hat{\sigma}^{g_k=1}_{\tau_i-\tau_{i+1}}$ is calculated from simulation (Figs. 3.14b-d). Eq. (3.11) should be solved for three unknowns, g_is, which characterize the relaxation coefficients, g_is, without needing to invoke time-consuming inverse methods. It should be mentioned that the values given in Figs. 3.14b-d are valid for a specific indentation rate ($\tau_0 =$ 0.5 s). Figs. 3.15 shows the values for $\Delta\hat{\sigma}^{g_1=1}$,$\Delta\hat{\sigma}^{g_2=1}$, and $\Delta\hat{\sigma}^{g_3=1}$ at different indentation rates. Based on the indentation rate used in the experiment, one can find the corresponding values for stress relaxation and substitute them in Eq. (3.12) to derive g_1, g_2, and g_3.

We evaluated the accuracy of our method by comparing the parameters de-

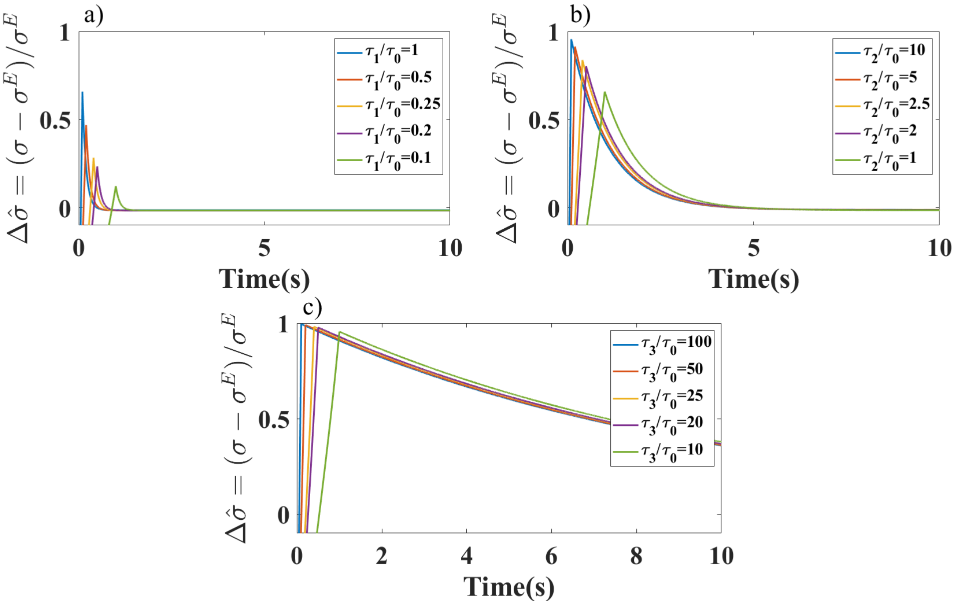

Figure 3.12: Effect of indentation rate on the viscous behavior: evolution of nondimensionalized stress relaxation over time when a) $g_1 = 1$, b) $g_2 = 1$, and c) $g_3 = 1$. The indentation rate is measured by indentation time τ_0, which is measured against τ_i. Stress relaxation increases as τ_i/τ_0 increases; in particular, when $\tau_i/\tau_0 \geq 10$, the indentation rate is sufficiently fast to fully capture the stress relaxation $(\sigma - \sigma_E/\sigma_E \approx 1)$. In addition, the stress relaxation is shown to depend on τ_i/τ_0 and not on the individual values of τ_i and τ_0. While τ_i differs in different plots, the same stress relaxation is observed when τ_i/τ_0 is the same.

rived by Eq. (3.12) from the indentation test with those obtained from the 1D uniaxial compression test. We used the method described in Section 2.1 to obtain the QLV parameters from uniaxial compression. The indentation and compression tests were done on three different elastomers and the parameters are compared in Table 3.2. Elastomers were made using commercially available elastomer kits Ecoflex™ 00-10, Ecoflex™ 00-30, and Ecoflex™ 00-50 along with NOVOCS™ solvents (Smooth-On Inc., Pennsylvania, USA). The elastomers' fabrication and the experimental apparatus are similar to what is described before in Section 2.1. Each experiment was repeated three times and the mean values are reported with

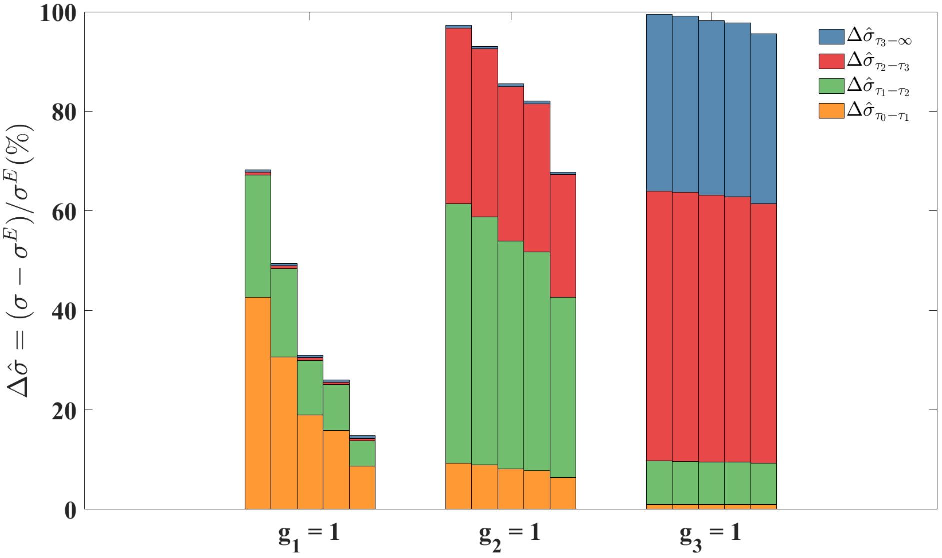

Figure 3.13: The stress relaxation of Fig. 3.12 in different time intervals; the data is nondimensionalized by elastic stress, and expressed as a percentage. The coefficient g_i affects the stress relaxation mainly between (τ_{i-1},τ_{i+1}); in particular, the stress relaxation over the last time interval is only influenced by g_3 since $\Delta\sigma_{\tau_3-\infty}$ is zero when $g_1=1$ or $g_2=1$. Likewise, stress relaxation in (τ_2,τ_3) depends on g_2 and g_3 ($\Delta\sigma_{\tau_2-\tau_3}$) is zero when $g_1=1$ and the stress relaxation between (τ_1,τ_2) depends on all three relaxation coefficients.

the standard deviation. Table 3.2 demonstrates a good precision (small standard deviation), though the accuracy is not appropriate for all cases; in particular, the derived values for g_1 from the indentation test are different from those obtained from the compression test. To improve the method's accuracy, we increased the number of points in Eq. (3.12) and minimize the difference E:

$$E=\sum_{\tau_i=\tau_0}^{\infty}\left(\Delta\hat{\sigma}_{\tau_i-\infty}-\sum_{k=1}^{3}g_k\left(\Delta\hat{\sigma}_{\tau_i-\infty}^{g_{k=1}}\right)\right)^2 \tag{3.13}$$

We used the 0.01s time steps in Eq. (3.13) and derived the materials' properties again (see Table 3.2). The results show a high precision (standard deviation less than 10%) and good accuracy (error within 20%) when compared to the parameters

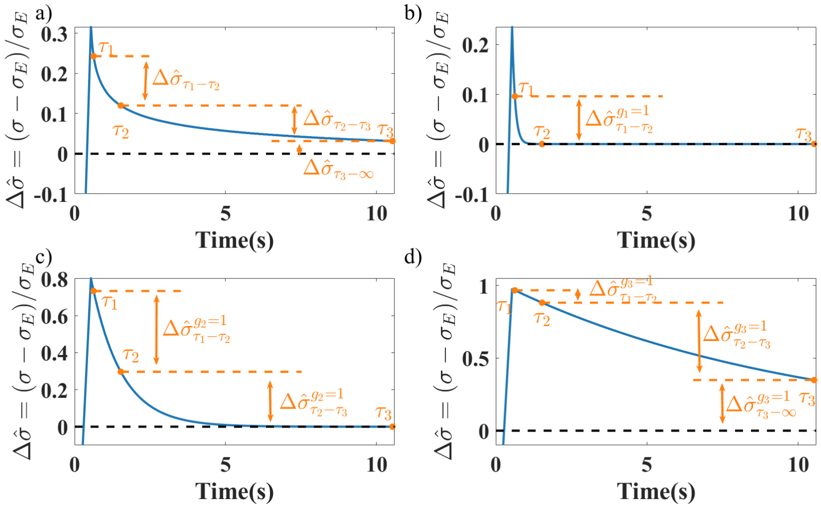

Figure 3.14: The suggested characterization procedure; a) stress relaxation from a ramp-and-hold indentation experiment. The figure shows stress relaxation created by b) $g_1 = 1$, c) $g_2 = 1$, and d) $g_3 = 1$. Note that the values for $\Delta\hat{\sigma}^{g_1=1}_{\tau_2-\tau_3}, \Delta\hat{\sigma}^{g_1=1}_{\tau_3-\infty}$, and $\Delta\hat{\sigma}^{g_2=1}_{\tau_3-\infty}$ are all zero. Eq. (3.12) compares the stress relaxation at three points ($t = \tau_1, t = \tau_2$, and $t = \tau_3$ in figure a) with those of pre-calculated simulation results (figures b-d) and derives the material's parameters. The results are depicted for indentation time $\tau_0 = 0.5$ s.

from the uniaxial test.

Eq. (3.13) derives the materials' parameters within a few seconds (~ 5 seconds), making it appropriate for real-time applications. Also, as mentioned earlier, the same method can be applied for indentation tests with different indenter diameters, indentation depths, and indentation tilt angles (misalignment) (see Figs. 3.9 and 3.16). Nevertheless, the accuracy of the results is compromised when the indenter size increases and the stress state approaches the uniaxial compression case ($\varphi \sim D$); in particular, the normalized stress relaxation for uniaxial compression (1D QLV model) is different from those shown in Fig. 3.12 by 40%. Our results do not suggest that the method should be used when the indenter is larger than half of the specimen diameter. Furthermore, the new characterization procedure is valid for materials that follow the QLV constitutive equations and the results are not necessarily true for materials whose elastic and viscous behavior cannot be separated. Finally, this chapter describes the viscous behavior by identifying the relaxation parameters, and it does not analyze other viscous aspects, like the loss modulus. The loss modulus describes the short-term viscoelastic behavior while our focus is on long-term viscoelastic response characterization. Studying the long-term viscoelastic behavior is more effective for detecting subtle microstructural changes in the material. Finally, the proposed method is more focused on viscous properties, and it is useful when the material can be characterized by viscous parameters. When elastic and viscous parameters are both needed for material characterization, inverse FE methods can be used, even with the longer processing time.

Table 3.2: Comparing the relaxation parameters obtained from uniaxial compression and indentation: the parameters are first obtained from the compression test using the method described in Section 2.1 and compared with those calculated from an indentation test using our proposed methods (Eqs. (3.12) and (3.13)). Compression and indentation tests were repeated three times for each material and the mean values are reported along with the standard deviations. The table demonstrates that Eq. (3.13) introduces parameters with a high precision (standard deviation within 10%) and in a good agreement with uniaxial parameters (maximum error within 20%).

Elastomer	**Uniaxial Compression (using the method in Section 2.1)**			**Indentation (Eq. (3.12))**			**Indentation (Eq. (3.13))**		
80% Ecoflex™ 00-10 + 20% NOVOCS™	0.57 ±0.01	0.16 ±0.00	0.09 ±0.00	0.63 ±0.00	0.13 ±0.00	0.09 ±0.00	0.51 ±0.01	0.13 ±0.00	0.11 ±0.00
Ecoflex™ 00-30	0.13 ±0.02	0.03 ±0.01	0.03 ±0.01	0.18 ±0.05	0.03 ±0.01	0.03 ±0.00	0.11 ±0.01	0.03 ±0.00	0.03 ±0.00
Ecoflex™ 00-50	0.15 ±0.01	0.05 ±0.00	0.04 ±0.00	0.25 ±0.03	0.05 ±0.01	0.04 ±0.00	0.18 ±0.00	0.05 ±0.00	0.04 ±0.00

3.4 Summary

In this chapter, we studied the viscoelastic behavior of a material under different indenter sizes and indentation depths, and revealed that the stress relaxation is dependent on neither. The stress relaxation was also investigated for different shear

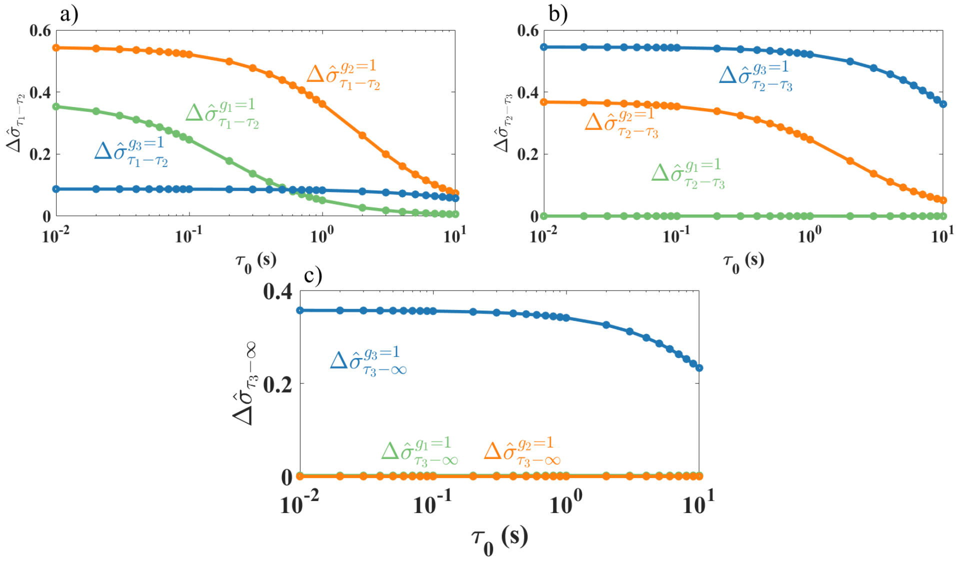

Figure 3.15: Effect of indentation rate (measured by τ_0) on the stress relaxations created by $g_1 = 1, g_2 = 1$, and $g_3 = 1$. The results demonstrate the stress relaxation between a) $(\tau_1 - \tau_2)$, b) $(\tau_2 - \tau_3)$, and c) $(\tau_3 - \infty)$. The stress relaxation decreases as the indentation time (τ_0) increases (slower indentation). No stress relaxation is created by g_1 after $t = \tau_2$ ($\Delta\hat{\sigma}_{\tau_2-\tau_3}^{g_1=1}$ and $\Delta\hat{\sigma}_{\tau_3-\infty}^{g_1=1}$) are zero in figures b and c) and no stress relaxation is made by g_2 after $t = \tau_3$ ($\Delta\hat{\sigma}_{\tau_3-\infty}^{g_2=1}$ is zero in figure c)). Since the values of $\Delta\hat{\sigma}^{g_1=1}, \Delta\hat{\sigma}^{g_2=1}$, and $\Delta\hat{\sigma}^{g_3=1}$ are dependent on the indentation rate, the values substituted in Eq. (3.12) and (3.13) should correspond to τ_0 used in the experiment.

relaxation moduli and it was shown that each relaxation modulus governs the stress relaxation in a specific time interval, so that the stress relaxation is proportionally related to the relaxation modulus. Based on these findings, we introduced a procedure for characterizing materials via indentation test and showed that our method can derive the material properties in a few seconds. Moreover, we compared the parameters derived with our method with those obtained from uniaxial compression test (Section 2.1) and demonstrated that our method has high accuracy (error within 20%) and precision (standard deviation within 10%). Having a method to characterize soft tissue, we are now ready to derive the viscoelastic properties of prostate tissue with and without cancer and study the effect of cancer on the prop-

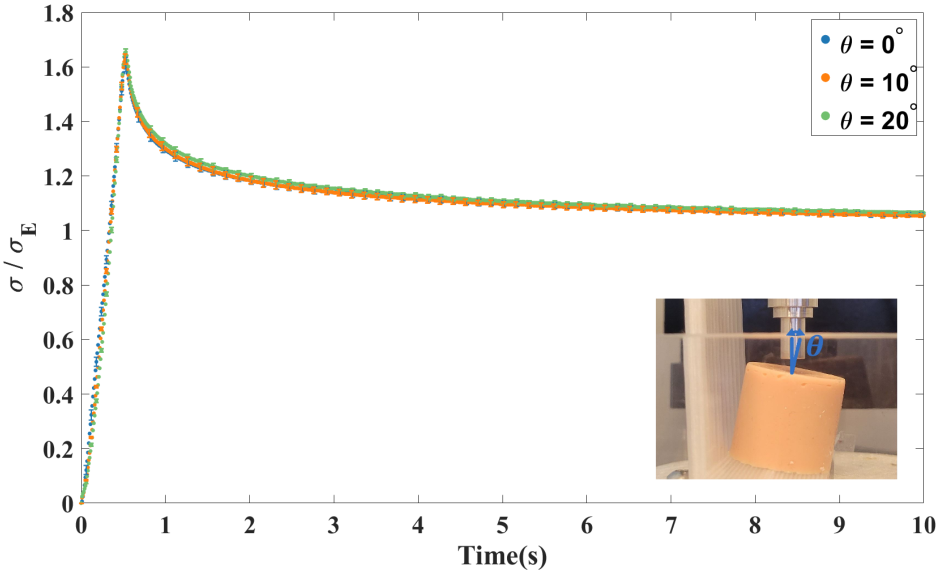

Figure 3.16: Normalized stress for indentation tests with different indentation tilt angles, defined as the angle between the indenter and contact surface normal (θ). The results demonstrate that tilt angle (misalignment) up to 20° does not affect the stress relaxation. Note that the figure represents the experimental data since the indentation test with 0 cannot be modelled with an axisymmetric simulation.

erties, which is the subject of next chapter.

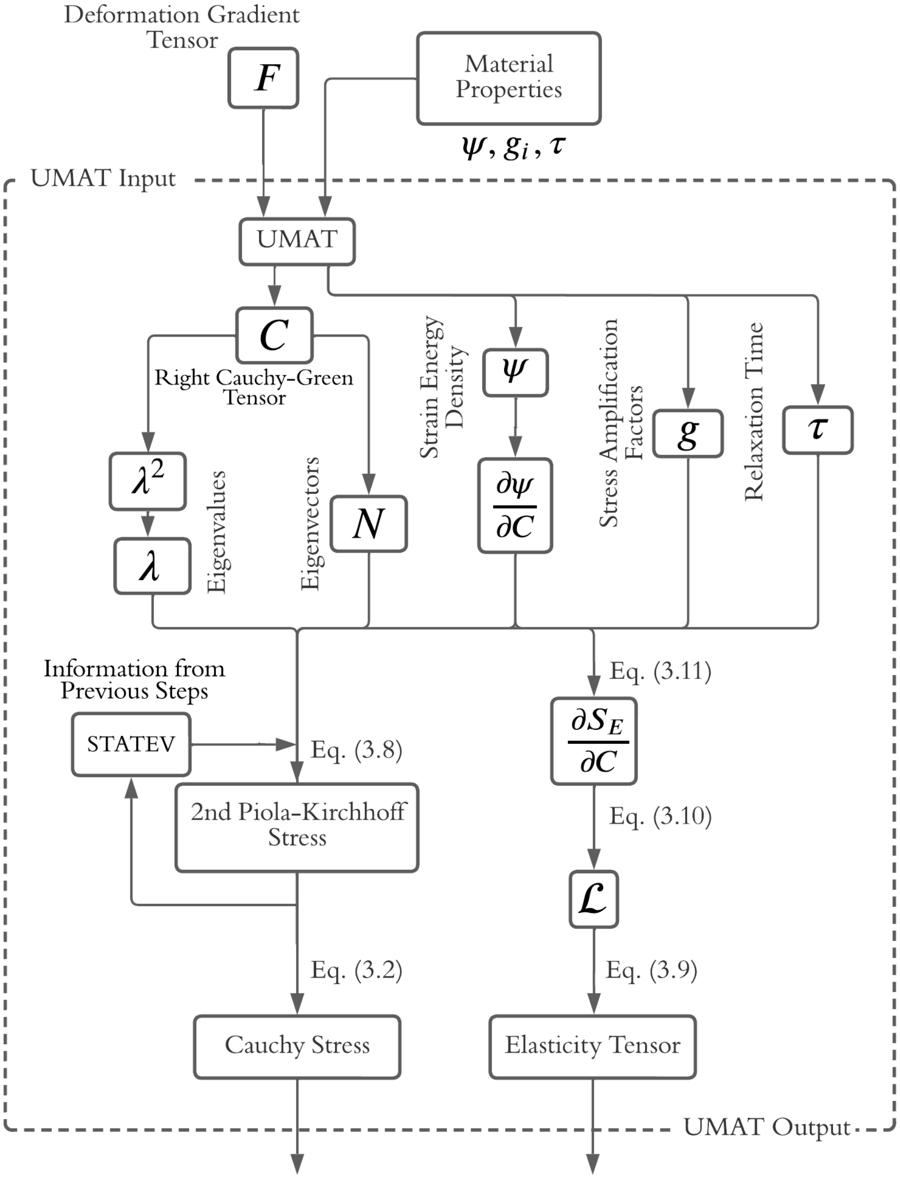
Deformation Gradient Tensor
F
Material Properties
ψ, g_i, τ
UMAT Input
UMAT
C
Right Cauchy-Green Tensor
Strain Energy Density
ψ
Stress Amplification Factors
g
Relaxation Time
τ
λ^2
λ
Eigenvalues
Eigenvectors
N
$\frac{\partial\psi}{\partial C}$
Information from Previous Steps
STATEV
Eq. (3.8)
2nd Piola-Kirchhoff Stress
Eq. (3.11)
$\frac{\partial S_E}{\partial C}$
Eq. (3.10)
$\mathcal{L}$
Eq. (3.2)
Eq. (3.9)
Cauchy Stress
Elasticity Tensor
UMAT Output

Figure 3.17: Algorithm for writing the UMAT software in Fortran; the UMAT receives the deformation gradient tensor (from ABAQUS calculations) and material properties (from user inputs) and provides the Cauchy stress and elasticity tensor.

Chapter 4

Effect of Cancer on the Viscoelastic Properties of Prostate Tissue

In this chapter, we aim to use the characterization method described in Chapters 2 and 3 for studying the effect of cancer on the stiffness and viscous properties of prostate tissue. Thirty-five fresh prostate samples were collected within two hours after their removal by radical prostatectomy surgery and characterized by the previously described process. We performed tests for four locations of the posterior prostate, and then transferred the samples to the pathology lab for histological analysis to reveal the presence or absence of cancer at each tissue site. The characterization results were then correlated with the pathology reports to study the effect of cancer on the viscoelastic properties of the prostate. Our results demonstrate that the presence of cancer has statistically meaningful effects on the stiffness and relaxation shear modulus of the prostate gland. In particular, we show that the first shear relaxation modulus and stiffness increase by 14% and 30%, respectively due to the presence of cancer.

This chapter is organized as follows: first, we provide a brief review on our characterization procedure and the design of a stress relaxation experiment for prostate tissue. We tested our method on prostate-mimicking phantoms with an embedded hard nodule representing a tumor. The phantoms were made using an anatomical model that represents the shape of the prostate. After validating the method, it was applied to real prostate tissues and the results are provided in the second section. The results include the effect of cancer and cancer grade on the mechanical properties of the prostate. We also performed statistical hypothesis testing on the data to reveal the significance of our conclusions. The application of the results for PCa diagnosis is discussed in the third section where we suggest a possible approach for *in vivo* detection of PCa. Finally, the conclusion of the chapter is provided in the fourth section.

4.1 Experimental Design for Ex Vivo Testing

As described in Chapter 3, material characterization was performed by feeding Cauchy stress data from a ramp-and-hold experiment into Eqs. (3.2), (3.3), and (2.8) and solving for σ_E and g_is. The stress relaxation experiment we used to characterize the prostate included a ramp-and-hold compression (Fig. 4.1a) where the sample was compressed at a rate of 10 mm/s from $t = 0$ to $t = \tau_0$ and kept at an indentation depth ($\delta = 5$ mm in the figure) for 45 seconds. Note that we increased the waiting period after the compression to 45 seconds to ensure that the stress had fully relaxed. Fig. 4.1b illustrates how the QLV parameters were derived from the relaxation stress response. Having σ_E and g_is, the viscoelastic properties of the soft tissues can be characterized.

4.1.1 Model Validation with Prostate-mimicking Phantoms

We validated the applicability of this procedure by testing it on tissue-mimicking phantoms. Phantoms (Figs. 4.2a and b) were made to represent the posterior prostate with a cancerous nodule on the left side (Prostate Model, 3B Scientific, Georgia, USA). Approximately 80% of the PCa has been shown clinically to stem from the posterior prostate [94]. After consulting with a pathologist expert, we considered three spherical nodules with diameters 5 mm, 7 mm, and 10 mm to demonstrate PCa in early, intermediate, and advanced stages, respectively. Each nodule was embedded near the surface (see Fig. 4.2). Previous prostate-mimicking phantom constructions for elastography studies used similar approaches [95, 96]. Phantoms were made using a commercial elastomer kit Ecoflex™ 00-10 (Smooth-

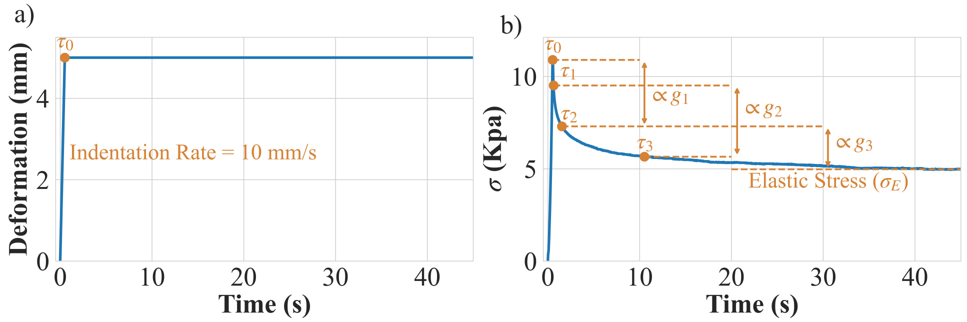

Figure 4.1: Procedure for mechanical testing: a) the sample is compressed at 10 mm/s and kept at an indentation depth (here, $\delta = 5$mm for 45 seconds), b) stress response after the compression shown in (a). Stress peaks occurred at $t = \tau_0$ and then they relaxed over time until reaching the steady-state stress σ_E. Relaxation shear moduli g_is were determined by the stress relaxation that occurred in different time periods, as specified by relaxation times τ_ks. Three relaxation times τ_1, τ_2, and τ_3 were chosen that were 0.1, 1, and 10 seconds, respectively, after $t = \tau_0$.

On Inc., Pennsylvania, USA), following the instructions given in Section 2.1. We tailored the mechanical properties by adding NOVOCS™ solvents (Smooth-On Inc., Pennsylvania, USA) so that the Young's modulus of our phantoms matched that of normal prostate tissue (15-20 kPa) [78]. The hard nodules were made with Ecoflex™ 00-50 (Smooth-On Inc., Pennsylvania, USA) with a Young's modulus similar to that of cancerous prostate tissue (40-60 kPa) [78]. As mentioned earlier, the viscous properties of the phantoms did not necessarily resemble normal and cancerous prostate since the viscous properties of prostate tissue have not been well established [79, 80]. To ensure that the phantoms had the same shape as the posterior prostate, we cured the polymer solution inside molds that had the same shape as our prostate anatomy model. The molds were fabricated using Mold Start™ 15 (Smooth-On Inc., Pennsylvania, USA).

The testing apparatus was similar to that described in Sections 2.1 and 3.1: the specimen was placed on a custom-built holder and an indenter with diameter of $\varphi = 7.60$ mm compressed the surface at $\delta = 5$ mm and then waited for 45 seconds for the stress to fully relax. Compression tests were repeated six times for each side and the σ_E and g_i were derived from each test. The values for σ_E and g_is were

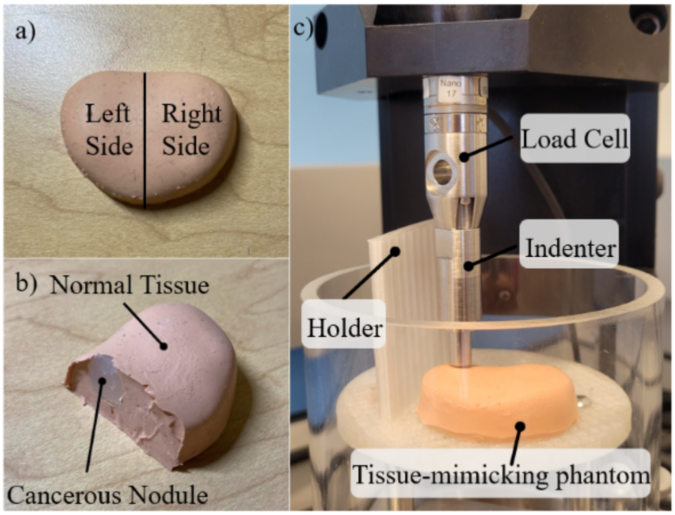

Figure 4.2: Tissue-mimicking phantoms with embedded nodules to resemble cancerous prostate tissue: a) phantoms were fabricated by Ecoflex™ 00-10 with elasticity close to the Young's modulus of normal prostate gland. The anatomical model was used to ensure that the phantom's shape was similar to that of the posterior prostate, b) a hard nodule was embedded on the left side of the phantom to mimic the presence of cancer. Nodules were made by Ecoflex™ 00-50 with a Young's modulus close to that of prostate cancer. Three phantoms were fabricated with different-sized nodules; i.e., 5 mm, 7 mm, and 10 mm, representing the presence of cancer in early, intermediate, and advanced stages, respectively, c) mechanical tester (Mach-1 V500CS) equipped with a multiple-axis load cell to record the stress response of tissue at a sampling rate of 100 Hz.

averaged and then reported in Figs. 4.3 and 4.4 to compare the properties of the "cancerous" side (the side with the nodule) to the "normal" side (the side without a nodule) under different nodule sizes. The relaxation shear moduli g_is for the nodules were four-times smaller than the substrate material, and hence, g_is at the cancerous side were expected to be smaller than those at the normal side (Fig. 4.3). Interestingly, the larger nodules were associated with more significant differences between the properties. Also, variations of g_1 were more significant than those of g_2 and g_3. Fig. 4.4 illustrates that the cancerous side had more stiffness than the normal side and the larger nodules led to more significant differences in elastic stress σ_E. Figs. 4.3 and 4.4 confirm our procedure's potential for detecting nodules inside the phantoms.

4.1.2 Experiment with Fresh Prostate Tissue

After testing the tissue-mimicking phantoms, we used the same procedure to obtain the viscoelastic properties of fresh prostate tissue. Ethical and operational approval was obtained from the Research Ethics Board at the University of British Columbia (H19-03592) and the Vancouver Coastal Health Authority. Thirty-five prostate glands were collected within two hours of their removal by radical prostatectomy surgery. Previously, it has been shown that the mechanical properties of excised prostate gland do not change within two hours after removal [97]. We excluded any cases that had received prior therapy, including radiation, high intensity focused ultrasound (HIFU), and androgen deprivation therapy (ADT) due to possible effects to the prostate properties. The prostatectomy surgeries were performed at Vancouver General Hospital (Vancouver, British Columbia, Canada) and the prostate samples were delivered to the pathology laboratory immediately after their removal. After being registered at the pathology laboratory, the fresh, unfixed samples were transported to a nearby facility with biosafety level 2 for the mechanical testing. Tissues were kept on ice during the transportation for 10 minutes. It has been shown that short-term contact with ice does not adversely affect the mechanical properties of biological tissues [98]. The mechanical tests were performed by compressing the tissue at a rate of 10 mm/s and then waiting 45 seconds for the stress relaxation to occur. The indentation strain did not exceed 15% to ensure that the test did not damage the tissue [5].

The mechanical test was repeated eight times at each site on the prostate (i.e., mid, apex, and at the left and right sides) (see Fig. 4.5). The first two tests were considered as tissue preconditioning (see Section 1.1) and the remaining six tests were used for the analysis. Before each test was begun, sites on the prostate were identified with help from an expert. Mechanical testing took approximately one hour, while the prostate was kept in a container filled with phosphate-buffered saline (PBS) to avoid dehydration. Samples were placed onto a custom-built plastic holder, so that the posterior prostate was at the top (in contact with the indenter),

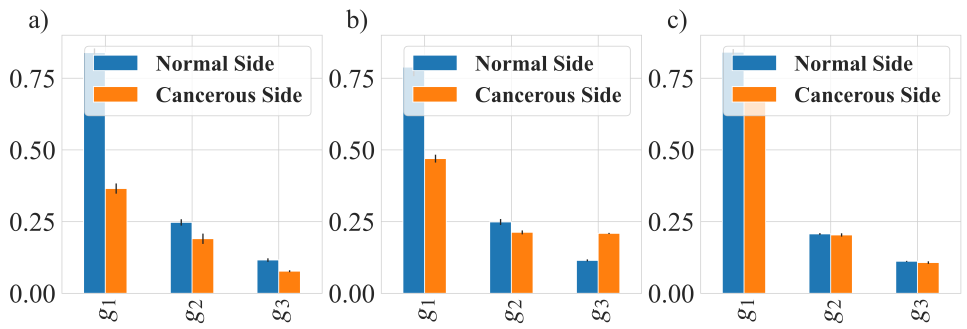

Figure 4.3: Model validation with tissue-mimicking phantoms: comparison of relaxation shear moduli between the side with the hard nodule (i.e., the "cancerous" side) and the side without a nodule (i.e., the "normal" side), for nodule sizes of a) 10 mm, b) 7 mm, and c) 5 mm. The figure shows that larger nodules led to higher viscous properties.

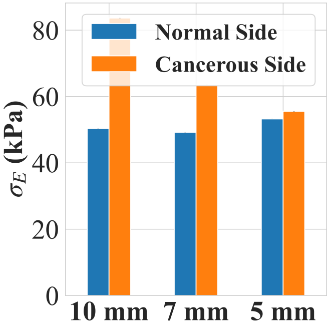

Figure 4.4: Model validation with tissue-mimicking phantoms: comparison of elastic properties (steady-state stress) between the side with the hard nodule (i.e., the "cancerous" side), and the side without a hard nodule (i.e., the "normal" side), for nodule sizes of 10 mm, 7 mm, and 5 mm. The figure shows that larger nodules led to higher elastic properties.

and the anterior prostate was at the bottom (in contact with the holder) (shown in Fig. 4.6). We performed the tests on the posterior side of the prostate to mimic the DRE procedure. The stress response of the prostate after compression was recorded, and the procedures described in Chapter 3 were followed to calculate σ_E and g_is for each tissue site. After testing, the samples were brought back to the pathology laboratory for histological examination. The histological analysis re-

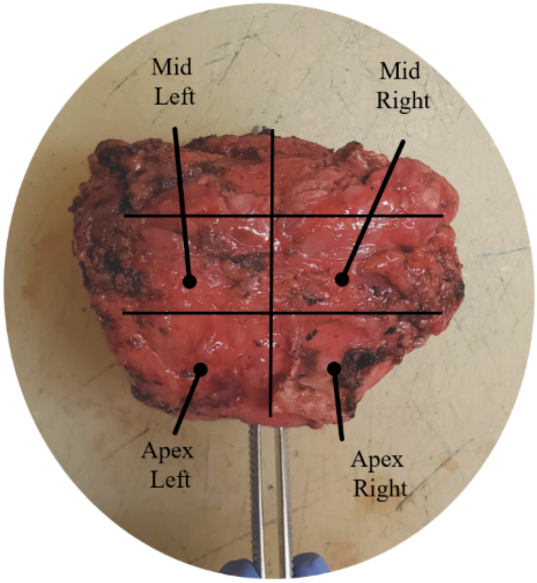

Figure 4.5: Fresh prostate gland: tissues were collected within two hours after being removed by radical prostatectomy surgery. Tests were performed on mid and apex sections of the posterior prostate and the mechanical properties were compared to those at the left and right sides of the posterior prostate.

ported: i) the location(s) of predominant tumor(s), ii) the cancer grade and Gleason score, iii) prostate volume, iv) tumor volume, v) prostate mass, and vi) the patient's age (Table B). Features that were not available for the report are left empty in the table. Prostate samples P1-P3 were used to verify the applicability of the QLV model for prostate tissue (Section 4.2.1) and samples P4-P35 were used to study the effect of cancer on prostate properties (Sections 4.2.2 and 4.2.3).

4.2 Results and Discussion

4.2.1 Application of the QLV model to Prostate Tissue

According to Eq. (3.3), the QLV model assumes that the elastic and viscous parts of a material's behavior are separable, which may not necessarily be true for all soft

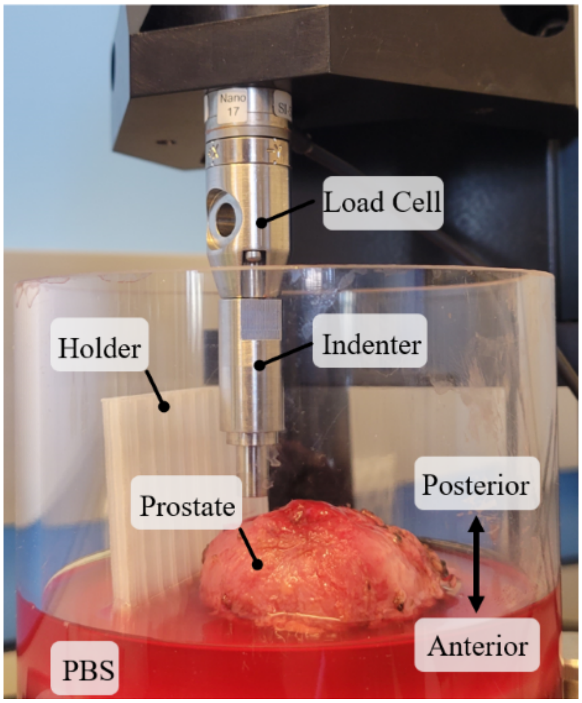

Figure 4.6: The prostate was placed into a container filled with phosphate buffered saline (PBS) to avoid dehydration. Samples were supported from beneath by a plastic holder and oriented so that the anterior prostate was at the bottom (touching the holder) and the posterior prostate was at the top (touching the indenter).

tissues [93]. To verify this assumption for prostate tissue, we changed the elastic component of the stress by performing the indentation test at different indentation depths and examined if the viscous behavior remained the same. Fig. 4.7 shows the viscous behavior of the prostate gland (P1, mid-section) under different indentation depths. We normalized the stress with σ_E to remove the effect of elastic stress. The normalized stress showed similar behaviors under different indentation depths (δ), which confirms that the elastic and viscous properties are separable in prostate tissue. We repeated the same procedure for the P2 and P3 sections, which led to the same conclusion. For further analysis, we derived the g_is for experiments with different indentation depths and compared the results (Fig. 4.8). The figure includes the results for the P1-P3 samples, and shows the variation of g_is with respect to indentation depth δ. The results are normalized with g_i^{avg}, which is the average g_i obtained from different indentation depths. The figure shows that g_2 (Fig. 4.8b) and g_3 (Fig. 4.8c) have smaller *between variation* than g_1 (Fig. 4.8a), which may be due to the undesirable effect of overshoot on g_1. Overshoot occurs when the tester cannot precisely control the indentation depth at a high rate, which may compromise the measurement accuracy for peak stress. This may also account for the larger error bars seen in Fig. 4.7 for recording stress when it is close to $t = \tau_0$. Overshoot has been shown to cause up to 30% error in deriving the QLV values [71].

Fig. 4.8 also shows the model's precision by the variation within g_is. The test with $\delta = 6$ mm indicates a higher precision as it had the lowest variation within g_is (green boxes in Fig. 4.8). To ensure that the indentation strain remained below 15%, the test with $\delta = 5$ mm (orange boxes in Fig. 4.8) was performed and it also showed a variation within g_is that was below 10%. The same is true for the precision of σ_E (Fig. 4.9).

4.2.2 Effect of Cancer on Mechanical Properties of Prostate

The prostate gland is a complex tissue with different mechanical properties at different locations; that is to say, the properties of the mid and apical areas are not similar. In a normal prostate gland, each section has symmetrical properties on the left and right sides (see Fig. 4.5). Consequently. the properties on the left and right sides of each section can be compared to study the effect of cancer on the viscoelastic properties. Fig. 4.10 shows the effect of cancer on the prostate properties, including the mid and apical sites. In cases where the predominant tumors are in both sides (mid site in sample P11, apical site in sample P14, and mid site in sample P21) the tests were excluded since the information on tumor size was not available. The properties were normalized by dividing the properties for the cancerous side (the side with a predominant tumor) by the properties for the normal side. Figs. 4.10a-d show the viscoelastic properties when the cancer was present in the posterior prostate and Figs. 4.10e-h show the properties when the cancer was in the anterior prostate. In most cases, g_is and σ_E are greater for the cancerous sides, especially in the posterior prostate. This observation is consistent with pre-

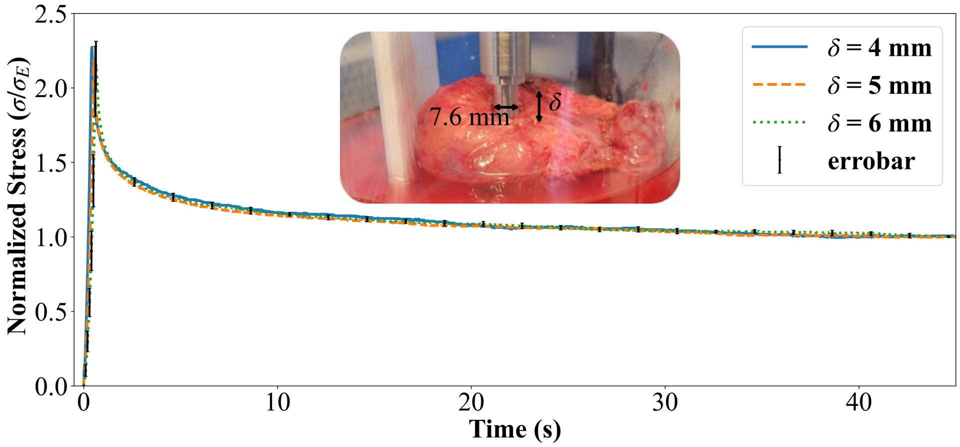

Figure 4.7: Applicability of the QLV model for prostate tissue: the QLV model's applicability for predicting the viscoelastic behavior of prostate tissue was checked by testing the separation between the viscous and elastic parts of the stress response. Testing was performed with different indentation depths; i.e., 4 mm, 5 mm, and 6 mm, and the stress was normalized by the elastic stress to obtain the viscous part of the stress. The results show that the elastic and viscous parts of the prostate stress response are separable since while the indentation depth varies, and hence the elastic part of stress, the viscous part remained the same.

vious studies that used MRE to derive the viscoelastic properties of prostate cancer [66, 68–70]. Figs. 4.10e-h show less significant differences, possibly because we measured the posterior prostate and so, the properties of the anterior prostate were less well captured. The 95% confidence intervals for the results in Fig. 4.10a-d are shown in Table 4.1.

The increase in g_is and σ_E due to cancer can be explained by changes in the tissue's cell structure. Tissue stress relaxation depends on the ability of cells to diffuse water (water diffusivity) and exchange their position with that of their neighbors (tissue fluidity). High water diffusivity and fluidity leads to smaller stress relaxation as the cells can rapidly relax the stress either by removing the water from the cells or rearranging their positions. PCa has been shown to decrease water diffusivity [66], which decreases the water movement between cells and hence increases the stress relaxation. This can explain why g_is increase in the presence of cancer.

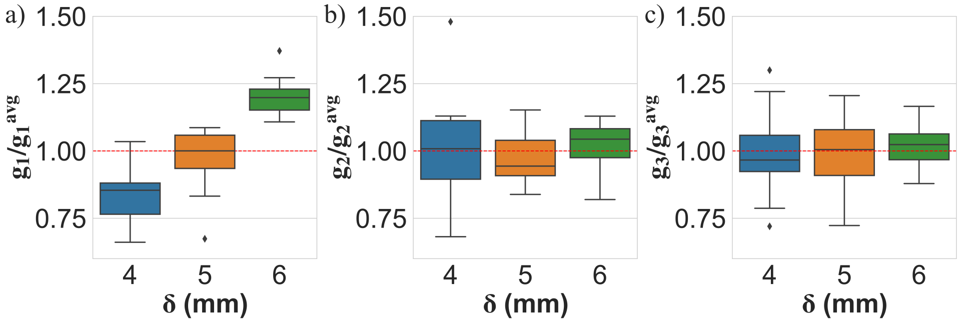

Figure 4.8: Applicability of the QLV model for the prostate gland: mechanical testing was performed with different indentation depths; i.e., $\delta = 4$ mm, 5 mm, and 6 mm, and the relaxation shear moduli g_is were obtained for each test. Each test was repeated eight times and the average and standard deviation of g_is for the last six tests were reported in the figure (blue, orange, and green boxes). The properties are normalized by g_i^{avg}s; i.e., the average of the properties for the three indentation depths. The figure shows that a) g_1, b) g_2, and c) g_3 from tests at different indentation depths are close. The greater variation of g_1 is mainly due to overshoot; i.e., when the tester cannot precisely control the final deformation at a high indentation rate. The figure also shows that the variation within g_is for the different tests is within 10%, which indicates the precision of the measurements.

The increase in elastic stress σ_E can also be explained by the uncontrolled proliferation of cancerous cells, so that the increased number of cells causes more stiffness. To further analyze the effect of cancer on the prostate properties, we performed a statistical analysis on the results. Table 4.2 shows the statistics for $g_i^{\text{cancer}}/g_i^{\text{normal}}$ and $\sigma_E^{\text{cancer}}/\sigma_E^{\text{normal}}$ in the posterior prostate (Fig. 4.10a-d). The table also includes the one-tailed p-values for the alternative hypotheses: $g_i^{\text{cancer}}/g_i^{\text{normal}} > 1$ and $\sigma_E^{\text{cancer}}/\sigma_E^{\text{normal}} > 1$ from a t-Student distribution. The effect of cancer is statistically significant for g_1 and σ_E with p-values less than 2%.

Table B shows that in some samples, both sides of a section were non-cancerous (like the mid-section in P4). In these samples, the properties at the left and right sides would be expected to be similar. Fig. 4.11 shows the properties for these cases, after the properties for the right side are normalized by the properties for the left side, without losing generality. The shaded area in the figure specifies the

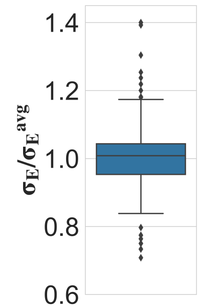

Figure 4.9: Precision of the QLV model: each mechanical test was repeated eight times and the results of last six tests were used for the figure. σ_E from each test was compared to the average elastic stress σ_E^{avg} to determine the precision of the measurements. From this figure (and Fig. 4.8) the QLV model has a high precision for reporting the viscoelastic properties of the prostate.

10% variation (as indicated in Section 3.1) that can be regarded as insignificant. The figure shows that some of the properties do not always fall within the 10% variation, especially in regards to g_3. While more data would be needed to confirm the observations, the different properties for the left and right sides can be explained by the presence of a tumor in a nearby section. Table 4.3 shows the 95% confidence interval (CI) for the results from Fig. 4.11, and both g_is and σ_E have acceptable confidence intervals. Moreover, while the results for g_2 and σ_E appear to be balanced around one, g_1 and g_3 appear to be slightly biased toward higher ratios. By comparing Tables 4.1 and 4.3, the properties of the prostate gland with and without the presence of cancer can be seen. In particular, the tables show that the presence of cancer increases g_1s and σ_E by 14%, and 30%, respectively.

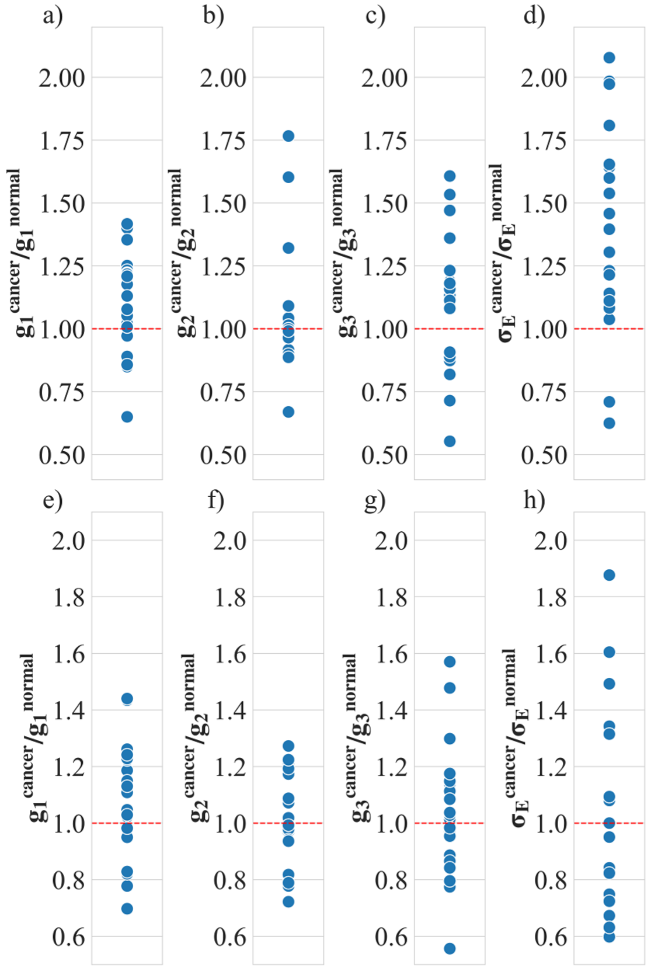

Figure 4.10: Effect of cancer on the mechanical properties when cancer is in posterior prostate (a-d); and when cancer is in anterior prostate (a-h). Samples that had cancer on both sides were excluded. The properties were normalized by dividing the properties of the cancerous side by the properties of the normal side for each section. Tests were repeated eight times for each quadrant and the average of the last six tests were used to calculate the properties. The figures show higher values for the properties on the cancerous side, especially for a) g_1, and d) σ_E as the ratio for the properties on the cancerous and normal sides are mostly above one. The effect of cancer on the properties is less significant when cancer occurred in the anterior prostate e-h), mainly because the tests were performed on the posterior prostate, which limits the accuracy in capturing the anterior prostate properties.

Table 4.1: 95% confidence intervals for the ratio between the properties of the cancerous and normal sides of the posterior prostate. As seen in Fig. 4.10, the properties for the cancerous side are greater than those for the normal side.

	Count	$\mathbf{g_1^{cancer}/g_1^{normal}}$	$\mathbf{g_2^{cancer}/g_2^{normal}}$	$\mathbf{g_3^{cancer}/g_3^{normal}}$	$\boldsymbol{\sigma_E^{cancer}/\sigma_E^{normal}}$
95% CI	46	(1.03 – 1.50)	(0.96 – 1.15)	(0.90 – 1.69)	(1.16 – 1.50)

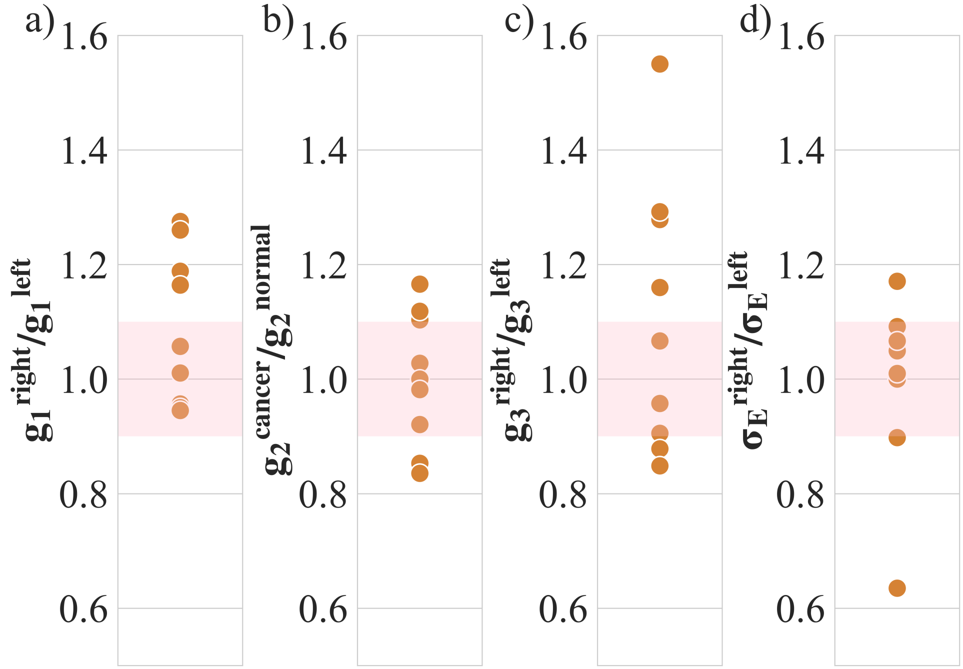

Figure 4.11: Mechanical properties of non-cancerous prostate gland. The properties are normalized by dividing the properties for the right side by the properties for the left side in each section. Since no cancerous nodules are in the prostate, the properties for the left and right sides are expected to be similar. The shaded area shows the 10% variation in the properties, which can be considered as insignificant (see Fig. 4.8 and Fig. 4.9). The figures also show more similarity between the properties for the left and right sides for a) g_1 and d) σ_E. The higher difference in g_2, c) g_3 may be explained by the presence of a nodule in a nearby section.

4.2.3 Effect of Cancer Grade on the Prostate Gland

In Section 3.2, the effect of cancer on the mechanical properties of the prostate was investigated. PCa is classified into different grades, depending on how fast it spreads and whether or not it affects other organs (metastatic cancer). Higher cancer grades are associated with fast-growing cancers that can invade nearby organs. In this section, we investigate the possible correlation between cancer grade and viscoelastic properties of the prostate. The relationships between cancer grade and other properties of the prostate are also discussed.

Fig. 4.12 illustrates the correlation between cancer grade, prostate volume, prostate mass, and patient's age. Fig. 4.12a shows that, as expected, the prostate mass and volume are highly correlated. Interestingly, our results show that the prostate volume (in mL) is close to the prostate mass (in grams). Nevertheless, these factors are not correlated with cancer grade and, for example, a cancer grade of five (red dots in Fig. 4.12a) can appear in small, intermediate, or large-sized prostate glands. Here, we reported the International Society of Urological Pathology (ISUP) Cancer Grade, calculated based on the Gleason patterns observed in the prostate (Table B). Cancer grade 2, shows that the top two patterns in the prostate are Gleason scores of 3 and 4 (shown as 3+4); Similarly, cancer grades 3,4, and 5 are associated with Gleason Score 4+3, 4+4, and 4+5 (or 5+4), respectively. Fig. 4.13 shows the patterns that correspond to Gleason scores of 3, 4, and 5, which represent cancerous cells in early, intermediate, and advanced stages, respectively. Since the cancer grade mostly depends on the cell patterns and not on the prostate size, a clear correlation between cancer grade and prostate mass/volume would not be expected.

The correlations between cancer grade, patient's age, and cancer volume are shown in Fig. 4.12b. Prostate gland enlargement is a common condition that occurs as men age and so a relationship between prostate volume and patient's age would be expected. Moreover, while no apparent correlation is observed between age and cancer grade, high-grade cancers (i.e., grades 4 and 5) are more likely to appear in older patients. Similarly, Alibhai et al. [99] reported a weak correlation between cancer grade and patient's age. The presence of high-grade cancer in older patients can be explained by a lower number of screening tests, which can lead to more

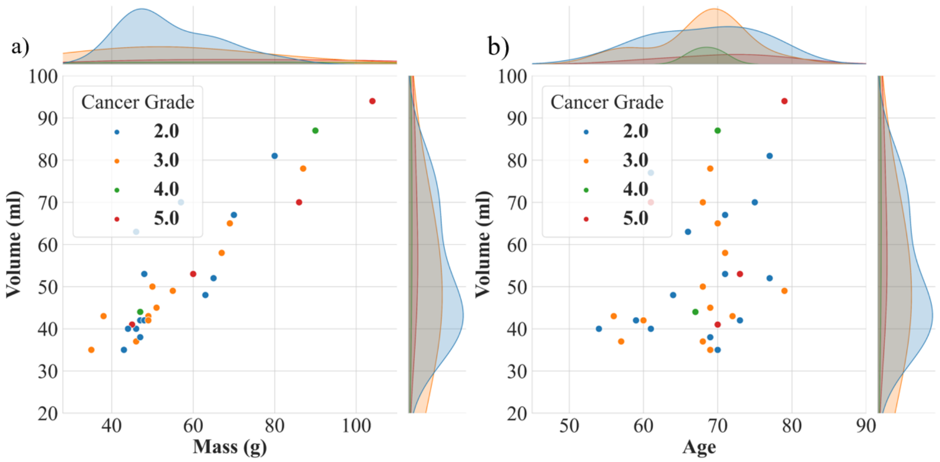

Figure 4.12: Correlation between different properties of the prostate gland: a) correlation between cancer grade, prostate mass, and prostate volume, and b) correlation between cancer grade, prostate volume, and patient's age. a) shows a strong correlation between the prostate volume and mass, but the cancer grade does not appear to be correlated to the mass or volume. For example, cancer grade 5 could be assigned to either a small or a large prostate gland. b) shows a positive correlation between patient's age and prostate volume. While a clear relationship between cancer grade and age is not seen, high-grade cancer (i.e., grades 4 and 5) are more likely to occur in older patients.

advanced PCa levels [99]. Changes in cancer biology can also explain the high grades of cancer in older patients [100].

Besides cancer grade, the tumor volume is another important factor that can be used to evaluate the cancer progression. Tumor volume is the total volume of the prostate that is occupied by a tumor nodule(s) and higher tumor volumes are associated with more progressive cancers. Figs. 4.14 and 4.15 show the effect of tumor volume on the mechanical properties of prostate when cancer presents in the posterior and anterior prostates. A higher variation in the viscoelastic properties (i.e., larger $g_i^{\text{cancer}}/g_i^{\text{normal}}$ and $\sigma_E^{\text{cancer}}/\sigma_E^{\text{normal}}$) would be expected with an increase in tumor volume. Fig. 4.14 shows that an increase in tumor volume in the posterior prostate increases the viscous properties (Figs. 4.14a-c) but does not affect the elastic properties (Figs. 4.14d). Among the viscous properties, g_1 and g_3 are cor-

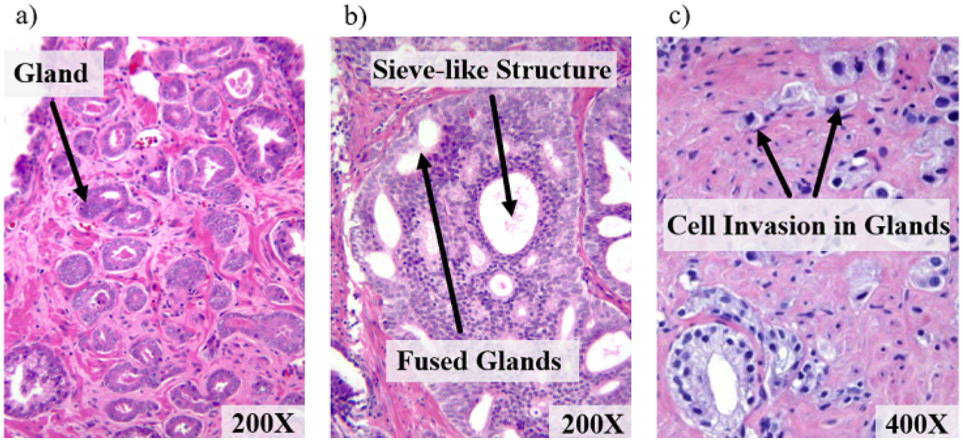

Figure 4.13: Gleason scores for prostate cancer cells: a) patterns for Gleason score 3 have well-formed glands without fusion, b) patterns for Gleason score 4 have back-to-back fused glands and a sieve-like structure formed by the cells, and c) patterns for Gleason score 5 show cell invasion in the glands.

related with the highest statistical significance (lowest p-values). That is to say, g_1 and g_3 can provide a good approximation of the tumor volume. As expected, less significant effects are observed when cancer is in the anterior prostate since the properties of the anterior prostate are not well captured by our testing. In addition, no correlation appears to exist between cancer grade and tumor volume. The same is also true for cancer grade and relative tumor volume (Fig. 4.16). The literature is generally controversial about whether or not tumor volume should be an indicator for PCa progression (e.g., [101, 102]). In 2007, Nature published work by May et al. [103] who concluded that relative tumor volume below 25% cannot serve as an independent factor for determining PCa progression. This would explain why we did not see an independent influence of tumor volume in most of our prostate samples, where the relative tumor volume was below 25% (Fig. 4.16). A larger sample of prostate glands with high tumor volumes would be needed to provide more insight into the relationship between tumor volume and PCa progression.

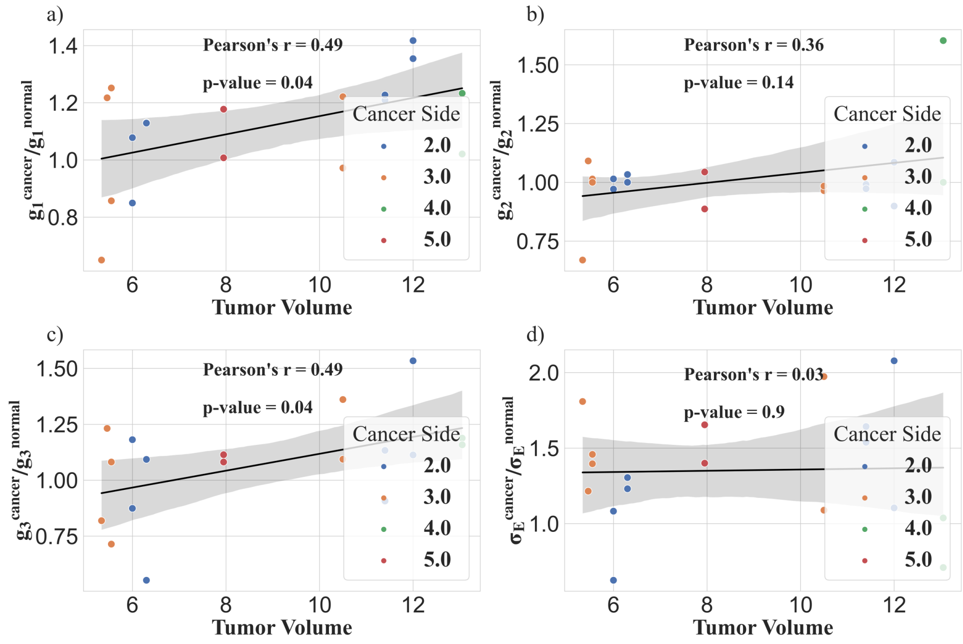

Figure 4.14: Correlation between tumor volume and properties when cancer presents in the posterior prostate. The properties were normalized by dividing the properties for the cancerous side to the properties for the normal side. Viscous properties are affected by tumor volume (see a, b, and c) while the elastic properties do not seem to vary with tumor volume (see d). g_1 and g_3 have the highest statistical significance (lowest p-value). The cancer grade does not appear to be correlated with tumor volume or the viscoelastic properties. International Society of Urological Pathology (ISUP) Cancer Grade was reported, and calculated based on the Gleason score. Cancer grades 2, 3, 4, and 5 are associated with Gleason Score 3+4, 4+3, 4+4, and 4+5 (or 5+4), respectively.

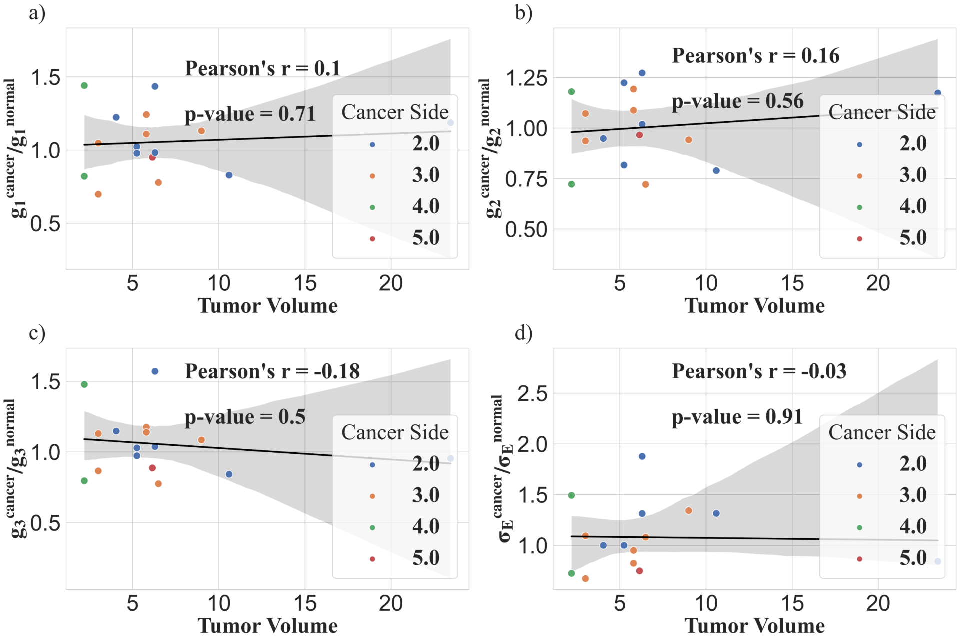

Figure 4.15: Correlation between tumor volume and mechanical properties when cancer presents in the anterior prostate. The properties are normalized by dividing the properties on the cancerous side by the properties on the normal side. Unlike Fig. 4.14, no clear correlation can be seen between tumor volume and the viscoelastic properties. This may be due to our testing that was performed on the posterior prostate, which fails to accurately capture the properties in the anterior prostate. International Society of Urological Pathology (ISUP) Cancer Grade was reported, and calculated based on the Gleason score. Cancer grades 2, 3, 4, and 5 are associated with Gleason Score 3+4, 4+3, 4+4, and 4+5 (or 5+4), respectively.

4.3 Application in Prostate Cancer Diagnosis

This thesis, which is focused on the possible effects of cancer on the properties of the prostate gland does not intend to introduce a diagnostic model for PCa. In fact, any diagnostic model for PCa would require a larger number of prostate samples ($\sim$ 50) for classification algorithms to be applied [104]. Nevertheless, the initial results of this study suggest that stiffness σ_E and the relaxation shear modulus g_1 could be used together to detect PCa with a high sensitivity (Table 4.2) and specificity

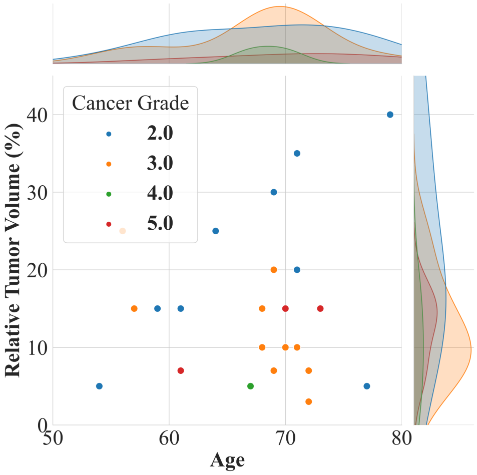

Figure 4.16: Correlation between cancer grade and relative tumor volume (tumor volume divided by prostate volume). No clear correlation is seen between cancer grade, patient's age, and the relative tumor volume. International Society of Urological Pathology (ISUP) Cancer Grade was reported, and calculated based on the Gleason score. Cancer grades 2, 3, 4, and 5 are associated with Gleason Score 3+4, 4+3, 4+4, and 4+5 (or 5+4), respectively.

Table 4.2: Descriptive and inferential statistics for the cancer effect on the viscoelastic properties of the prostate gland when cancer presents in the posterior prostate. The table also includes p-values for the alternative hypothesis with $g_i^{\text{cancer}}/g_i^{\text{normal}} > 1$ and $\sigma_E^{\text{cancer}}/\sigma_E^{\text{normal}} > 1$. From the table, cancer appears to have a greater statistically significant effect on g_1 and σ_E (lower p-values).

	$\mathbf{g_1^{\text{cancer}}/g_1^{\text{normal}}}$	$\mathbf{g_2^{\text{cancer}}/g_2^{\text{normal}}}$	$\mathbf{g_3^{\text{cancer}}/g_3^{\text{normal}}}$	$\boldsymbol{\sigma}_\mathbf{E}^{\text{cancer}}/\boldsymbol{\sigma}_\mathbf{E}^{\text{normal}}$
Count	24	24	24	24
Average	1.24	1.06	1.29	1.33
Standard Deviation	0.49	0.22	0.94	0.40
p-values	0.012	0.12	0.07	0.00

Table 4.3: 95% confidence interval for non-cancerous prostate samples. Since cancer is absent from the prostate sections, the properties for the left and right sides are expected to be similar. The table shows that g1 and g3 are relatively biased towards higher ratios and g2 and E are balanced around a ratio of one.

	Count	$\mathbf{g_1^{right}/g_1^{left}}$	$\mathbf{g_2^{right}/g_2^{left}}$	$\mathbf{g_3^{right}/g_3^{left}}$	$\sigma_{\mathbf{E}}^{\mathbf{right}}/\sigma_{\mathbf{E}}^{\mathbf{left}}$
95% CI	9	(0.99 – 1.20)	(0.91 – 1.09)	(0.92 – 1.29)	(0.88 – 1.14)

(Table 4.3). σ_E has been widely used for detecting prostate cancer but to the best of our knowledge, this is the first time that the relaxation shear modulus is reported to serve as a possible diagnostic tool. We also report that the method can estimate tumor volume (Fig. 4.14). Nevertheless, our current results do not suggest that the method would be appropriate for detecting cancer in the anterior prostate, which accounts for approximately 20% of all PCa cases [94]. The same problem has also been reported for detecting PCa via ultrasound elastography [105] or by biopsy [94]. Furthermore, the current results are only valid for *ex vivo* examination and their applicability for *in vivo* tests remains for future studies. For instance, since *in vivo* examination involves the indenter approaching the prostate gland through the rectum, the effect of the rectal wall on force measurements should be analyzed. That is to say, possible clinical applications of this method *in vivo* would require other considerations that are beyond the scope of this study. A brief discuss on the possible approach for *in vivo* applications of our results for PCa diagnosis is included in the Appendix, though we leave the actual implementation to future work.

4.4 Summary

In this chapter, we derived the QLV properties for fresh prostate tissue and investigated the effect of cancer on the viscoelastic characteristics. Thirty-five prostate glands were collected within two hours following prostatectomy surgery and their QLV parameters were obtained by performing stress relaxation experiments. The properties were then correlated with the presence and grade of cancer to study the effect of cancer on the stiffness and shear relaxation moduli of the prostate.

The results show that cancer increases both elastic and viscous properties of the prostate with a high statistical significance (p-value $< 2\%$). For example, the first shear relaxation modulus and stiffness increase by 14% and 30%, respectively in the presence of cancer. In addition, the cancer grade is not directly related to the mechanical properties of the prostate or prostate volume and mass. Furthermore, tumor volume is highly correlated with the viscous properties, so that a higher tumor volume appears to lead to a higher shear relaxation moduli. No similar correlation was found for the elastic properties. In this chapter, the application of the results to the *in-vivo* diagnosis of PCa was also discussed. A FBG sensor was designed and fabricated for possible use as a diagnostic tool *in-vivo* and the sensor's applicability for detecting a hard nodule within prostate-mimicking phantoms was demonstrated.

Chapter 5

Conclusions and Future Work

5.1 Conclusion

The mechanical properties of biological soft tissues have attracted much attention due to their importance in diagnosing diseases. In particular, assessing the mechanical properties of the prostate gland is suggested to be a primary method for detecting prostate cancer. In this thesis, we presented a new method for calibrating the quasi-linear viscoelastic (QLV) model by using uniaxial stress relaxation experiments (Chapter 2) and extended the method for a possible indentation test (Chapter 3). Finally, we characterized the viscoelastic properties of the prostate gland and studied the effect of cancer and cancer grade on shear relaxation moduli and stiffness of prostate tissue (Chapter 4). In the following sections, we present concluding remarks for each chapter.

5.1.1 Calibrating the QLV Model via the Uniaxial Test

A new method for calibrating the QLV model was presented that derives the shear relaxation moduli and Young's modulus for soft materials using uniaxial compression tests. The method differs from previously reported methods that are based on the QLV model in two aspects: 1) we define elastic stress as the stress that emerges after a sufficiently long time, where the time-dependent part vanishes and only the elastic part remains; and 2) we designed two different experiments to calculate the elastic and viscous characteristics independently. Considering these two modifications, we derived the viscoelastic properties with confidence intervals that were one-third of those previous reported.

To ensure the applicability of our method, we tested it on tissue-mimicking phantoms; i.e., soft materials that represent the mechanical properties of biological tissue. For this purpose, we performed stress relaxation tests at specific compression depths and used the results to characterize the material. The derived parameters were then used to predict the behavior of materials at other compression depths, and the predicted results were in good agreement with the experimental results. Thus, the ability of the model to derive the properties independently from the loading conditions was demonstrated. These results represent an improvement with respect to other viscoelastic models (e.g., spring-dashpot models) that introduce different parameters for each loading condition. We tested the applicability of the method to distinguish prostate phantoms with the same Young's modulus as normal and cancerous prostate tissue, and the results allowed for the precise distinction between the materials. We also showed that our model can distinguish materials with similar elastic properties but different viscous properties, and vice-versa. On the limitation side however, we admit the fact that a better fit with experimental data could be presented by increasing the number of relaxation times, and hence the relaxation moduli, but at the risk of over-fitting. Another way to improve the modeling could be optimizing relaxation times instead of pre-selecting them, but this may further complicate the fitting algorithm.

5.1.2 QLV Characterization via the Indentation Test

Because the method for QLV calibration by a uniaxial compression test may not necessarily be applicable to *in vivo* testing, we presented a procedure for QLV characterization by an indentation test. For this purpose, we studied the indentation behavior of viscoelastic materials with an indentation test under different loading conditions. The effect of the QLV parameters on stress relaxation behavior was also discussed. The results show that stress relaxation is not dependent on the indenter size or indentation depth, and it is only governed by the material properties and the indentation rate. The shear relaxation moduli were also shown to affect the stress relaxation at specific time intervals and thus, they are proportional to the amount of stress relaxation. We also calculated the effect of different relaxation moduli on stress relaxation by superimposing the effect of each modulus. While demonstrating a good performance for characterizing soft materials, it should be noted that our model (and hence the reported parameters) is affected by the selected relaxation times. We argue that our selection was limited by experimental parameters (e.g. sensors/actuators specifications). In the future, one can derive a continuous spectrum of relaxation moduli by invoking Eq. (2.6) for the relaxation function and hence report a better description of the relaxation behaviour; however, it might be challenging to combine with FEA.

Based on the findings, we present a new procedure for fast and straightforward characterization of soft materials. Using a finite element analysis, we can calculate the stress relaxation for different time intervals and estimate the value for the relaxation moduli. To validate the accuracy of our procedure, we compared the parameters obtained from an indentation test with those calculated from the uniaxial compression tests (Chapter 2), where a good accuracy (error within 20%) and high precision (standard deviation within 10%) have been reported. Our procedure can also characterize materials within a few seconds, which distinguishes it from inverse finite element methods, making it appropriate for real-time material characterization. It is important to mention that the applicability of the calibration method for a more complex phantom was not discussed in the section as our phantoms were all homogeneous with a simple cylindrical shape. We acknowledge the possibility of less accurate performance for the model when it comes to more complex phantoms.

5.1.3 Effect of Cancer on Prostate Viscoelasticity

We used the models presented in Chapters 2 and 3 to characterize the mechanical properties of the prostate gland and study the effect of cancer on the properties. First, we used the model to detect a hard nodule within a prostate-mimicking phantom. The hard nodule and the phantom have the same Young's modulus as normal and cancerous prostate tissue, respectively. We performed stress relaxation tests on the sides with and without the hard nodule and compared the properties to determine whether or not the model can capture differences in the mechanical properties. The results confirm that the model can recognize different mechanical properties for the side with a small nodule (5 mm in diameter) compared to the side without a nodule.

For clinical assessments, we collected 35 fresh prostate glands within two hours of their removal and tested their viscoelastic properties. First, we validated the applicability of the QLV model for prostate tissue by checking whether or not the elastic and viscous aspects can be separated. We repeated the stress relaxation tests with different indentation depths (to change the elastic aspect) and found that the viscous part of stress relaxation remained the same. After validating the applicability of the QLV model for prostate tissue, we compared the properties of cancerous and non-cancerous prostate tissues to assess the effect of cancer and cancer grade on the relaxation moduli and stiffness. We found that cancer can change prostate gland properties with a high statistical significance (p-value $< 2\%$). Cancer increases the first relaxation modulus by 14% and the stiffness by 30%. The relationship between cancer grade and the prostate properties were also assessed though no apparent correlation was observed. Nevertheless, cancer grade was found to be correlated with the patient's age and high-grade cancers were more likely to occur among older patients. A similar trend was not observed for low-grade cancers. Furthermore, tumor volume was also shown to be highly correlated with relaxation moduli though the same was not true for the elastic properties.

5.2 Future Work

The clinical applications of the findings for detecting prostate cancer would require the following future work:

1. The QLV model in Chapters 2 and 3 are derived for a homogeneous and isotropic material, which is not the case for complex biological tissues, like prostate gland. While the current model seems to provide accurate results, the accuracy can be improved by considering anisotropic relaxation function in the QLV model to reflect the complex composition of the tissue. This step would be required if future results show that the model's accuracy diminishes by including more data.

2. More prostate samples should be tested *ex vivo* and analyzed with classification algorithms to obtain a model predicting the presence and grade of prostate cancer based on the mechanical properties. For this purpose, the important features in detecting prostate cancer should be specified and then importance of each is determined by employing ensemble classification algorithms.

3. *In vivo* testing should be performed to confirm if the conclusion from *ex vivo* testing is also valid for *in vivo* setting. The testing can be first performed on a life-like prostate examination simulator and then on human participants. For this purpose, a mechanism should be designed to navigate the sensor (described in the Appendix) through the rectum so that it smoothly accesses the prostate gland and stays fixed during the force measurement. *In vivo* testing can investigate whether or not the rectum wall affects the force readings. It can also show if the prostate position variation from a person to another can make difference in the results. That being said, it should be mentioned that the current results cannot be extended to *in vivo* setting. For example, the guidance of the sensor through the rectum needs to be considered before any *in vivo* experiments. Appropriate guidance should ensure the sensor can reach the prostate quadrants, so the indentation test is performed the same as *ex vivo*. Also, *in vivo* applications might require using a smaller indenter than what we used in this work, which may alter the results. Last but not least, it should be mentioned that the sample we used is biased toward the people with confirmed prostate cancer, which is different from our actual sample, i.e., all people who are suspicious of having prostate cancer. While we can address this issue by doing *in vivo* testing on a more diverse sample, the difference in the sample sizes might lead to different outcomes.

4. Finally, the results of *in vivo* testing should be compared with those obtained from digital rectal examination by practicing both on the same participants. The comparison can demonstrate how much the method is effective in improving the prostate cancer diagnosis.

Bibliography

[1] Yuan-Cheng Fung. *Biomechanics*. Springer New York, New York, NY, 1981. → pages xiii, 4, 5, 6, 7, 8, 13, 16, 17

[2] Nihat Özkaya, Margareta Nordin, David Goldsheyder, and Dawn Leger. *Fundamentals of Biomechanics*, volume 86. Springer New York, New York, NY, mar 2012. → pages xiii, 7, 8

[3] Hyuna Sung, Jacques Ferlay, Rebecca L. Siegel, Mathieu Laversanne, Isabelle Soerjomataram, Ahmedin Jemal, and Freddie Bray. Global Cancer Statistics 2020: GLOBOCAN Estimates of Incidence and Mortality Worldwide for 36 Cancers in 185 Countries. *CA: A Cancer Journal for Clinicians*, 71(3):209–249, 2021. → page 1

[4] Jan F. M. Verbeek and Monique J. Roobol. What is an acceptable false negative rate in the detection of prostate cancer? *Translational Andrology and Urology*, 7(1):54–60, 2018. → page 1

[5] Federico Campisano, Selim Ozel, Anand Ramakrishnan, Anany Dwivedi, Nikolaos Gkotsis, Cagdas D. Onal, and Pietro Valdastri. Towards a soft robotic skin for autonomous tissue palpation. In *2017 IEEE International Conference on Robotics and Automation (ICRA)*, pages 6150–6155. IEEE, may 2017. → pages 1, 60

[6] Leen Naji, Harkanwal Randhawa, Zahra Sohani, Brittany Dennis, Deanna Lautenbach, Owen Kavanagh, Monica Bawor, Laura Banfield, and Jason Profetto. Digital rectal examination for prostate cancer screening in primary care: A systematic review and meta-analysis. *Annals of Family Medicine*, 16(2):149–154, 2018. → page 1

[7] Timo F.W. Soeterik, Harm H.E. van Melick, Lea M. Dijksman, Douwe H. Biesma, J. Alfred Witjes, and Jean Paul A. van Basten. Multiparametric Magnetic Resonance Imaging Should Be Preferred Over Digital Rectal

Examination for Prostate Cancer Local Staging and Disease Risk Classification. *Urology*, 147:205–212, 2021. → page 1

[8] Daniel Jones, Charlotte Friend, Andreas Dreher, Victoria Allgar, and Una Macleod. The diagnostic test accuracy of rectal examination for prostate cancer diagnosis in symptomatic patients: A systematic review. *BMC Family Practice*, 19(1):1–6, 2018. → page 1

[9] Rosa M.S. Sigrist, Joy Liau, Ahmed El Kaffas, Maria Cristina Chammas, and Juergen K. Willmann. Ultrasound elastography: Review of techniques and clinical applications. *Theranostics*, 7(5):1303–1329, 2017. → pages 1, 3

[10] Yogesh K. Mariappan, Kevin J. Glaser, and Richard L. Ehman. Magnetic resonance elastography: A review. *Clinical Anatomy*, 23(5):497–511, 2010. → page 1

[11] J. L. Gennisson, T. Deffieux, M. Fink, and M. Tanter. Ultrasound elastography: Principles and techniques. *Diagnostic and Interventional Imaging*, 94(5):487–495, 2013. → pages 1, 2, 3

[12] Árpád Takács, Imre J. Rudas, and Tamás Haidegger. Surface deformation and reaction force estimation of liver tissue based on a novel nonlinear mass–spring–damper viscoelastic model. *Medical Biological Engineering Computing*, 54(10):1553–1562, 2016. → pages 2, 7, 29

[13] T H J Yang, S Phipps, S K W Leung, R L Reuben, F K Habib, S A McNeill, and R W Else. Dynamic instrumented palpation (DIP)—a new method for soft tissue quality assessment; application to engineered mechanical phantom materials. *Biomedical Physics Engineering Express*, 3(2), mar 2017. → page 2

[14] Z. T H Tse, H. Janssen, A. Hamed, M. Ristic, I. Young, and M. Lamperth. Magnetic resonance elastography hardware design: A survey. *Proceedings of the Institution of Mechanical Engineers, Part H: Journal of Engineering in Medicine*, 223(4):497–514, 2009. → page 2

[15] Jeffrey M. Abeysekera, Manyou Ma, Mehran Pesteie, Jefferson Terry, Denise Pugash, Jennifer A. Hutcheon, Chantal Mayer, Lutz Lampe, Septimiu Salcudean, and Robert Rohling. SWAVE Imaging of Placental Elasticity and Viscosity: Proof of Concept. *Ultrasound in Medicine and Biology*, 43(6):1112–1124, 2017. → pages 2, 12

[16] Kathryn R. Nightingale, Mark L. Palmeri, Roger W. Nightingale, and Gregg E. Trahey. On the feasibility of remote palpation using acoustic radiation force. *The Journal of the Acoustical Society of America*, 110(1):625–634, 2001. → page 2

[17] Costanza Bruno, Salvatore Minniti, Alessandra Bucci, and Roberto Pozzi Mucelli. Arfi: from basic principles to clinical applications in diffuse chronic disease—a review. *Insights into imaging*, 7(5):735–746, 2016. → page 2

[18] Kathy Nightingale. Acoustic radiation force impulse (arfi) imaging: a review. *Current medical imaging*, 7(4):328–339, 2011. → page 2

[19] Behzad Babaei, Aaron J Velasquez-Mao, Stavros Thomopoulos, Elliot L Elson, Steven D Abramowitch, and Guy M Genin. Discrete quasi-linear viscoelastic damping analysis of connective tissues, and the biomechanics of stretching. *Journal of the mechanical behavior of biomedical materials*, 69:193–202, 2017. → page 2

[20] MS Commisso, JL Calvo-Gallego, J Mayo, E Tanaka, and J Martínez-Reina. Quasi-linear viscoelastic model of the articular disc of the temporomandibular joint. *Experimental Mechanics*, 56(7):1169–1177, 2016.

[21] Jose L Calvo-Gallego, Jaime Domínguez, Tomás Gómez Cía, Gorka Gómez Ciriza, and Javier Martínez-Reina. Comparison of different constitutive models to characterize the viscoelastic properties of human abdominal adipose tissue. a pilot study. *Journal of the mechanical behavior of biomedical materials*, 80:293–302, 2018. → page 2

[22] Xiaohui Guo, Ying Huang, Xia Cai, Caixia Liu, and Ping Liu. Capacitive wearable tactile sensor based on smart textile substrate with carbon black /silicone rubber composite dielectric. *Measurement Science and Technology*, 27(4), 2016. → page 3

[23] Anish S. Naidu, Rajni V. Patel, and Michael D. Naish. Low-Cost Disposable Tactile Sensors for Palpation in Minimally Invasive Surgery. *IEEE/ASME Transactions on Mechatronics*, 22(1):127–137, 2017. → page 3

[24] Zonglai Mo and Weiliang Xu. Temperature-Compensated Optical Fiber Force Sensing at the Tip of a Surgical Needle. *IEEE Sensors Journal*, 16(24):8936–8943, 2016. → pages 3, 4

[25] Tianliang Li, Chaoyang Shi, and Hongliang Ren. A High-Sensitivity Tactile Sensor Array Based on Fiber Bragg Grating Sensing for Tissue Palpation in Minimally Invasive Surgery. *IEEE/ASME Transactions on Mechatronics*, 23(5):2306–2315, 2018. → pages 3, 4

[26] S.J. Hammer, W.M. Shu, W.N. MacPherson, R.L. Reuben, J. Li, R.R.J. Maier, and D.P. Hand. An optical fibre dynamic instrumented palpation sensor for the characterisation of biological tissue. *Sensors and Actuators A: Physical*, 225:53–60, 2015. → page 3

[27] Daniele Tosi, Sven Poeggel, Iulian Iordachita, and Emiliano Schena. Fiber Optic Sensors for Biomedical Applications. In *Opto-Mechanical Fiber Optic Sensors*, pages 301–333. Elsevier, 2018. → page 4

[28] Paulo Roriz, Orlando Frazão, António B. Lobo-Ribeiro, José L Santos, and José A Simões. Review of fiber-optic pressure sensors for biomedical and biomechanical applications. *Journal of Biomedical Optics*, 18(5), may 2013. → page 4

[29] G. Chagnon, M. Rebouah, and D. Favier. Hyperelastic Energy Densities for Soft Biological Tissues: A Review. *Journal of Elasticity*, 120(2):129–160, 2015. → page 6

[30] Krit Chaimoon and Prinya Chindaprasirt. An anisotropic hyperelastic model with an application to soft tissues. *European Journal of Mechanics - A/Solids*, 78:103845, 2019. → page 6

[31] Alexander E Ehret and Mikhail Itskov. A polyconvex hyperelastic model for fiber-reinforced materials in application to soft tissues. *Journal of Materials Science*, 42(21):8853–8863, 2007.

[32] D.R. Nolan, A.L. Gower, M. Destrade, R.W. Ogden, and J.P. McGarry. A robust anisotropic hyperelastic formulation for the modelling of soft tissue. *Journal of the Mechanical Behavior of Biomedical Materials*, 39:48–60, 2014. → page 6

[33] Lawrence S Taylor, Amy L Lerner, Deborah J Rubens, and Kevin J Parker. A Kelvin-Voight fractional derivative model for viscoelastic characterization of liver tissue. *ASME 2002 International Mechanical Engineering Congress and Exposition*, pages 447–448, 2002. → pages 7, 29

[34] K J Parker, T Szabo, and S Holm. Towards a consensus on rheological models for elastography in soft tissues Towards a consensus on rheological models for elastography in soft tissues. 2019. → page 7

[35] R. De Pascalis, I. D. Abrahams, and W. J. Parnell. On nonlinear viscoelastic deformations: a reappraisal of Fung's quasi-linear viscoelastic model. *Proceedings of the Royal Society A: Mathematical, Physical and Engineering Sciences*, 470(2166), apr 2014. → pages 9, 32, 41

[36] Behzad Babaei, A.J. Velasquez-Mao, Kenneth M. Pryse, William B. McConnaughey, Elliot L. Elson, and Guy M. Genin. Energy dissipation in quasi-linear viscoelastic tissues, cells, and extracellular matrix. *Journal of the Mechanical Behavior of Biomedical Materials*, 84(May):198–207, 2018.

[37] Behzad Babaei, Steven D. Abramowitch, Elliot L. Elson, Stavros Thomopoulos, and Guy M. Genin. A discrete spectral analysis for determining quasi-linear viscoelastic properties of biological materials. *Journal of the Royal Society Interface*, 12(113):10–17, 2015. → pages 9, 17, 19

[38] M. A. Puso and J. A. Weiss. Finite element implementation of anisotropic quasi-linear viscoelasticity using a discrete spectrum approximation. *Journal of Biomechanical Engineering*, 120(1):62–70, 1998. → pages 9, 17

[39] W. Yang, T. C. Fung, K. S. Chian, and C. K. Chong. Viscoelasticity of esophageal tissue and application of a QLV model. *Journal of Biomechanical Engineering*, 128(6):909–916, 2006. → page 9

[40] Jose L. Calvo-Gallego, Jaime Domínguez, Tomás Gómez Cía, Gorka Gómez Ciriza, and Javier Martínez-Reina. Comparison of different constitutive models to characterize the viscoelastic properties of human abdominal adipose tissue. A pilot study. *Journal of the Mechanical Behavior of Biomedical Materials*, 80:293–302, apr 2018. → pages 9, 16, 19, 20

[41] Feng Xu, Keith Seffen, and Tianjian Lu. A Quasi-Linear Viscoelastic Model for Skin Tissue. *Proceedings of the 3rd IASME / WSEAS International Conference on CONTINUUM MECHANICS (CM'08)*, (July 2015):14–21, 2008. → page 9

[42] Kevin L. Troyer, Snehal S. Shetye, and Christian M. Puttlitz. Experimental Characterization and Finite Element Implementation of Soft Tissue

Nonlinear Viscoelasticity. *Journal of Biomechanical Engineering*, 134(11), nov 2012. → pages 9, 19

[43] Hang Yin Ling, Pong Chi Choi, Yong Ping Zheng, and Kin Tak Lau. Extraction of mechanical properties of foot plantar tissues using ultrasound indentation associated with genetic algorithm. *Journal of Materials Science: Materials in Medicine*, 18(8):1579–1586, 2007. → pages 10, 29

[44] Michelle Griffin, Yaami Premakumar, Alexander Seifalian, Peter Edward Butler, and Matthew Szarko. Biomechanical characterization of human soft tissues using indentation and tensile testing. *Journal of Visualized Experiments*, 2016(118):1–8, 2016. → pages 10, 29

[45] Golriz Kermani, Ali Hemmasizadeh, Soroush Assari, Michael Autieri, and Kurosh Darvish. Investigation of inhomogeneous and anisotropic material behavior of porcine thoracic aorta using nano-indentation tests. *Journal of the Mechanical Behavior of Biomedical Materials*, 69(July 2016):50–56, 2017. → page 10

[46] S Tripathy and E J Berger. Measuring Viscoelasticity of Soft Samples Using Atomic Force Microscopy. 131(September):6–11, 2009. → page 10

[47] Yuan-chiao Lu and Costin D Untaroiu. Effect of storage methods on indentation-based material properties of abdominal organs. (November), 2013. → page 10

[48] Long Qian and Hongwei Zhao. Nanoindentation of Soft Biological Materials. 2018. → page 10

[49] Suhao Qiu, Xuefeng Zhao, Jiayao Chen, Jianfeng Zeng, Shuangqing Chen, Lei Chen, and You Meng. Characterizing viscoelastic properties of breast cancer tissue in a mouse model using indentation. *Journal of Biomechanics*, 69:81–89, 2018. → page 10

[50] Y. P. Zheng and A. F.T. Mak. Extraction of quasi-linear viscoelastic parameters for lower limb soft tissues from manual indentation experiment. *Journal of Biomechanical Engineering*, 121(3):330–339, 1999. → page 10

[51] Yan-ping Huang and Yong-ping Zheng. Quasi-linear viscoelastic properties of fibrotic neck tissues obtained from ultrasound indentation tests in vivo. 20:145–154, 2005. → page 10

[52] R. K. Korhonen, M. S. Laasanen, J. Töyräs, J. Rieppo, J. Hirvonen, H. J. Helminen, and J. S. Jurvelin. Comparison of the equilibrium response of articular cartilage in unconfined compression, confined compression and indentation. *Journal of Biomechanics*, 35(7):903–909, 2002. → page 10

[53] Petro Julkunen, Rami K. Korhonen, Walter Herzog, and Jukka S. Jurvelin. Uncertainties in indentation testing of articular cartilage: A fibril-reinforced poroviscoelastic study. *Medical Engineering and Physics*, 30(4):506–515, 2008.

[54] R. M. Delaine-Smith, S. Burney, F. R. Balkwill, and M. M. Knight. Experimental validation of a flat punch indentation methodology calibrated against unconfined compression tests for determination of soft tissue biomechanics. *Journal of the Mechanical Behavior of Biomedical Materials*, 60:401–415, 2016. → pages 10, 41

[55] Behzad Seyfi, Nasser Fatouraee, and Milad Imeni. Mechanical modeling and characterization of meniscus tissue using flat punch indentation and inverse finite element method. *Journal of the Mechanical Behavior of Biomedical Materials*, 77(September 2017):337–346, 2018. → page 11

[56] Jung Kim and Mandayam A. Srinivasan. Characterization of Viscoelastic Soft Tissue Properties from In Vivo Animal Experiments and Inverse FE Parameter Estimation. pages 599–606. 2005. → page 11

[57] B. Pierrat, D. B. MacManus, J. G. Murphy, and M. D. Gilchrist. Indentation of heterogeneous soft tissue: Local constitutive parameter mapping using an inverse method and an automated rig. *Journal of the Mechanical Behavior of Biomedical Materials*, 78(March 2017):515–528, 2018. → page 11

[58] Katharina Boehm, Georg Salomon, Burkhard Beyer, Jonas Schiffmann, Kathrin Simonis, Markus Graefen, and Lars Budaeus. Shear wave elastography for localization of prostate cancer lesions and assessment of elasticity thresholds: Implications for targeted biopsies and active surveillance protocols. *Journal of Urology*, 193(3):794–800, 2015. → page 11

[59] Shuai Fu, Yuzhe Tang, Shi Tan, Yuqing Zhao, and Ligang Cui. Diagnostic value of transrectal shear wave elastography for prostate cancer detection in peripheral zone: comparison with magnetic resonance imaging. *Journal of endourology*, 34(5):558–566, 2020. → page 11

[60] Thineskrishna Anbarasan, Cheng Wei, Jeffrey C. Bamber, Richard G. Barr, and Ghulam Nabi. Characterisation of prostate lesions using transrectal shear wave elastography (SWE) ultrasound imaging: A systematic review. *Cancers*, 13(1):1–15, 2021. → page 12

[61] Guillermo Rus, Inas H. Faris, Jorge Torres, Antonio Callejas, and Juan Melchor. Why are viscosity and nonlinearity bound to make an impact in clinical elastographic diagnosis? *Sensors (Switzerland)*, 20(8):1–35, 2020. → page 12

[62] Haoming Lin, Xinyu Zhang, Yuanyuan Shen, Yi Zheng, Yanrong Guo, Ying Zhu, Xianfen Diao, Tianfu Wang, Siping Chen, and Xin Chen. Model-dependent and model-independent approaches for evaluating hepatic fibrosis in rat liver using shearwave dispersion ultrasound vibrometry. *Medical Engineering and Physics*, 39:66–72, 2017. → page 12

[63] Viksit Kumar, Max Denis, Adriana Gregory, Mahdi Bayat, Mohammad Mehrmohammadi, Robert Fazzio, Mostafa Fatemi, and Azra Alizad. Viscoelastic parameters as discriminators of breast masses: Initial human study results. *PLoS ONE*, 13(10):1–15, 2018. → page 12

[64] F. G. Mitri, M. W. Urban, M. Fatemi, and J. F. Greenleaf. Shear wave dispersion ultrasonic vibrometry for measuring prostate shear stiffness and viscosity: An in vitro pilot study. *IEEE Transactions on Biomedical Engineering*, 58(2):235–242, 2011. → page 12

[65] Bing Hu, Ying Deng, Jingbiao Chen, Sichi Kuang, Wenjie Tang, Bingjun He, Linqi Zhang, Yuanqiang Xiao, Jun Chen, Phillip Rossman, Arvin Arani, Ziying Yin, Kevin J Glaser, Meng Yin, Sudhakar K Venkatesh, Richard L Ehman, and Jin Wang. Evaluation of MR elastography for prediction of lymph node metastasis in prostate cancer PCa Prostate cancer. *Abdominal Radiology*, 46(7):3387–3400, 2021. → page 12

[66] Patrick Asbach, Sa-ra Ro, Nader Aldoj, Joachim Snellings, Rolf Reiter, Julian Lenk, Torsten Köhlitz, Matthias Haas, Jing Guo, Bernd Hamm, Jürgen Braun, and Ingolf Sack. In Vivo Quantification of Water Diffusion , Stiffness , and Tissue Fluidity in Benign Prostatic Hyperplasia and Prostate Cancer. 55(8), 2020. → pages 12, 65

[67] Kay M Pepin, Richard L Ehman, and Kiaran P Mcgee. Magnetic resonance elastography (MRE) in cancer : Technique , analysis , and applications. *PROGRESS IN NUCLEAR MAGNETIC RESONANCE SPECTROSCOPY*, 90-91:32–48, 2015. → page 12

[68] Saying Li, Min Chen, Wenchao Wang, Weifeng Zhao, Jianye Wang, and Xuna Zhao. A feasibility study of MR elastography in the diagnosis of prostate cancer at 3 . 0T. pages 0–4, 2011. → pages 12, 13, 65

[69] Rolf Reiter, Shreyan Majumdar, Steven Kearney, Virgilia Macias, Simone Crivellaro, Brandon Caldwell, Michael Abern, Thomas J Royston, and Dieter Klatt. Prostate cancer assessment using MR elastography of fresh prostatectomy specimens at 9 . 4 T. (November 2019):396–404, 2020. → pages 12, 13

[70] Martin Reiss-zimmermann, Josephin Otto, Karl-titus Hoffmann, Michael Moche, Nikita Garnov, Thomas Kahn, and Harald Busse. Novel Technique for MR Elastography of the Prostate Using a Modified Standard Endorectal Coil as Actuator. 1485:1480–1485, 2013. → pages 12, 65

[71] Jonathan A. Gimbel, Joseph J. Sarver, and Louis J. Soslowsky. The effect of overshooting the target strain on estimating viscoelastic properties from stress relaxation experiments. *Journal of Biomechanical Engineering*, 126(6):844–848, 2004. → pages 13, 27, 64

[72] George Z. Voyiadjis and Aref Samadi-Dooki. Hyperelastic modeling of the human brain tissue: Effects of no-slip boundary condition and compressibility on the uniaxial deformation. *Journal of the Mechanical Behavior of Biomedical Materials*, 83(April):63–78, 2018. → page 16

[73] Behzad Babaei, Aaron J. Velasquez-Mao, Stavros Thomopoulos, Elliot L. Elson, Steven D. Abramowitch, and Guy M. Genin. Discrete quasi-linear viscoelastic damping analysis of connective tissues, and the biomechanics of stretching. *Journal of the Mechanical Behavior of Biomedical Materials*, 69:193–202, 2017. → page 19

[74] M. S. Commisso, J. L. Calvo-Gallego, J. Mayo, E. Tanaka, and J. Martínez-Reina. Quasi-Linear Viscoelastic Model of the Articular Disc of the Temporomandibular Joint. *Experimental Mechanics*, 56(7):1169–1177, 2016. → page 19

[75] Steven D. Abramowitch and Savio L.Y. Woo. An improved method to analyze the stress relaxation of ligaments following a finite ramp time based on the quasi-linear viscoelastic theory. *Journal of Biomechanical Engineering*, 126(1):92–97, 2004. → pages 20, 27

[76] Hande Y. Benson and David F. Shanno. Interior-point methods for nonconvex nonlinear programming: Regularization and warmstarts.

Computational Optimization and Applications, 40(2):143–189, 2008. → page 20

[77] Piotr Mazurek, Sindhu Vudayagiri, and Anne Ladegaard Skov. How to tailor flexible silicone elastomers with mechanical integrity: A tutorial review. *Chemical Society Reviews*, 48(6):1448–1464, 2019. → pages 22, 26, 27

[78] Niall P. Kelly, Hugh D. Flood, David A. Hoey, Patrick A. Kiely, Subhasis K. Giri, J. Calvin Coffey, and Michael T. Walsh. Direct mechanical characterization of prostate tissue—a systematic review. *Prostate*, 79(2):115–125, 2019. → pages 22, 58

[79] Kenneth Hoyt, Benjamin Castaneda, Man Zhang, Priya Nigwekar, P. Anthony di Sant'Agnese, Jean V. Joseph, John Strang, Deborah J. Rubens, and Kevin J. Parker. Tissue elasticity properties as biomarkers for prostate cancer. *Cancer Biomarkers*, 4(4-5):213–225, nov 2008. → pages 22, 58

[80] Daniel W. Good, Grant D. Stewart, Steven Hammer, Paul Scanlan, Wenmiao Shu, Simon Phipps, Robert Reuben, and Alan S. McNeill. Elasticity as a biomarker for prostate cancer: A systematic review. *BJU International*, 113(4):523–534, 2014. → pages 22, 58

[81] Man Zhang, Priya Nigwekar, Benjamin Castaneda, Kenneth Hoyt, Jean V. Joseph, Anthony di Sant'Agnese, Edward M. Messing, John G. Strang, Deborah J. Rubens, and Kevin J. Parker. Quantitative Characterization of Viscoelastic Properties of Human Prostate Correlated with Histology. *Ultrasound in Medicine and Biology*, 34(7):1033–1042, 2008. → page 22

[82] Frank C.P. Yin, Paul H. Chew, and Scott L. Zeger. An approach to quantification of biaxial tissue stress-strain data. *Journal of Biomechanics*, 19(1):27–37, 1986. → pages 24, 25

[83] Xuejian Wang, Jianbo Wang, Yingxi Liu, Huafeng Zong, Xiangyu Che, Wei Zheng, Feng Chen, Zheng Zhu, Deyong Yang, and Xishuang Song. Alterations in mechanical properties are associated with prostate cancer progression. *Medical Oncology*, 31(3), 2014. → page 26

[84] Ville Jalkanen, Britt M. Andersson, Anders Bergh, Börje Ljungberg, and Olof A. Lindahl. Indentation loading response of a resonance sensor-discriminating prostate cancer and normal tissue. *Journal of Medical Engineering and Technology*, 37(7):416–423, 2013. → page 26

[85] E Verron MS Sukiman, D Wong, A Andriyana, BC Ang. Evaluation of the elastic properties of randomly-oriented electrospun nanofibrous polyurethane thermoplastic elastomer membranes. In *11th European Conference on Constitutive Models for Rubber (ECCMR 2019)*, pages 133–137, 2019. → page 28

[86] Marco Amabili, Prabakaran Balasubramanian, Ivan Breslavsky, Giovanni Ferrari, and Eleonora Tubaldi. Viscoelastic characterization of woven Dacron for aortic grafts by using direction-dependent quasi-linear viscoelasticity. *Journal of the Mechanical Behavior of Biomedical Materials*, 82(February):282–290, 2018. → pages 32, 44

[87] Stephen John Connolly, Donald Mackenzie, and Yevgen Gorash. Isotropic hyperelasticity in principal stretches: explicit elasticity tensors and numerical implementation. *Computational Mechanics*, 64(5):1273–1288, 2019. → pages 34, 35

[88] Nhung T Nguyen. *Experiments and Inverse Analysis for Determining Non-Linear Viscoelastic Properties of Polymeric Capsules and Biological Cells (Doctoral dissertation)*. PhD thesis, 2014. → page 34

[89] Juan C. Simo and Robert L. Taylor. Quasi-incompressible finite elasticity in principal stretches. continuum basis and numerical algorithms. *Computer Methods in Applied Mechanics and Engineering*, 85(3):273–310, 1991. → page 34

[90] J. C. Simo. On a fully three-dimensional finite-strain viscoelastic damage model: Formulation and computational aspects. *Computer Methods in Applied Mechanics and Engineering*, 60(2):153–173, 1987. → page 35

[91] L. Sanchez Fellay, L. A. Fasce, M. Czerner, E. Pardo, and P. M. Frontini. On the feasibility of identifying first order ogden constitutive parameters of gelatin gels from flat punch indentation tests. *Soft Materials*, 13(4):188–200, 2015. → page 39

[92] Alice Chinghsuan Chang and Bernard Haochih Liu. Modified flat-punch model for hyperelastic polymeric and biological materials in nanoindentation. *Mechanics of Materials*, 118(June 2017):17–21, 2018. → page 41

[93] Michelle L. Oyen. A model for nonlinear viscoelastic mechanical responses of collagenous soft tissues. *Materials Research Society Symposium Proceedings*, 898:66–71, 2005. → pages 42, 63

[94] S. R.J. Bott, M. P.A. Young, M. J. Kellett, and M. C. Parkinson. Anterior prostate cancer: Is it more difficult to diagnose? *BJU International*, 89(9):886–889, 2002. → pages 57, 76

[95] Gregory J. Gerling, Sarah Rigsbee, Reba Moyer Childress, and Marcus L. Martin. The design and evaluation of a computerized and physical simulator for training clinical prostate exams. *IEEE Transactions on Systems, Man, and Cybernetics Part A:Systems and Humans*, 39(2):388–403, 2009. → page 57

[96] Javier Palacio-Torralba, Robert L. Reuben, and Yuhang Chen. A novel palpation–based method for tumor nodule quantification in soft tissue—computational framework and experimental validation. *Medical and Biological Engineering and Computing*, 58(6):1369–1381, 2020. → page 57

[97] Ta a Krouskop, Tm M Wheeler, F Kallel, B S Garra, and T Hall. Elastic Moduli of Breast and Prostate Tissue under Compression. *Ultrasonic imaging*, 20(4):260–274, 1998. → page 60

[98] Chris M. Bleakley and Joseph T. Costello. Do thermal agents affect range of movement and mechanical properties in soft tissues? A systematic review. *Archives of Physical Medicine and Rehabilitation*, 94(1):149–163, 2013. → page 60

[99] Shabbir M.H. Alibhai, Murray D. Krahn, Neil E. Fleshner, Marsha M. Cohen, George A. Tomlinson, and Gary Naglie. The association between patient age and prostate cancer stage and grade at diagnosis. *BJU International*, 94(3):303–306, 2004. → pages 70, 71

[100] Deborah Borek, David Butcher, Khatab Hassanein, and Frederick Holmes. Relationship of age to histologic grade in prostate cancer. *The Prostate*, 16(4):305–311, 1990. → page 71

[101] Thomas A. Stamey, John E. McNeal, Cheryl M. Yemoto, Bronislava M. Sigal, and Iain M. Johnstone. patt. *Journal of the American Medical Association*, 281(15):1395–1400, 1999. → page 72

[102] M. L. Blute, O. Nativ, H. Zincke, G. M. Farrow, T. Therneau, and M. M. Lieber. Pattern of failure after radical retropubic prostatectomy for clinically and pathologically localized adenocarcinoma of the prostate: influence of tumor deoxyribonucleic acid ploidy. *Journal of Urology*, 142(5):1262–1265, 1989. → page 72

[103] M. May, M. Siegsmund, F. Hammermann, V. Loy, and S. Gunia. Visual estimation of the tumor volume in prostate cancer: A useful means for predicting biochemical-free survival after radical prostatectomy? *Prostate Cancer and Prostatic Diseases*, 10(1):66–71, 2007. → page 72

[104] F. Pedregosa, G. Varoquaux, A. Gramfort, V. Michel, B. Thirion, O. Grisel, M. Blondel, P. Prettenhofer, R. Weiss, V. Dubourg, J. Vanderplas, A. Passos, D. Cournapeau, M. Brucher, M. Perrot, and E. Duchesnay. Scikit-learn: Machine learning in Python. *Journal of Machine Learning Research*, 12:2825–2830, 2011. → page 74

[105] Review Article. Multiparametric ultrasound and micro- ultrasound in prostate cancer : a comprehensive review. (October 2021), 2022. → page 76

Appendix A

A Possible Approach for *In Vivo* Diagnosis of Prostate Cancer

A.1 Sensor Design and Fabrication

As discussed in Chapter 1, fiber Bragg grating (FBG) sensors are appropriate for force measurements in biomedical applications. A fiber Bragg grating is a microstructure, generally a few millimeters in length, that is photo inscribed in the core of a single mode optical fiber. When the full spectrum of light passes through the fiber Bragg grating, a specific wavelength is reflected back and measured by an interrogator. When the fiber Bragg grating is subject to strain, the reflected wavelength changes accordingly. We proposed using a FBG sensor to test the *in vivo* stress relaxation in the prostate gland. The design for the sensor is shown in Fig. A.1. The sensor is composed of a 3D printed enclosure, sensor head, and polyurethane rod. A fiber Bragg grating sensor (FBGS Technologies Company, Jena, Germany) was first bonded onto a 5 mm polyurethane rod using Norland UV-curable Adhesive NOA 61 (Norland Products, New Jersey, USA). The rod was sanded on one side to provide a suitable flat surface for bonding. Once the sensor was bonded to the rod, it was glued into the sensor head and the bottom of the sensor enclosure. The rod was suspended in the middle of the enclosure to allow for unconfined compression when an axial load is applied. The sensor head has an indentation face of 6 mm (dia.) and is manufactured using Master Mold Resin

(MiiCraft, Vaughan, Canada) via stereolithography 3D printing. The sensor head also contains two grooves to prevent torsional strain from affecting the axial loading during compression. The assembled sensor has an outer diameter of 15 mm and a total length of 26 mm. The enclosure was fabricated from polylactide acid (PLA) using the Monoprice Mini Select V2 3D Printer.

The fabricated sensor was attached to a linear actuator for stress relaxation experiments. To ensure proper compression and reliability in capturing the stress relaxation, the actuator requires a pull-in force of 2 N, linear speed of 10 mm/s, and accuracy of at least 0.5 mm. The specifications are chosen so that the sensor can provide enough force to compress the prostate tissue by 5 mm at a rate that is appropriate for capturing the stress relaxation. To fulfill the criteria, an L12 linear actuator supplied by Actuonix (12 V, 100:1 gearing, with position feedback) was used. An adaptor was also 3D printed to connect the sensor to the actuator (the adapter is not shown in Fig. A.1).

The sensor is calibrated using the mechanical tester described in Section 2.1 (see Fig. A.2). The sensor was placed directly under the indenter tip and force calibration experiments were conducted over a range of 0 to 2.25% strain using the fiber Bragg grating at strain intervals of 0.225%. The FBG sensor was connected to an FBG-Scan 908 interrogator (FBGS Technologies Company, Jena, Germany) and sensor readings were recorded at 100 Hz. For each increment, the static force from the load cell and the central wavelength shift from the interrogator were recorded. The calibration procedure was repeated three times to ensure consistent results. The sensor calibration results showed the sensitivity to be 4 mN in a range of 0-4.0 N, corresponding to a strain of 2.5%. The calibration shows linearity between the measurements (wavelength shift in the FBG sensor) and force, which is reflected by the R-squared value of 0.9998 and a maximum non-linearity error of 22 mN. The current sensor design is 15 mm in diameter, which is sufficiently small to be suitable for *in-vivo* prostate tissue examinations. The sensor design greatly simplifies the fabrication procedure as no complex machining is required, and the number of different components in the assembled sensor are kept at a minimum. This helps to reduce sources of error, improves reliability, and minimizes the cost.

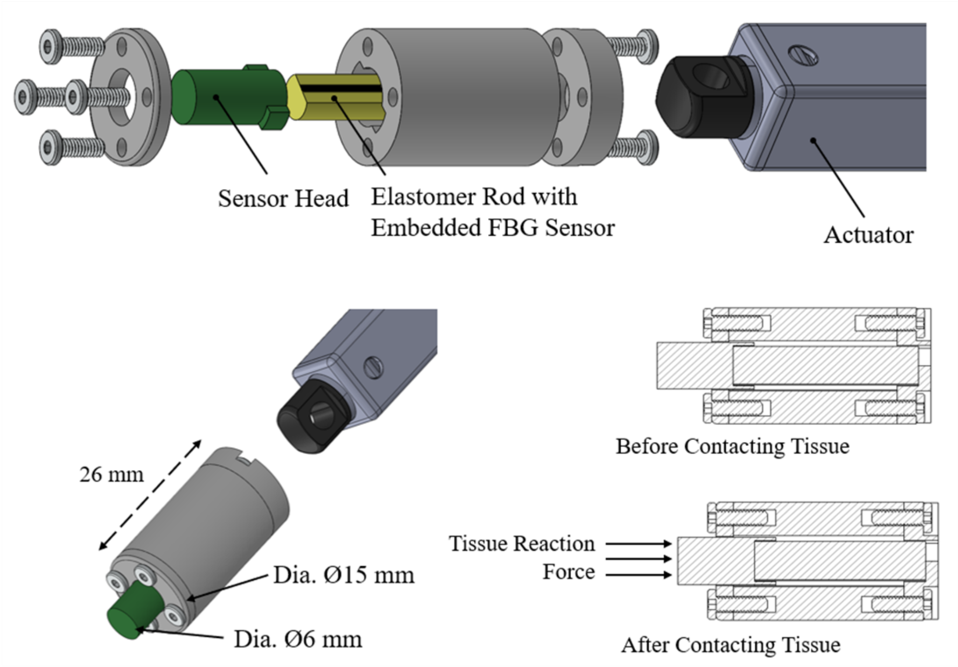
Sensor Head
Elastomer Rod with Embedded FBG Sensor
Actuator
26 mm
Dia. Ø15 mm
Dia. Ø6 mm
Before Contacting Tissue
Tissue Reaction Force
After Contacting Tissue

Figure A.1: Design of the proposed FBG sensor: The sensor is composed of an FBG sensor bonded to a elastomer (polyurethane) rod and it is supported by a 3D printed enclosure. The rod is designed to contact the material through a sensor head with a diameter of 6 mm. The sensor is compressed into a material by using an actuator and the force reaction of the material is recorded over time. The size of the sensor is designed to allow for *in vivo* applications.

A.2 Validation on Prostate-mimicking Phantoms

The applicability of the sensor was demonstrated by testing the prostate-mimicking phantoms (Fig. A.3). The phantoms were fabricated following the procedure described in Section 4.1.1. As shown in Fig. A.3, a test rig was fabricated to rigidly hold the actuator and sensor for the stress relaxation experiments. The sensor compresses the prostate phantom in the four quadrants (as shown in Fig. A.3a) following the protocol described in Fig. 4.1. Each test was repeated three times. For each phantom that was tested, a cancerous nodule was inserted in quadrant L1. The QLV parameters for each quadrant (g_is and σ_E) were then calculated according to

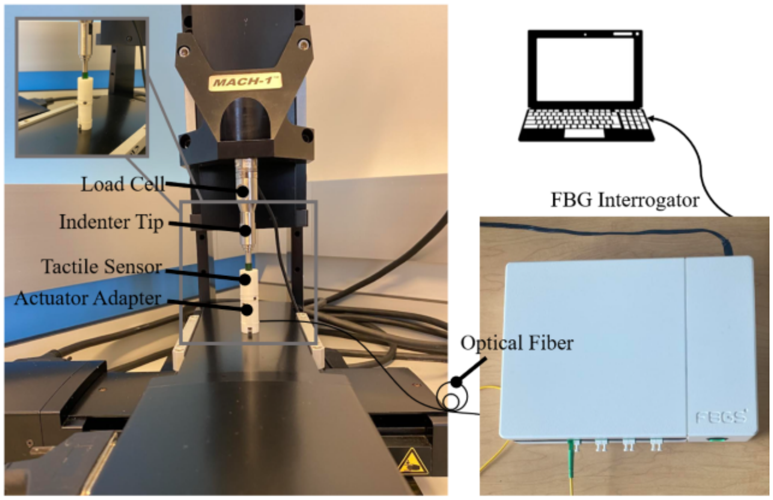

Figure A.2: Sensor calibration: the mechanical tester described in Section 2.1 was used to calibrate the sensor. The FGB sensor was placed beneath the tester's indenter and a range of strains from 0 to 2.25% were applied in intervals of 0.225%. The sensor information was read through the interrogator and calibrated by the forces recorded for the load cell. The calibration showed a linear relationship between the sensor's measurements (wavelength shift in the FBG sensor) and Force, with a maximum non-linearity error of 22 mN.

the procedure outlined in Chapter 3, and compared to Figs. A.4 and A.5.

The QLV parameters for each location in the prostate phantom are shown in Fig. A.4. In all tests, the g_i parameters from the quasi-linear viscoelastic model were smaller in the cancerous region of the phantom compared to the non-cancerous regions. As mentioned earlier, this result is expected since the shear relaxation moduli for the hard nodules are four-times smaller than those of the phantom. Based on the results, the sensor was able to identify both the elastic and viscous properties of the phantoms. Furthermore, in all tests, the elastic stress was highest in quadrant L1 where the cancerous nodule had been implanted (Fig. A.5). The elastic and viscous parameters are directly related to the size of the nodules, with larger nodules leading to higher elastic stresses and shear relaxation moduli. The results shown in Figs. A.4 and A.5 demonstrate that the FBG sensor, equipped with the QLV model, can identify the hard nodules in the phantoms. Nevertheless,

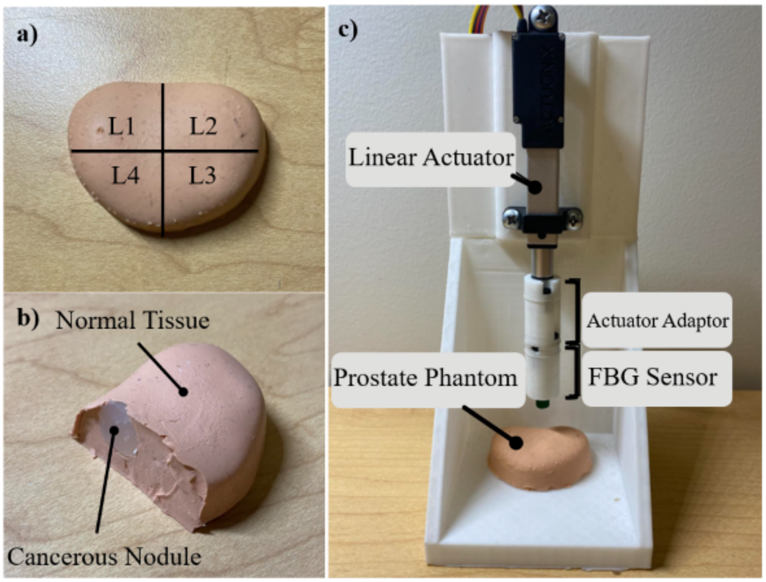

Figure A.3: Testing the FBG sensor on the prostate-mimicking phantoms: phantoms were fabricated as described in Section 4.1.1 and the nodule was located in L1; c) the FBG sensor was used to measure the force response of the prostate phantoms after each test. The sensor was connected to the actuator with an adaptor and a custom-built rig. Experiments were repeated three times for each quadrant (L1-L4) and the average QLV parameters were recorded for each quadrant.

the applicability of the sensor for *in vivo* diagnosis of PCa requires further clinical testing. In particular, the current design for connecting the actuator and sensor would require modification to accommodate *in vivo* testing. Specific guidance of the sensor in the rectum would also need to be considered so that movement of the sensor does not cause injury. While we did not assess whether or not the current design would satisfy the *in vivo* requirements, we believe that it is a step forward in providing a better tool for detecting PCa cancer in the early screening stages.

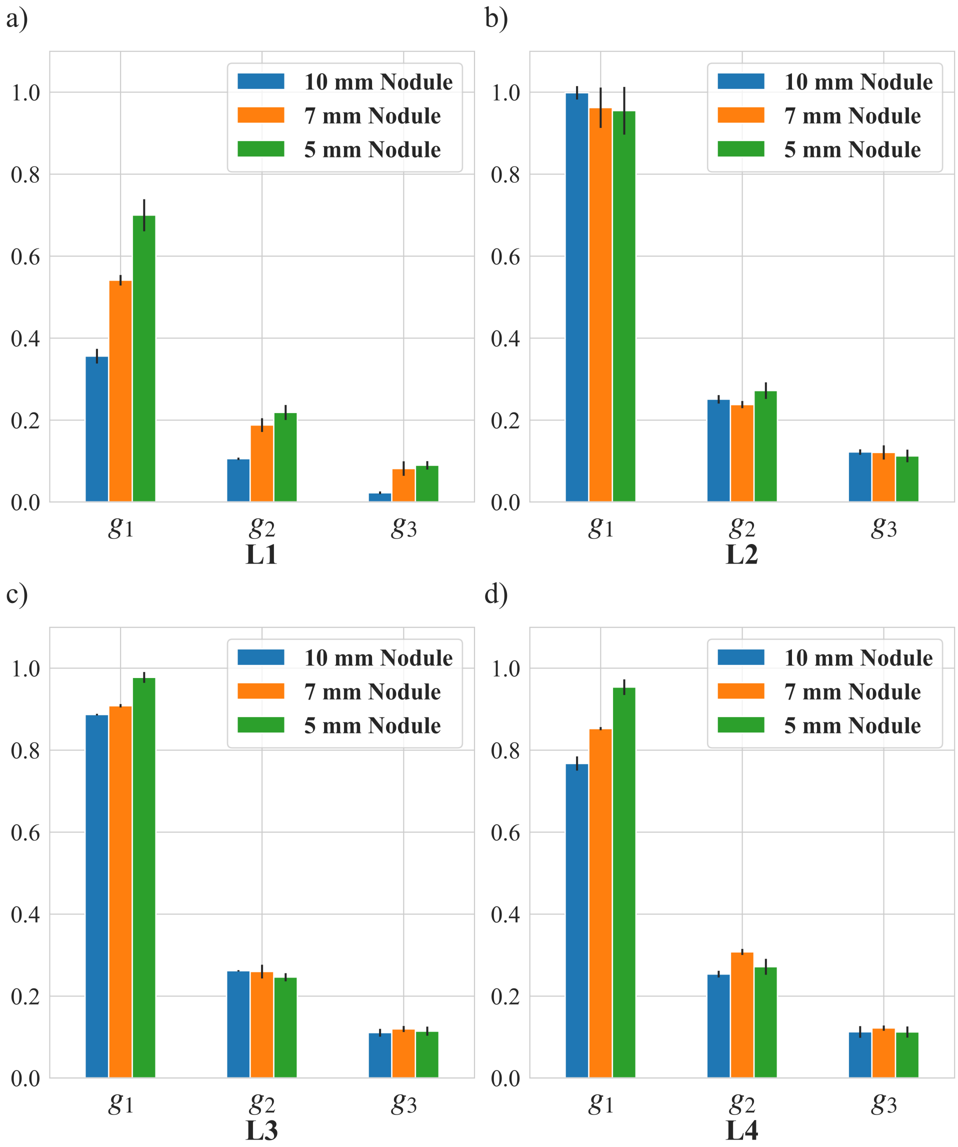

Figure A.4: Validation of the FBG sensor applicability by testing on prostate-mimicking phantoms: viscous properties (g_i s) are reported for a) L1, b) L2, c) L3, and d) L4 for hard nodules with diameters of 5 mm, 7 mm, and 10 mm. The figure shows that the most variation occurs for the properties at L1, where the nodules are located. The properties at L4 also vary slightly for the different nodule sizes, which is likely due to the effect of a hard nodule in a nearby quadrant. L2 and L3, however, have similar properties for the different nodule sizes.

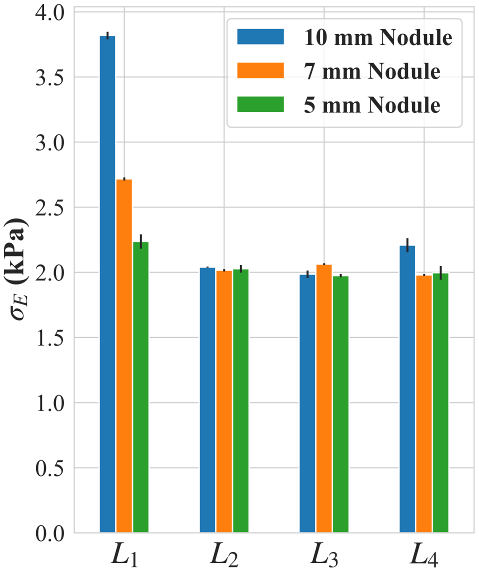

Figure A.5: Validation of the FBG sensor applicability by testing the prostate-mimicking phantoms: elastic stress is shown for quadrants with different nodule sizes. The figure shows that the greatest variation in elastic stress occurs with the nodule sizes at L1. The elastic stress at L4 also varies slightly with the nodule size, which is likely due to the effect of a nearby quadrant. L2 and L3, however, have similar amounts of elastic stress for the different nodule sizes.

Appendix B

Prostate Glands for Clinical Study

Table B includes the prostate samples we used for the clinical study as well as the cancer location(s), cancer grade, prostate volume, tumor volume, prostate mass, and patient's age.

Table B.1: Characteristics of fresh prostate samples used in the clinical study: Thirty-five fresh prostate samples, identified as P1-P35 were collected within two hours after removal by prostatectomy surgery. The table includes the location(s) of the cancer in mid and apical sections, cancer grade, Gleason score, prostate volume, prostate mass, and the patient's age. The results for samples P1-P3 are used in Section 3.1 to check the suitability of the QLV model for the prostate gland, and the results for samples P4 - P35 are used in Sections 3.1 and 3.2 for studying the effect of cancer on the properties of the prostate gland. Some of the prostate characteristics were not available and appear empty in the table.

	Cancer Location (s)		**Cancer Grade (Gleason Score)**	**Prostate Volume (ml)**	**Tumor Volume (ml)**	**Prostate Mass (g)**	**Patient's Age**
	Mid Section	**Apex Section**					
P1	Right (Posterior)	Right (Posterior)	3 (4+3)	50	5	50	68
P2	Right and Left (Anterior)	None	2 (3+4)	40	2	46	54
P3	Left (Anterior)	None	5	70	5	86	61
P4	None	Left (Posterior)	3 (4+3)	178	5	165	72
P5	Left (Anterior)	Left (Anterior)	2 (3+4)	35	5	43	70
P6	Left (Posterior)	Left (Posterior)	3 (4+3)	37		46	68

P7	Right (Anterior)	Right (Anterior)	2 (3+4)	42	6	47	73
P9	Right (Posterior)	Right (Posterior)	4	87	13	90	70
P11	Right and Left (Anterior)	Left (Anterior)	2 (3+4)	63		46	66
P12	Right (Posterior)	Right (Posterior)	3 (4+3)	49		55	79
P13	Left (Anterior)	Left (Anterior)	2 (3+4)			51	62
P14	Right (Anterior)	Right and Left (Anterior)	2 (3+4)			63	79
P15	Left (Posterior)	Left (Posterior)	2 (3+4)	48	12	63	64
P16	Right (Posterior)	None	5	94		104	79
P17	None	Right (Anterior)	5	41	6	45	70
P18	Right (Anterior)	None	3 (4+3)	45	9	51	69

P19	Right (Anterior)	Left (Anterior)	4	44	2	47	67
P20	Left (Posterior)	Left (Posterior)	3 (4+3)	70	11		68
P21	Right and Left (Anterior)	Left (Anterior)	2 (3+4)	67	23	70	71
P22	Right (Posterior)	Right (Posterior)	2 (3+4)	40	6	44	61
P23	Left (Anterior)	Left (Anterior)	3 (4+3)	43	3	38	72
P24	Left (Posterior)	Right (Posterior)	5	53	8	60	73
P25	Left (Posterior)	Left (Posterior)	2 (3+4)	42	6	48	59
P26	Left (Posterior)	None	3 (4+3)	42		49	60
P27	Left (Posterior)	None	3 (4+3)	78	5	87	69
P28	Left (Posterior)	None	2 (3+4)	77			61

P29	Left (Posterior)	Left (Posterior)	3 (4+3)	37	6		57
P30	Left (Posterior)	Left (Posterior)	2 (3+4)	38	11	47	69
P31	None	Left (Anterior)	3 (4+3)	65	7	69	70
P32	None	Right (Anterior)	2 (3+4)	81	4	80	77
P33	Left (Anterior)	Right and Left (Anterior)	2 (3+4)	53	11	48	71
P34	Left (Anterior)	Left (Anterior)	3 (4+3)	58	6	67	71
P35	Right (Anterior)	Right (Anterior)	3 (4+3)	35		35	69